Free Energy Surface and Scaling in High – T_c Superconductors

by

Ahmad Fathi Abdallah Salem

A Thesis Presented to the

FACULTY OF THE COLLEGE OF GRADUATE STUDIES

KING FAHD UNIVERSITY OF PETROLEUM & MINERALS

DHAHRAN, SAUDI ARABIA

In Partial Fulfillment of the
Requirements for the Degree of

MASTER OF SCIENCE

In

PHYSICS

December, 1999

INFORMATION TO USERS

This manuscript has been reproduced from the microfilm master. UMI films the text directly from the original or copy submitted. Thus, some thesis and dissertation copies are in typewriter face, while others may be from any type of computer printer.

The quality of this reproduction is dependent upon the quality of the copy submitted. Broken or indistinct print, colored or poor quality illustrations and photographs, print bleedthrough, substandard margins, and improper alignment can adversely affect reproduction.

In the unlikely event that the author did not send UMI a complete manuscript and there are missing pages, these will be noted. Also, if unauthorized copyright material had to be removed, a note will indicate the deletion.

Oversize materials (e.g., maps, drawings, charts) are reproduced by sectioning the original, beginning at the upper left-hand corner and continuing from left to right in equal sections with small overlaps.

Photographs included in the original manuscript have been reproduced xerographically in this copy. Higher quality 6" x 9" black and white photographic prints are available for any photographs or illustrations appearing in this copy for an additional charge. Contact UMI directly to order.

Bell & Howell Information and Learning
300 North Zeeb Road, Ann Arbor, MI 48106-1346 USA

UMI®
800-521-0600

Free Energy Surface and Scaling in High-T_c Superconductors

BY

Ahmad Fathi Abdallah Salem

A Thesis Presented to the

FACULTY OF THE COLLEGE OF GRADUATE STUDIES

KING FAHD UNIVERSITY OF PETROLEUM & MINERALS

DHAHRAN, SAUDI ARABIA

In Partial Fulfillment of the
Requirements for the Degree of

MASTER OF SCIENCE

In

PHYSICS

December 1999

KING FAHD UNIVERSITY OF PETROLEUM & MINERALS
DHAHRAN 31261, SAUDI ARABIA

DEANSHIP OF GRADUATE STUDIES

This Thesis written by **Ahmad Fathi Abdallah Salem** under the direction of his Thesis Advisor and approved by his Thesis Committee, has been presented and accepted by the Dean of Graduate Studies, in partial fulfillment of the requirements for the degree **MASTER OF SCIENCE IN PHYSICS**.

Thesis Committee:

Dr. Khalil A. Ziq (Advisor)

Dr. Mohammed Al-Ohali (Member)

Dr. Abdul-Karim Mekki (Member)

Dr. Mohammed Fettouhi (Member)

Dr. John Shirokoff (Member)

Department Chairman

Dean of Graduate Studies

5/2/2000
Date

الإهداء

إلى والدي ووالدتي
وزوجتي
وإخواني وأخواتي
وأبنائي عبد الله ومحمد
مع صادق الوفاء والتقدير

ACKNOWLEDGMENTS

Praise be to Allah, the Merciful, the Compassionate, and blessing and peace upon the Master of Prophets, our prophet Muhammed (Peace Be Upon Him).

First of all, I have to express my sincere gratitude for my advisor Dr. Khalil Ziq for offering me continuous support, unfailing enthusiasm and good ideas. I will always remember his relentless encouragement and friendship. I also wish to thank all members of my Thesis Committee Dr. Abdul-Karim Mekki, Dr. Mohammed Fattouhi, and Dr. Mohammed Al-Ohali for their valuable advice and support. The help of Dr. N. Hamdan during the early stages of the project is greatly appreciated. Great thanks to Dr. J. Shirokoff for his help in carrying out X-ray diffraction. Thanks to the Cryogenics lab staff for their cooperation in providing liquid nitrogen and liquid helium. Special thanks to Dr. A. Al-Saif and Mr. M. Khodjah for their assistance in learning Scientific Work Place.

The support of **King Fahd University of Petroleum and Minerals** is gratefully acknowledged. I will not forget the encouragement and help of the management and faculty of Al-Manara school in Al-Khobar.

Finally, no words will be enough to express my indebtedness to my parents, my wife, my brothers, my sisters, and my sons Abdullah and Mohammed.

TABLE OF CONTENTS

LIST OF FIGURES

LIST OF TABLES

THESIS ABSTRACT

Name : Ahmad Fathi Abdallah Salem

Title : Free Energy Surface and Scaling in High-T_c Superconductors

Major : PHYSICS

Dec. 1999

In this thesis, we investigate the scaling of the critical current density (J_c)and the pinning force (PF) in $Y_{1-x}Gd_xBa_2Cu_3O_{7-\delta}$ high-T_c superconductors and $La_{1.45}Nd_{0.40}Sr_{0.15}CuO_4$ stripe phase superconductor. The main objective is to study the effect of paramagnetic contribution on thermodynamic scaling of superconducting and magnetic properties.

Magnetization measurements were performed for all the samples at different temperatures below T_c and fields up to 9 tesla. We were able to subtract the paramagnetic contribution (due to Gd^{3+} ions) from the total magnetization by fitting the paramagnetic contribution at high fields using the extended Brillouin function. A thermodynamic approach to calculate the critical magnetic field H_c for the Gd doped samples was followed.

The critical current density (J_c) and the pinning force (PF) behavior were studied at different temperatures and fields. We have found that Gd substitution has pronounced effects on J_c and PF but very little effect on H_c. Then, it is possible to use the H_c values as a single scaling parameter for both critical current density and pinning force. This scaling scheme illustrates the importance of the free energy (which is related to H_c) in pinning mechanism.

Finally, the study is extended to another completely different system which is the stripe phase superconductor, namely $La_{1.45}Nd_{0.40}Sr_{0.15}CuO_4$ single crystal.The paramagnetic moments (due to Nd^{3+} ions) are along the c-axis and J_c and PF have different values along both directions. The evaluated H_c which is independent of the direction of the applied field has been used as a single scaling parameter for both J_c and PF for applied fields parallel to the c-axis and along the ab-plane. In all studied cases, the normalized critical current density ($J_n=J_c/H_c$) and normalized pinning force ($PF_n=PF/H_c^2$) showed a universal behavior with the normalized magnetic field ($H_n=H/H_c$).

MASTER OF SCIENCE DEGREE

KING FAHD UNIVERSITY OF PETROLEUM AND MINERALS

Dhahran, Saudi Arabia

Dec. 1999

خلاصة الرسالة

الاسم الكامل: أحمد فتحي عبد الله سالم

عنوان الدراسة: سطح الطاقة الحرة والمعايرة في المواد المفرطة التوصيل الكهربائي

التخصص: فيزياء

التاريخ: ديسمبر ١٩٩٩ م

تعنى هذه الدراسة ببحث معايرة التيارات الحرجة والقوى المثبتة في عينات من مواد فائقة التوصيل الكهربائي هي $Y_{1-x}Gd_xBa_2Cu_3O_7$ و $La_{1.45}Nd_{0.40}Sr_{0.15}CuO_4$ باستخدام المجال المغناطيسي الحرج والذي له علاقة بخواص المادة الحرارية. الهدف الرئيسي من هذه الدراسة هو معرفة تأثير وجود ذرات لها نشاط مغناطيسي (Gd و Nd) على الخواص الحرارية والمغناطيسية للموصلات الفائقة.

تم إجراء قياسات المغنطة على جميع العينات عند درجات حرارة مختلفة ومجالات مغناطيسية تصل إلى ٩ تسلا. وقد تمكنا من طرح التأثير المغناطيسي (والذي يعزى لوجود أيونات الـ Gd^{3+}) من منحنى التمغنط باستخدام دالة بريليون المعدلة لمواءمة المنحنى عند مجالات مغناطيسية عالية. وقد تم اتباع طريقة تعتمد على خواص المادة الحرارية لحساب قيم المجال المغناطيسي الحرج عند درجات حرارة مختلفة ولعينات تحتوي تركيزات مختلفة من الـ Gd.

سلوك التيارات الحرجة والقوى المثبتة تمت دراستها عند درجات حرارة ومجالات مغناطيسية مختلفة. وقد وجد أن لتركيز الـ Gd تأثير كبير على قيم التيارات الحرجة والقوى المثبتة ولكن تأثيره ضعيف على قيم المجال المغناطيسي الحرج. ثم قمنا بمعايرتهما باستخدام قيم المجالات المغناطيسية الحرجة حيث أظهر كل منهما سلوكاً موحداً مما يدل على أن ميكانيكية القوى المثبتة تعتمد على خواص المادة الحرارية.

في ختام الدراسة ، تم تطبيق الخطوات سالفة الذكر على مادة أخرى ذات خواص مختلفة وهي $La_{1.45}Nd_{0.40}Sr_{0.15}CuO_4$ والتي تعد ذات بلورة واحدة ومجالات أيونات الـ Nd^{3+} فيها تكون موازية لاتجاه c-axis. وقد تمكنا من حساب قيم المجالات المغناطيسية الحرجة في الاتجاهين بموازاة c-axis أو ab-plane ووجدنا أن هذه القيم متساوية في كلا الاتجاهين كما هو متوقع. باستخدام هذه القيم من المجالات المغناطيسية الحرجة (كمعامل وحيد للمعايرة) تمت معايرة التيارات الحرجة والقوى المثبتة أيضاً، علماً بأن التيارات الحرجة والقوى المثبتة لها قيم مختلفة تماماً في كلا الاتجاهين (c-axis و ab-plane).

يجدر بالذكر أن التيارات الحرجة المعايرة ($J_n=J_c/H_c$) والقوى المثبتة المعايرة ($PF_n=PF/H_c^2$) قد أظهرت سلوكاً موحداً مع المجالات المغناطيسية المعايرة ($H_n=H/H_c$).

درجة الماجستير في العلوم

جامعة الملك فهد للبترول والمعادن

الظهران ٣١٢٦١ – المملكة العربية السعودية

CHAPTER 1

Introduction

1.1 History of Superconductivity

The key for discovering superconductivity was the liquefaction of helium in 1908 by H. K. Onnes. Later, he started to study the resistivity of metals at very low temperatures using liquid helium as a coolant. In 1911, Onnes and co-worker noticed a surprising event, namely the sharp drop of resistivity of mercury (Hg) to zero at 4.15 K. He called this phenomena superconductivity. After this discovery, Onnes studied other metals and noticed that some become superconducting below a certain temperature called the critical temperature T_c [1].

In 1933, H. Meissner studied the magnetic behavior of superconductors and discovered that when cooled below their critical temperatures in the presence of a magnetic field, the magnetic flux is expelled out of the superconductor, a behavior which is completely unexpected for ordinary or even perfect conductors. In a superconductor the induced supercurrents due to a magnetic field exactly balance the applied field and prevent field lines from penetrating (see Fig. 1). In ordinary conductors, an induced current will be generated

if there is a magnet moving nearby or a changing magnetic field. This is the principle upon which electric generators operate. Superconductors lose superconductivity above a certain magnetic field called the critical magnetic field H_c [2]. In 1930's, other superconducting metals, alloys and compounds were discovered.

The first theory to explain superconductivity appeared in 1957 by J. Bardeen, L. Cooper and J. Schrieffer (the BCS theory) [1]. They proposed that in the superconducting state electrons are bound together as pairs (called cooper pairs) with zero spin and zero total momentum. Therefore, one can consider that the charge carriers in superconductors are bosons rather than electrons (fermions) [1]. This theory explains superconductivity at temperatures close to absolute zero but at higher temperatures, the theory becomes inadequate for the newly discovered high-T_c superconductors.

In 1986, the discovery of a new high-T_c superconducting material with $T_c \approx 35$ K was announced. Early in 1987, the discovery of $YBa_2Cu_3O_{7-\delta}$ was announced with transition temperature $T_c \approx 93$ K, which is above the liquid nitrogen temperature [3], [4]. The very strange feature of these new high-T_c superconductors is that they are ceramics which are normally insulators at room temperature, and don't conduct electricity at very low temperatures. Therefore, scientists started to look for new superconducting materials even with unimagined combinations of elements.

In the following few years, scientists were able to synthesize new superconductors with T_c above 130 K. There appears to be no end in sight, and perhaps some day there will be a room-temperature superconductor [5], [6](See Fig. 2).

Quitely, the hope was dimmed, and most of the effort was devoted to understand the

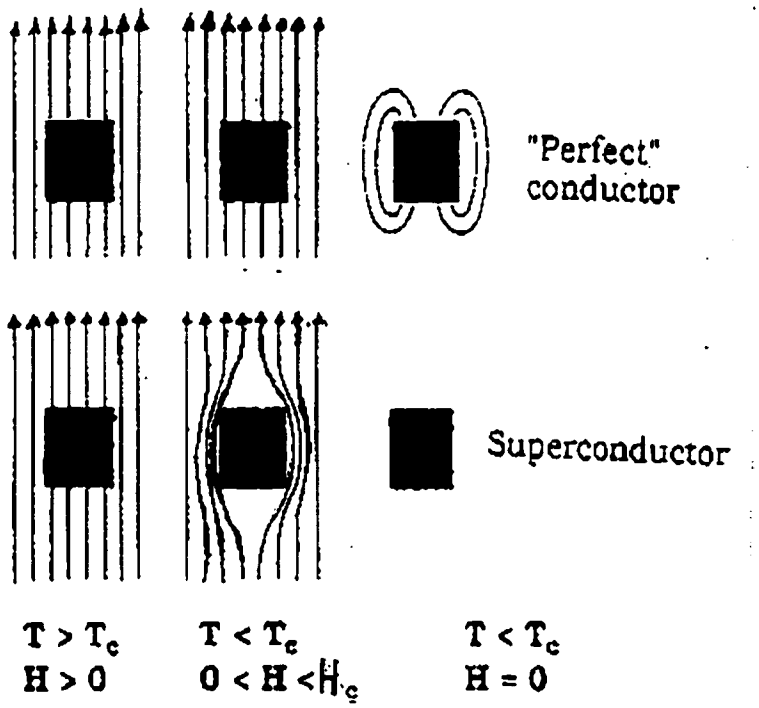

Figure 1: Meissner effect in superconductors.

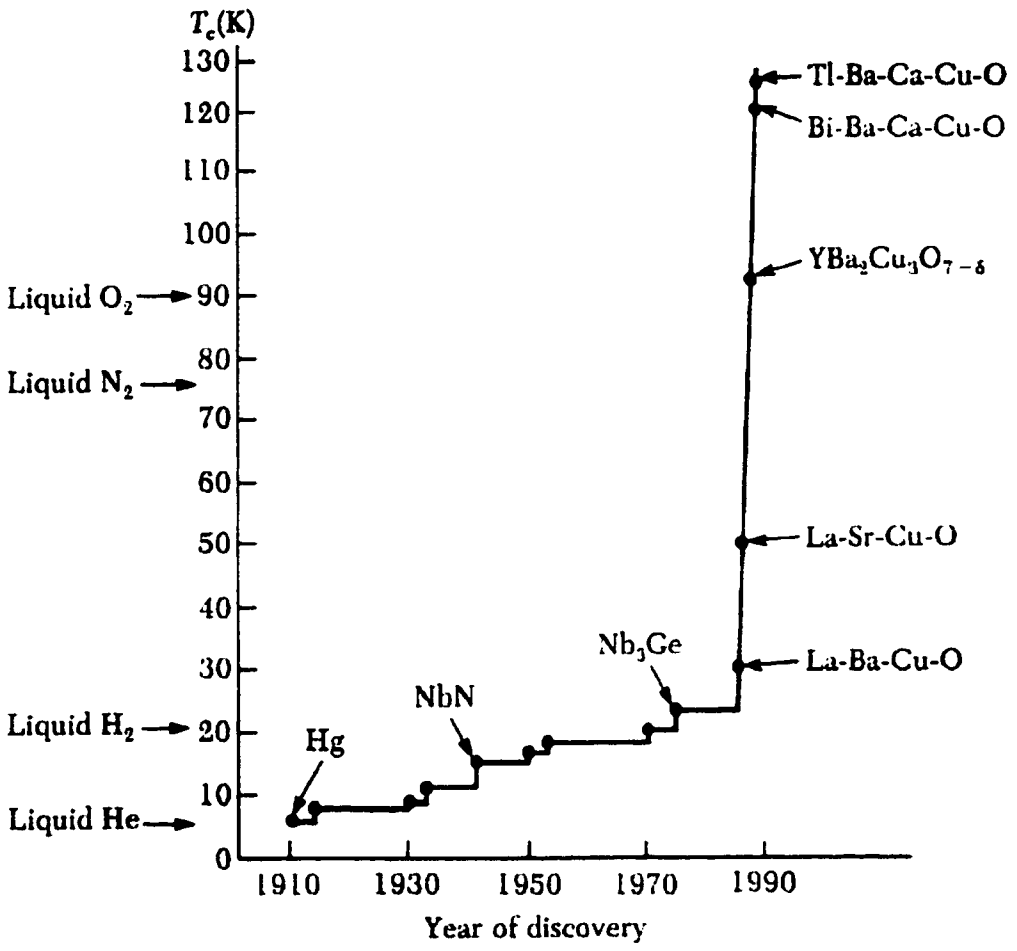

Figure 2: Transition temperature and year of discovery.(after *Serway*)

behavior various properties of high T_c superconductors, improve their mechanical and physical properties and push them into more practical and commercial applications.

1.2 Types of superconductors

There are two parameters that characterize a superconducting material, namely the coherence length (ξ) and the penetration depth (λ). The coherence length is defined as being the distance over which electrons in a cooper pair remain together. The penetration depth is the maximum distance that magnetic field penetrates through a superconductor according to the following expression:

$$H(x) = H(0)\exp(\frac{-x}{\lambda}) \tag{1.1}$$

where H is the magnetic field and x is the depth from the surface. The values of ξ and λ are of the order of 10 to 10^3 nm[1].

Superconductors are divided into two types depending on the Ginzburg-Landau (GL) parameter κ which is the ratio of ξ and λ ($\kappa = \frac{\lambda}{\xi}$).

1.2.1 Type I Superconductors

Type I superconductors have GL parameter κ less than $\frac{1}{\sqrt{2}}$. Many of the elemental superconductors were found to be of type I superconductors. These materials have low

critical temperatures and they have only one critical magnetic field H_c above which the superconductivity is destroyed. The critical magnetic field follows a quadratic temperature dependence, namely:

$$H_c(T) = H_c(0)\left[1 - \left(\frac{T}{T_c}\right)^2\right] \tag{1.2}$$

Below H_c, type I superconductors exhibit perfect diamagnetism which is an essential property of the superconducting state.

1.2.2 Type II Superconductors

Type II superconductors have a GL parameter larger than $\frac{1}{\sqrt{2}}$. These materials are characterized by two critical magnetic fields H_{c1} and H_{c2}. When the applied magnetic field is less than H_{c1}, the material is a perfect diamagnet, entirely superconducting and the magnetic flux is expelled out of the superconductor. When the applied magnetic field is larger than H_{c2}, the superconducting state is destroyed. For fields in between H_{c1} and H_{c2}, the material is in a mixed state (also called the vortex state). One can view the vortex state as a cylindrical swirl of supercurrents which surround a normal core which allows some flux to penetrate the interior of the type II superconductor. The normal core has a cyliderical shape in conventinal type II superconductors and believed to have a flat cylinderical or pan-cake shape in high-T_c superconductors [1], [2].

1.3 High-Temperature Superconductors (HTSC)

The era of HTSC started in 1986 and still is a fascinating subject. These materials are all copper oxides of one form or another. They have been determined to be type II superconductors with H_{c2} greater than 100 T and with very large $\kappa = \frac{\lambda}{\xi}$ values (200-500). All of these superconducting cuprates have layered structures (as shown in Fig. 3). There appears to be a direct correlation between the number of copper-oxygen layers in these compounds and the critical temperature [7].

Another property of these HTSC is that they are very anisotropic in nature. For example, in the normal state they show small resistivity in the copper-oxygen planes, but much higher resistivity in the direction perpendicular to these planes [1], [4], [3]. When copper atoms in these HTSC are substituted by any other atoms, superconductivity is very much affected or even destroyed. However, substitutions in other sites has varying effects on the superconductivity.

The BCS theory has been applied successfully to some properties of HTSC, but it failed with others [1]. Therefore, lots of work is done on these materials to build up a theory that explains all the properties and behavior of these materials.

Several families of superconducting ceramics have been discovered, some of these are:

1. Yttrium-based ($RBa_2Cu_3O_{7-\delta}$) with $T_c \approx 93$ K, where R is a rare earth element like yttrium. This group is the basis of our work.
2. Bismuth-based ($Bi_2Sr_2Ca_{n-1}Cu_nO_{2n+4}$) with $T_c \approx 110$ K for the phase having three CuO_2 planes and $T_c \approx 84$ K for that with two copper planes.

3. Thallium-based ($Tl_2Ba_2Ca_{n-1}Cu_nO_{2n+4}$) with T_c=90, 110 and 125 K for phases having 1, 2 and 3 CuO_2 planes, respectively.
4. Mercury-based ($HgBa_2Ca_{n-1}Cu_nO_{2n+2}$) with T_c=95, 122 and 133 K for phases having 1, 2 and 3 CuO_2 planes respectively [5].

1.4 Yttrium-Based HTSC

1.4.1 General

$YBa_2Cu_3O_{7-\delta}$ (YBCO) was the first compound discovered having a T_c above the liquid nitrogen temperature ($T_c \approx 93K$) [8]. The YBCO system can be used to prepare a wide range of superconducting (SC) compounds by replacing Y or Ba with other elements. Among these compounds are those formed by replacing Y with magnetic rare earth elements. It was surprising that superconductivity can coexist with magnetism in the same system. Pair breaking does not occur because the magnetic rare earth ions lie between the CuO_2 planes and ξ_c is small [9]. Therefore, superconductivity is not affected. On the other hand, in low T_c superconductors, magnetic ions cause breaking of Cooper pairs [9] which kills superconductivity. It has been found that in YBCO, nonmagnetic impurities affect the transition temperature T_c much more than magnetic impurities do [10]. In this study, we substituted Gd in the place of Y in $YBa_2Cu_3O_{7-\delta}$ with different concentrations, as will be discussed later. No change in Tc or the structure was observed after this substitution.

The compounds of YBCO family are very sensitive to oxygen content. For example, $YBa_2Cu_3O_{7-\delta}$ has a T_c maximized as δ goes to ~ 0.02 whereas superconductivity is destroyed at $\delta \geq 0.7$. The effect of oxygen content on $YBa_2Cu_3O_{7-\delta}$ is very well established [11], [12].

1.4.2 Structure

The structure of $YBa_2Cu_3O_{7-\delta}$ is orthorhombic ($a \neq b \neq c$). The unit cell contains three perovskite cubes with Y and Ba atoms alternating in the centers (see Fig. 3). The structure of $YBa_2Cu_3O_{7-\delta}$ is very well known and published in many books and articles, see for example [5], [4], [9], [13].

Oxygen and copper atoms are bound together in alternating layers containing chains and planes (shown in Fig. 3). These CuO_2 planes are recognized to be the essential part for superconductivity [14]. Moreover, some of the Oxygen sites are missing in the unit cells. This is why the formula has $O_{7-\delta}$ to indicate this fact. It should be noticed that {7-δ} represents the average number of oxygen atoms in the unit cells over the whole sample.

1.5 Hysteresis Loops

Hysteresis loop is the name given for the curve of magnetization vs. applied field over a complete cycle of applied magnetic field. A complete magnetic field cycle starts with a zero magnetic field then increases until reaching a maxima (say 9 T), then decreases (changing sign) to a minima (say -9 T), then increases back to zero to complete the cycle.

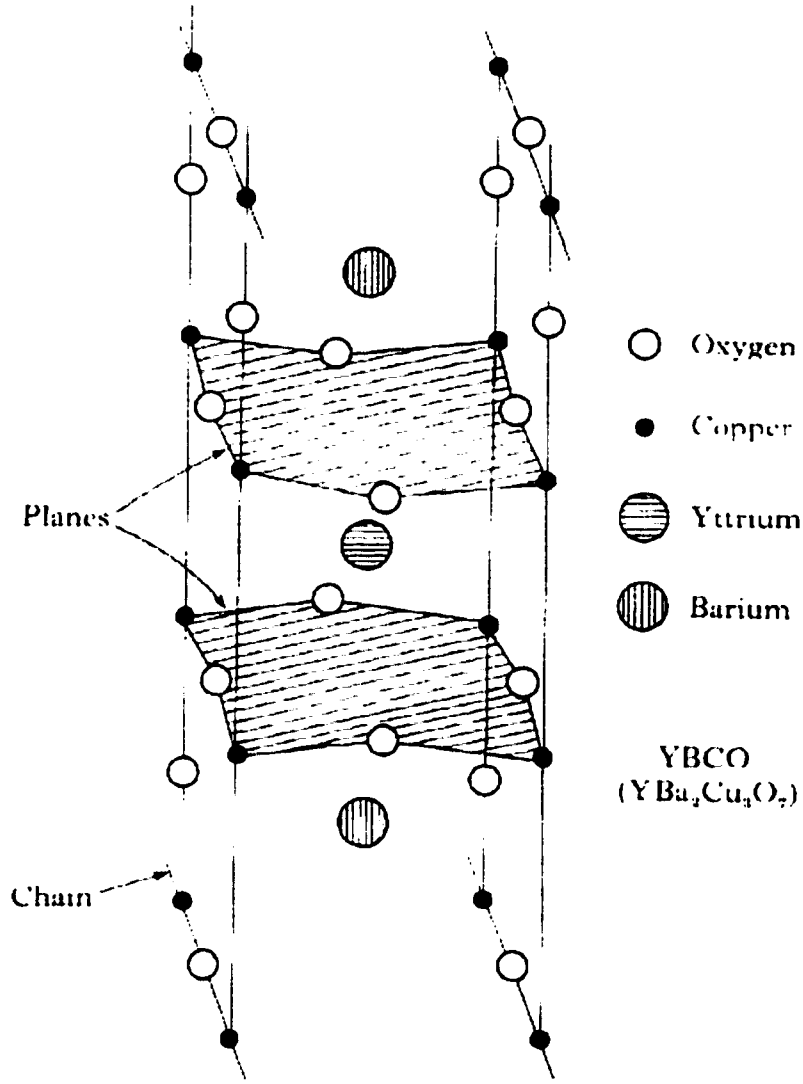

Figure 3: Structure of $YBa_2Cu_3O_7$

The literal meaning of hysteresis is 'lag behind'. Magnetization curves were named this way because they depend on the history of the sample [1].

Hysteresis Loops are very important to study superconductivity. Many features and properties can be determined using the hysteresis loops directly or indirectly via certain models. Examples of such properties calculated using the hysteresis loops are: energy loss, critical current density, remanent magnetic moment and the critical fields H_{c1} and H_{c2} [15], [16], [1].

Figs. 4 (after [15]) and 5 show hysteresis loops of $YBa_2Cu_3O_{7-\delta}$ (YBCO) at 4.5, 12 and 20 K and $GdBa_2Cu_3O_{7-\delta}$ (Gd1) at 4 K. From these two figures, we can notice the following. First, the hysteresis width gets narrower as temperature increases in Fig 4. Second, the paramagnetic effect is obvious on the hysteresis loop of Gd1 in Fig 5. The magnetization is positive for Gd1 which has a paramagnetic contribution while it is negative for the YBCO sample which is diamagnetic.

1.6 Rare Earth Elements

Rare earth is the name given to the elements of the lanthanide series in the periodic table [17]. In other words, they are the 14 elements filling the 4f shell. The ions of these elements have fascinating magnetic properties. Table 1 shows the rare earth ions and their electronic configurations.

To "classically" understand the origin of magnetic moments of these materials, it should

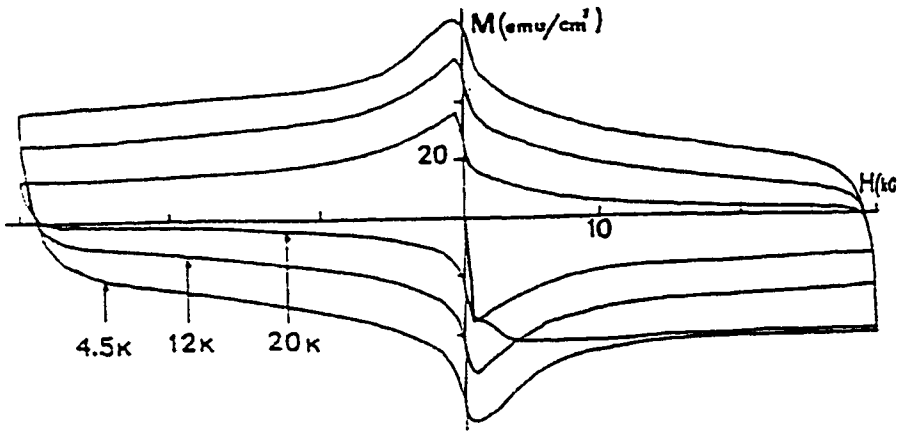

Figure 4: Hysteresis loops of $YBa_2Cu_3O_{7-\delta}$ at different temperatures.

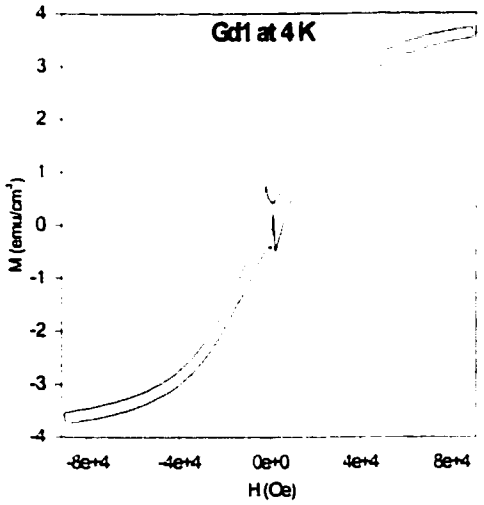

Figure 5: Hysteresis loop of Gd1 at 4 K.

TABLE 1: Rare earth ions and their electronic configurations

Ce^{3+}	Pr^{3+}	Nd^{3+}	Pm^{3+}	Sm^{3+}	Eu^{3+}	Gd^{3+}
$4f^1$	$4f^2$	$4f^3$	$4f^4$	$4f^5$	$4f^6$	$4f^7$
Tb^{3+}	Dy^{3+}	Ho^{3+}	Er^{3+}	Tm^{3+}	Yb^{3+}	
$4f^8$	$3f^9$	$4f^{10}$	$4f^{11}$	$4f^{12}$	$4f^{13}$	

be remembered that every electron acts like an electrically charged body that is spinning around a fixed axis, thus creating a magnetic moment along the axis of spin. The magnetic moment of an electron spin has a constant value called the Bohr magneton μ_B. In the rare earth series, an atom can have a nonzero magnetic moment since some of the electrons in the partly filled (4f) shell can lie in singly occupied orbital states with parallel spin [18]. In the case of Gd^{3+} ion, the configuration of the outer shell is as follows:

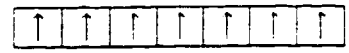

Since the shell is just half full, the application of Hund rules gives the orbital angular momentum L = 0, so the total angular momentum J = S (the total spin) [19]. This implies that J = 7/2 in the case of Gd^{3+} ions [20].

The interesting property of magnetic moment in a rare earth atom is its relative simplicity because their 4f electrons are tightly bound to the nucleus and do not contribute in the interatomic binding, which is completely accomplished by the conduction electrons [18].

1.7 Free Energy

Free energy of a superconductor is defined as the condensation energy required to

change the material from normal state to superconducting state. Because the phase transition (from normal state to SC state and vice versa) is reversible, thermodynamics can be applied to the SC materials [2], [21].

From thermodynamical arguments, when a material is magnetized by an applied magnetic field, its free energy changes by an amount proportional to the area under its reversible magnetization curve. Gibbs relation correlates the difference in free energy and the critical magnetic field via the following relation:

$$Gn - Gs = \frac{H_c^2}{8\pi} \tag{1.3}$$

The critical magnetic field can be written in terms of the area under the magnetization curve as follows [22]:

$$\int_0^{H_{c2}} MdH = \frac{H_c^2}{8\pi} \tag{1.4}$$

In this study, we will use relation (1.4) to find the H_c values for the samples under investigation by estimating the area numerically. The results are shown in chapter 4.

1.8 Statement of the Problem

In this thesis, we will study two different systems of HTSC, namely $Y_{1-x}Gd_xBa_2Cu_3O_{7-\delta}$

and $La_{1.45}Nd_{0.40}Sr_{0.15}CuO_4$ (a stripe phase superconducting material described in chapter 6). The two systems have a paramagnetic moment contribution due to the presence of the rare-earth ions Gd and Nd. The main objectives of this study are:

I) To study the effect of the thermodynamic critical field and free energy on pinning forces and critical current in both systems.

II) To study the effect of magnetic ions on pinning forces, critical current and thermodynamic critical field.

III) To study the scaling behavior of the pinning force (PF) and the critical current density (J_c) using thermodynamic critical field (H_c).

For both systems, the following will be reported:

1. Magnetization measurements (M vs. H) at different temperatures with applied magnetic fields as high as 9 T.
2. Application of extended Brillouin function for fitting the paramagnetic moments of Gd and Nd at high fields.
3. Subtraction of the paramagnetic contribution to the magnetization curve to study the superconducting contribution alone and hence calculate the thermodynamic critical field (H_c) using the free energy method.
4. The thermodynamic critical field behavior with temperature.
5. The behavior of critical current density (J_c) and pinning force (PF) at different temperatures and magnetic fields.
6. The use of H_c as a scaling parameter for the critical current density and pinning force in both systems and show the role of free energy in the pinning mechanism.

7. The deviation from BCS coupling.

CHAPTER 2

Experimental Techniques

2.1 Sample Preparation

Among the newly discovered high temperature superconductors, the preparation process of Y123 based superconductor is one of the easiest. The synthesis process is very important and in some cases crucial, as the microstructure and the oxygen content are severely affected. Incorrect annealing conditions may yield undesired phases or unexpected materials. Therefore, the preparation process should be followed by X-ray diffraction and other characterizing techniques to insure getting the desired material phase and to assist the quality of the prepared sample [23].

Special care has to be taken in preparing light-rare earth (Gd, Nd, ...) based high T_c superconductors. The light rare earth atom might occupy the Ba-site. Annealing in O_2 atmosphere during the initial stages increases atomic site replacement. Another concern is the presence of CO_2 gas during annealing since it can affect the grain boundaries, and the sharpness of the SC transition temperature and the microstructure of the light rare earth

high T_c superconductors [24].

We have prepared samples with general composition $Y_{1-x}Gd_xBa_2Cu_3O_{7-\delta}$ by solid state reaction using high purity powders of Y_2O_3, $BaCO_3$, CuO and Gd_2O_3. High purity powders are needed to ensure consistent results.

These powders are mixed properly using agate mortar for about 20 minutes. The black mixture was then pelletized in order to maximize the surface contact between particles using high pressure up to 4 tons [9]. The resulting pellets are then heated to 900°C for about 20 hours under normal atmosphere in an oven to let CO_2(resulting from $BaCO_3$ degradation) vent from the samples.

Then, the samples were cooled down to room temperature, regrounded to make sure of homogeneous reaction, pressed into small pellets and annealed at 900°C for 24 hours in oxygen gas. The samples were cooled down slowly (~1°C/min.) to 400°C in oxygen flow where they were kept for about 24 hours. Finally, the samples were furnace cooled to room temperature.

Four samples of $Y_{1-x}Gd_xBa_2Cu_3O_{7-\delta}$ were prepared in this manner, where x = 1, 0.75, 0.50, 0.25 and called Gd1, Gd2, Gd3 and Gd4, respectively.

The quality of the prepared samples was then tested roughly by observing magnetic levitation at liquid nitrogen using a small piece of magnet . Other techniques were performed to test the resulting samples, namely: the 4-probe technique, Inductive Coupled Plasma (ICP) spectroscopy and X-ray diffraction (XRD). The results of these tests are described and discussed in the following sections.

2.2 The 4-Probe Technique

In this technique, a constant current ($\sim$ 5 mA) is passed through the sample and the voltage across is measured using a sensitive nanovoltmeter (Keithley 182). The voltage is proportional to the resistivity of the specimen. Temperature of the sample is changed by controlling the height of the sample above the surface of liquid helium in a storage dewar. By measuring the voltage at different temperatures, the sudden drop in the resistivity at the critical temperature (T_c) can be measured easily ($T_c \sim 90$ K for $Gd_xY_{1-x}Ba_2Cu_3O_{7-\delta}$ samples). Fig. 6 shows a schematic diagram of the experimental setup. The results of these measurements are shown in Fig. 7 [9].

2.3 Inductively Coupled Plasma (ICP) Spectroscopy

This analytical technique was used for elemental analysis of all Gd-samples investigated in the present work. The analysis was performed in division IV of the Research Institute at King Fahd University of Petroleum and Minerals, Saudi Arabia. In this technique, a small amount of sample in solution is heated to a very high temperature enough to evaporate and dissociate the sample content into atoms in their excited states. These excited atoms will emit light and return to the ground state. The intensity of the emitted light is proportional to the concentration of the atoms present in the sample. Each element has its own characteristic emission spectral lines. A special computer software is used to determine the elements and their concentrations. For more details on the ICP technique see reference [25].

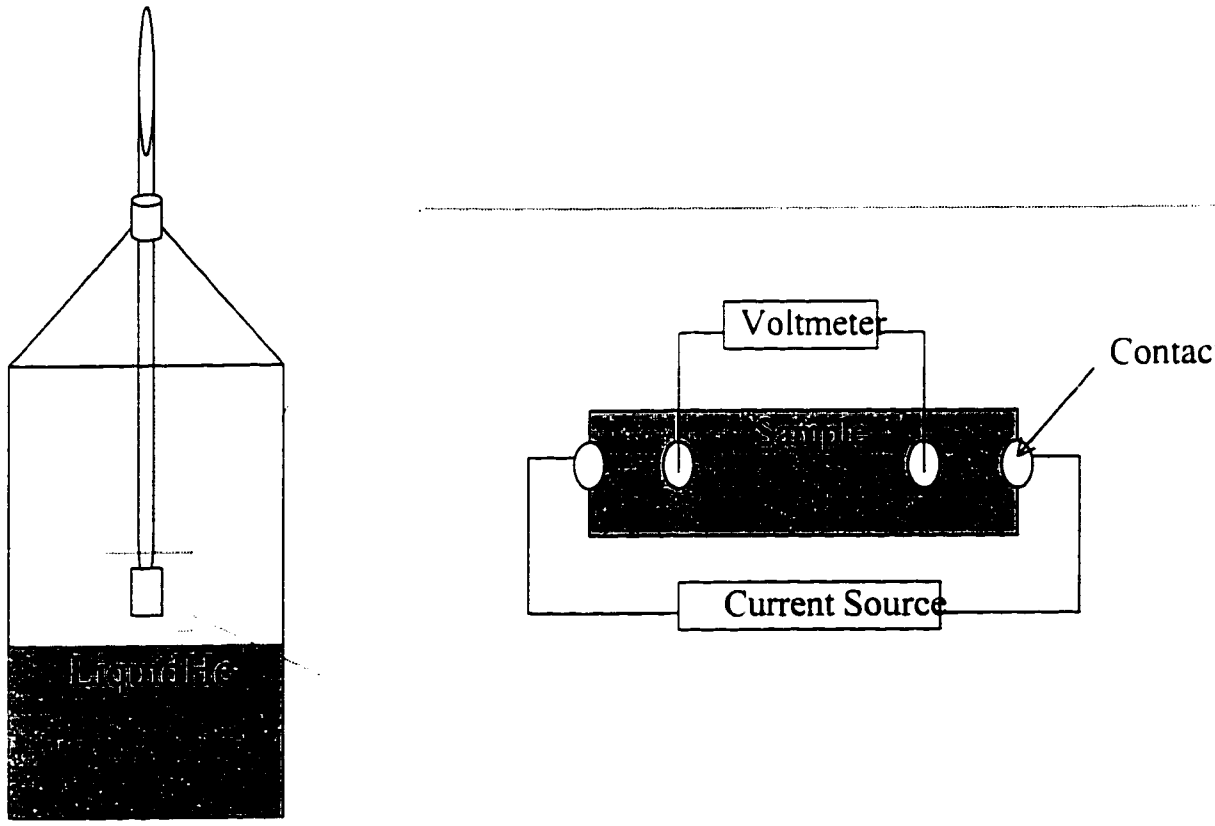

Figure 6: A schematic diagram of 4 probes connected to a sample whose temperature is measured by temperature sensor in thermal contact with the sample.

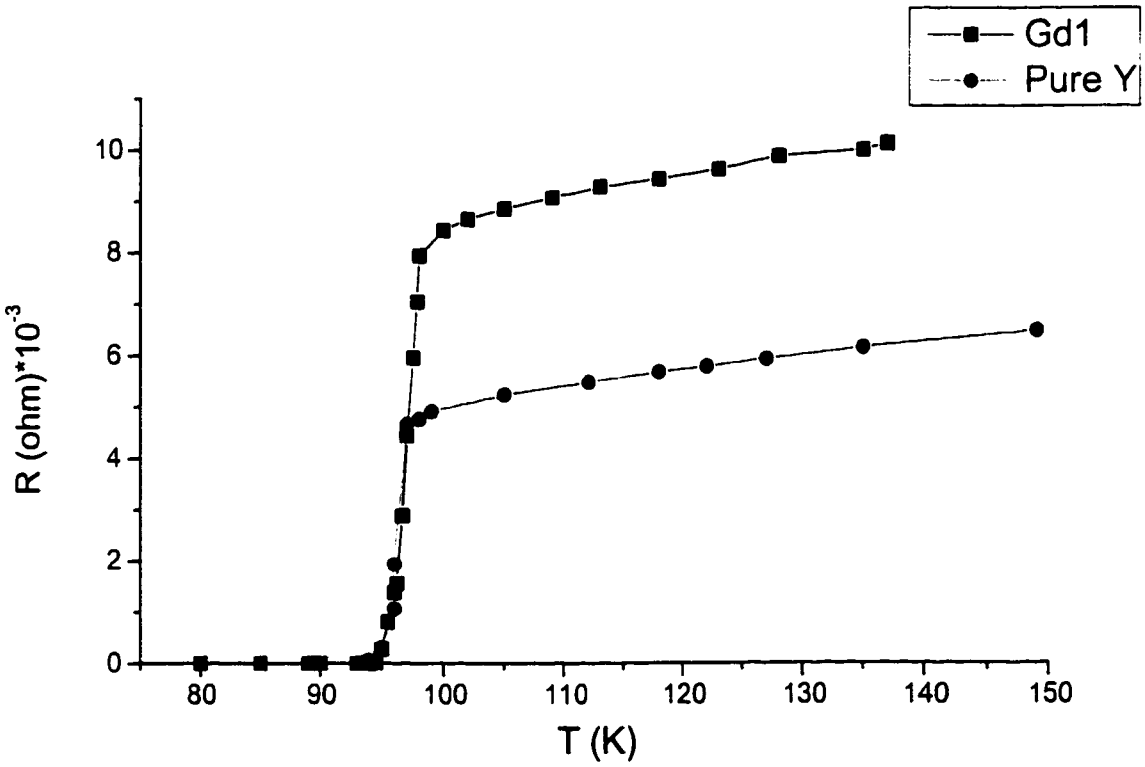

Figure 7: Resistivity vs. temperature for $GdBa_2Cu_3O_{7-\delta}$ (Gd1) and $YBa_2Cu_3O_{7-\delta}$ (pure Y) Showing that T_c for both systems is $\sim$ 93 K. The lines are guides for the eye.

TABLE 2: ICP results for Gd1 to Gd4 samples in weight percent

	Gd1	Gd2	Gd3	Gd4
BaO	41.6	42.5	43.6	44.0
CuO	33.4	34.3	35.2	35.6
Gd_2O_3	24.0	18.3	12.9	6.6
Y_2O_3	0	4.1	8.3	12.9

The results obtained from this technique are listed in Table 2.The experimental error of these results is less than 2 %.

Normalizing these numbers against (Y+Gd) would yield the results in Table 3 that reflect the atomic ratio of the constituents we have.

It is obvious that these results are reasonable within the experimental error and consistently reveals 1:2:3-ratio between Y+Gd: Ba: Cu. The ratio between Gd and Y elements in the four samples was found to be as listed in Table 4.

These results are compatible with our experimental proposition having in mind the formula of each sample (Table 5).

2.4 X-Ray Diffraction

X-ray diffraction is a semi-quantitative analysis technique primarily used on crystalline materials which can be used to obtain the lattice parameters and to determine the weight fractions of major crystalline phases down to few wt% [9]. This analysis was performed in division V of the Research Institute at King Fahd University of Petroleum and Minerals, Saudi Arabia. The X-ray pattern was obtained using a JEOL JDX-3530 XRD employing a Cu X-ray tube operating at 40 kV and 30 mA.

TABLE 3: ICP data normalized to atomic ratios

	Gd1	Gd2	Gd3	Gd4
Y+Gd	1	1	1	1
Ba	2.04	2.017	1.963	1.90
Cu	3.17	3.13	3.058	2.97

TABLE 4: Stoichiometric ratios for Y and Gd only

	Gd1	Gd2	Gd3	Gd4
Y	0	1	1.033	3.1
Gd	1	2.8	1	1

TABLE 5: Chemical formulas for Gd1 to Gd4 samples

Gd1	$GdBa_2Cu_3O_{7-\delta}$
Gd2	$Gd_{0.75}Y_{0.25}Ba_2Cu_3O_{7-\delta}$
Gd3	$Gd_{0.5}Y_{0.5}Ba_2Cu_3O_{7-\delta}$
Gd4	$Gd_{0.25}Y_{0.75}Ba_2Cu_3O_{7-\delta}$

The result of the analysis showed that all the four samples have a single orthorhombic phase. Fig 8 shows the X-ray diffraction pattern for Gd1. Our experimental data and published values [26] for the a, b and c lattice parameters are shown in Table 6.

These data clearly show that the lattice parameters are increasing with increasing Gd content. This is due to the fact that Gd-atoms are larger than Y-atoms and occupy a larger volume. This is also observed in the volume of the unit cell which has increased with increasing Gd content.

2.5 Magnetic Measurements

Vibrating sample magnetometer (VSM) was used to perform the magnetic moment measurements of each sample. Each sample was mounted in the system and studied at different temperatures and magnetic fields.

The VSM system consists of the following parts:

1. Vibrating head and sample holder.
2. Variable temperature cryostat.
3. Temperature controller.
4. VSM controller.
5. Power supply and controller of the magnet.
6. A P.C. which is connected to all of these items that has a GPIB-PcII interface card to control the experiment.

TABLE 6: Lattice parameter measurements for Gd1 to Gd4 samples compared to published data

Sample	a (A°)	b (A°)	c (A°)	V (A°3)
Gd1	3.8958	3.8466	11.6794	175.02
Gd2	3.8947	3.8350	11.6992	174.74
Gd3	3.8885	3.8243	11.687	173.79
Gd4	3.8856	3.8185	11.6804	173.30
Published data for Gd1	3.8987	3.8397	11.703	175.19

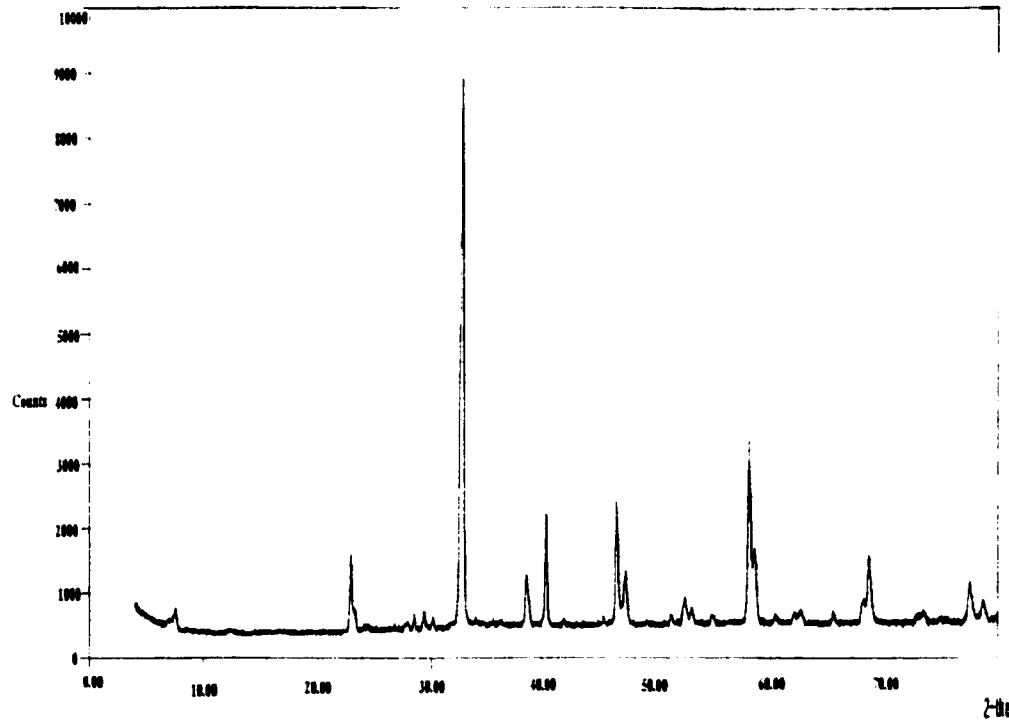

Figure 8: X-Ray diffraction pattern for Gd1.

For more details on the system see reference [12].

The experimental procedure for magnetization measurements can be described as follows. First, at a given measuring temperature the magnetic field is swept from 0 to a certain value (maximum of 9 Tesla), then decreases (changing sign) to a negative value (minimum of -9 Tesla) then increases back to zero completing one cycle. Measurements were repeated at temperatures in the range 2 K - 200 K.

The result of each cycle is a hysteresis loop which is a plot of magnetization vs. magnetic field. These hysteresis loops are the keys for studying many superconducting and magnetic properties [16], such as: the critical current density, the critical fields H_c, H_{c1} and H_{c2}, energy losses and the remanent magnetic moments. These properties can be calculated from the hysteresis loops using simple magnetic models. In the following chapters, we present some of these measurements for Gd-based and stripe phase superconductors.

CHAPTER 3

Magnetic Properties

3.1 Introduction

Superconductors are perfect diamagnetic materials only below H_{c1}. This means that a superconductor will repel a permanent magnet. In the presence of an applied magnetic field, superconductors have negative magnetization and therefore negative magnetic susceptibility [1],[27].

In this work, gadolinium , Gd, which is paramagnetic above $\sim$ 3 K is being substituted for Y in $YBa_2Cu_3O_{7-\delta}$ in order to study its magnetic effect on superconductivity. Paramagnetism is known to be the behavior of aligning the magnetic moments parallel to an applied magnetic field [20]. A paramagnetic material has a positive magnetization when put in some external magnetic field and therefore has a positive magnetic susceptibility.

Unlike most conventional superconductors, it has been shown that high T_c superconductivity may coexist with strong paramagnetic impurities [28]. A possible reason for this behavior is that the planes containing Y or rare earth magnetic ions are well separated from

the superconducting layers [29]. However, there are some changes because of the paramagnetic contribution.

In conventional superconductors, superconductivity does not coexist with ferromagnetism unless special geometries, like thin films, were considered [19], [20], [30].

In this thesis, we investigate the behavior of the magnetic impurity (Gd) in the high T_c SC, namely $Gd_xY_{1-x}Ba_2Cu_3O_{7-\delta}$. A paramagnetic behavior of the Gd^{3+} moments is expected since it has a very low antiferromagnetic ordering temperature (around 2 K) [31] . In the following section, some of the magnetic properties of the rare earth elements will be studied.

3.2 Why Gd substitution?

There are 14 rare earth elements in the sixth period filling the 4f sublevel (atomic number = 57 to 70) and Gd is one of them. Paramagnetism is exhibited by the rare earth elements (only above some ordering temperature) even when incorporated into solids. The source of this paramagnetism is the partially filled 4f shell [19]. The magnetism of rare earth ions in a solid is best described by treating them as free isolated ions [20]. Gd^{3+} ions have zero orbital angular momentum since they are (f^7) configuration S-state ions. Therefore, Gd ions do not interact to first order with crystalline electric field [28].

Many previous studies were done on substituting rare earth elements for Y in $YBa_2Cu_3O_{7-\delta}$ (YBCO) in order to study the effect of the paramagnetic moment on superconductivity. These studies have improved our understanding of the coexistance of superconductivity

and magnetism in high T_c-superconductors, and the roll of magnetic moments in YBCO [32], [8].

The main objective of having such elemental substitution is to understand the relation between superconductivity and magnetism. Directly after announcing the discovery of high T_c superconductivity [33], [29], [34] many research groups around the world started different elemental substitution experiments i.e. looking for new properties such as magnetic properties and mechanical properties, studying the effect of other elements on this new class of materials and trying to build up a strong theory that can well explain their behavior and properties.

3.3 Changes Caused by Gd Substitution

As seen from Fig. 7, there is a small increase in T_c of YBCO after substituting Gd for Y. The prepared four samples with four different concentrations of Gd and Y, all have the same T_c (~93 K) which is the same for the non-magnetic YBCO superconductor. This implies that the magnetic Gd-ions have no negative effect on T_c, and superconductivity and magnetism may be independent from each other for the system of GdYBCO. Also, this observation supports that superconductivity occurs in the CuO_2 layers since T_c is not changed much when Y is replaced with a magnetic ion. However, T_c is severely affected if some of Cu ions are replaced by magnetic ions [35]. This implies that Gd-ions are not causing pair breaking in Y-based superconductors [36], [37].

Fig. 9 shows magnetization vs. external applied magnetic field for Gd1 at T = 50 K.

The magnetization stays negative as the field increases to about 0.4 T reflecting the presence of superconducting contribution to the total magnetization. At higher fields, the magnetization becomes positive and shows linear increase with field. The positive magnetization is caused by the magnetic contribution of the Gd^{3+} ions present in the sample. It overcomes the negative magnetization caused by the superconducting state. The sample behaves as having two superimposed states: one of them being superconducting (M_{sc}) and the other paramagnetic (M_{para}). The total magnetization is given as:

$$M = M_{sc} + M_{para} \tag{3.1}$$

The M_{para} can be estimated from $((M^{+}+M^{-})/2)$ if the irreversible part of the magnetization is neglected where M^{+} represents the magnetization with increasing magnetic field and M^{-} represents the magnetization with decreasing magnetic field.

In evaluating the thermodynamical properties (such as H_c) of the superconducting state, one has to properly subtract the magnetic contribution of the Gd-ions. This can be achieved by modeling the the paramagnetic conribution to the magnetization.

M_{para} can be fitted using different methods. One of the commonly used techniques is the polynomial fit. Although this method of fitting yields good results (as we will show later), the physics of the problem is usually not clear. No solid conclusions can be made about the paramagnetic contribution after fitting, but meaningless fitting parameters (from a physics point of view).

Another fitting method that can be used is the Brillouin function [20], [19], [8]. This

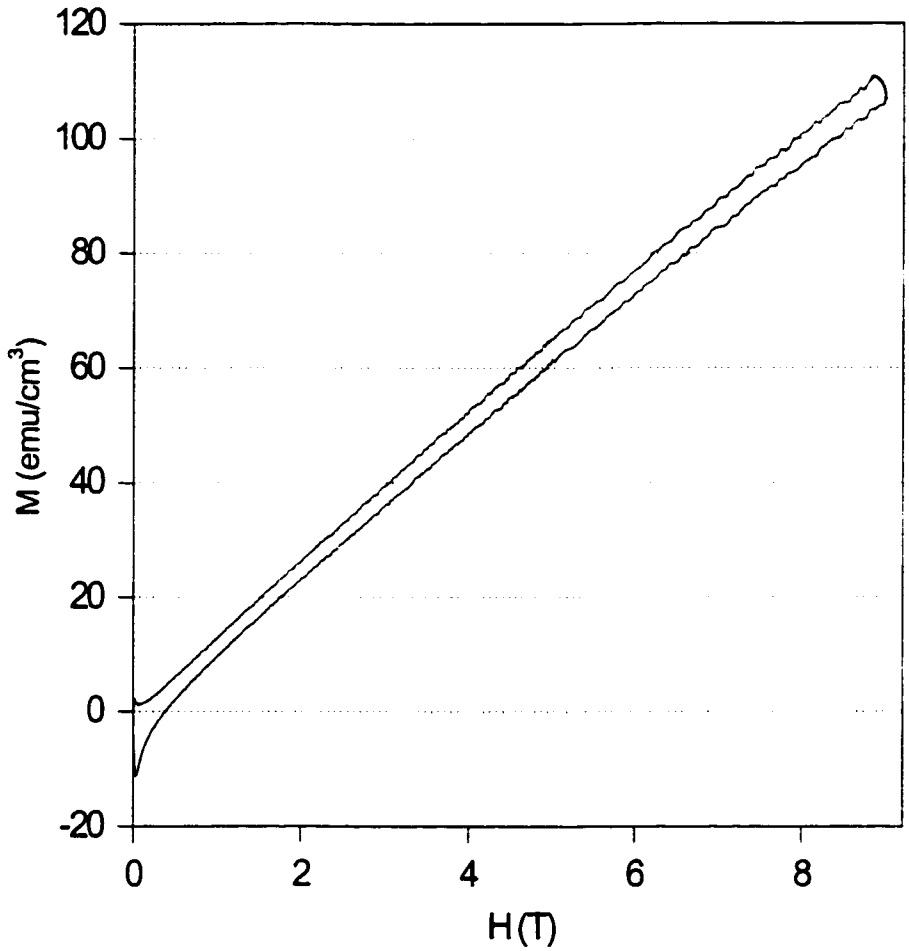

Figure 9: Magnetization hysterisis loop for Gd1 at 50 K in the magnetic field range 0 - 9T.

method has physical meaning and its fitting parameters are related to physical parameters of the material used. A comparison between some of the results obtained using both methods will be discussed in the next chapter. The next section explains the Brillouin function fitting method.

3.4 Brillouin Function

In an applied magnetic field, a paramagnetic atom with angular momentum quantum number J has a magnetization given by:

$$M = NgJ\mu_B B_J(x) \tag{3.2}$$

where

$$x \equiv \frac{gJ\mu_B B}{k_B T} \tag{3.3}$$

N: the total number of magnetic ions

g: the Lande factor (g=2 for free Gd^{3+} ions)

μ_B : Bohr magneton (μ_B=9.27410 X 10^{-24} J T^{-1})

k_B: Boltzmann constant (k_B = 1.38062 X 10^{-23} J K^{-1})

J: the total angular momentum (J=7/2 for Gd^{3+} ions) [19]

and the Brillouin function B_J is defined as [31]

$$B_J(x) = \frac{2J+1}{2J}\,\mathrm{ctnh}\left(\frac{(2J+1)}{2J}\,x\right) - \frac{1}{2J}\,\mathrm{ctnh}\left(\frac{x}{2J}\right) \tag{3.4}$$

Since Gd-atoms behave paramagnetically above T~2 K (ordering temperature), one can apply Brillouin function to calculate its paramagnetic contribution to the magnetization. The Brillouin function nicely describes the paramagnetic moment of Gd^{3+} free ions at high magnetic fields (H) and high temperatures (T). The agreement is not good at low field and low temperature regimes [8]. This disagreement is due to the antiferromagnetic interactions at low temperatures and low fields and should therefore be considered in this study. The Brillouin function should be extended. This can be done by having x proportional to $1/(T+\theta_N)$ rather than 1/T

$$x \equiv \frac{gJ\mu_B B}{k_B(T+\theta_N)} \tag{3.5}$$

where θ_N is a fitting parameter usually larger than the ordering temperature T_N ($\approx$ 2.1 - 2.6 K) for Gd^{3+} ions.

Now, one can use the extended Brillouin function to fit the paramagnetic contribution due to Gd^{3+} ions in the GdYBCO samples and subtract that contribution to get the superconducting contribution to the total magnetization. In the following section, the method used for fitting and subtracting the paramagnetic contribution to the total magnetization is described.

3.5 Technique Used for Fitting and Subtracting the Paramagnetic Contribution

A Fortran program was used to fit the paramagnetic contribution of Gd^{3+} ions in GdY-BCO samples using the extended Brillouin function. A set of experimental data composed of the values of the magnetization M at high values of H (the applied magnetic field $\approx 4-9$ T) are supplied as an input. The program looks for the best fit using the extended Brillouin function and generates new values for M at all values of H and minimizes the difference between the two sets of M. The output of the program is the θ_N value which is the fitting parameter in equation (3.5). In appendix A, the fitting program is listed.

Then, this θ_N value is used in another Fortran program in order to generate M values for the paramagnetic moments due to Gd^{3+} ions at all values of H (0-9 T) including (0,0) point. This program also uses the extended Brillouin function and is listed in appendix B.

These two Fortran programs were used on data for all of the four GdYBCO samples at all temperatures to find first the fitting parameter θ_N and then to generate the paramagnetic contribution due to the existence of the Gd^{3+} ions in these samples.

Fig. 10 shows the steps of the technique. It shows first the hysteresis loop of Gd1 at 60 K which contains both superconducting and paramagnetic contributions to the magnetization. It also shows the average of the two branches of the hysteresis loops, namely M^+ and M^-. This average is incorporated into the Fortran program for fitting. Fig. 10 also shows M_{para} generated after fitting, using the extended Brillouin function with θ =9.6 K. The final step of the process is the subtraction of M_{para} from the average Hysteresis loop to get the

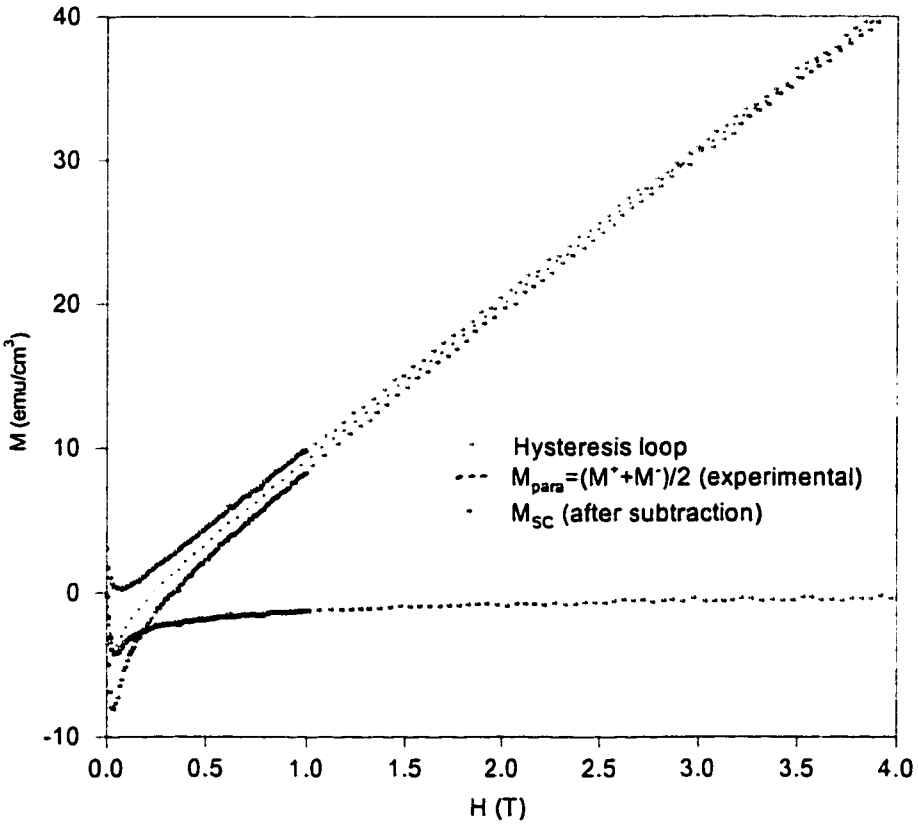

Figure 10: Steps of the procedure applied to Gd1 at 60 K with θ =9.6

TABLE 7: Variation of θ_N (K) with temperature for various samples used in this study

T	55 K	60 K	65 K	70 K	80 K
Gd1	11.3	9.6	9.7	10.0	11.6
Gd2	11.8	12.1	12.3	12.5	13.9
Gd3	12.0	12.3	13.0	14.7	15.9
Gd4	13.2	14.8	11.8	15.6	14.5

superconducting contribution to the total magnetization.

Other examples of the procedure applied to Gd2, Gd3 and Gd4 samples are shown in figures 11, 12 and 13, respectively.

Table 7 shows θ_N values (in units of K) for different samples at different temperatures detemined experimentally using the extended Brillouin function. One notices that θ_N changes slightly with temperature. This is accepted within the experimental errors for magnetization measurements which is in the order of 5 %.

In the following chapters, the properties of the superconducting contribution (after subtraction) will be discussed.

3.6 Magnetic Susceptibility

It was mentioned at the beginning of this chapter that χ (the dimensionless magnetic susceptibility) should be +ve for paramagnetic materials. In order to make sure that the interaction of our samples is paramagnetic, we found χ for each one of them vs. T. χ vs. 1/T for GdYBCO samples are presented in Fig. 14.

According to the Curie-Weiss model [19], χ (the paramagnetic susceptibility) can be written as

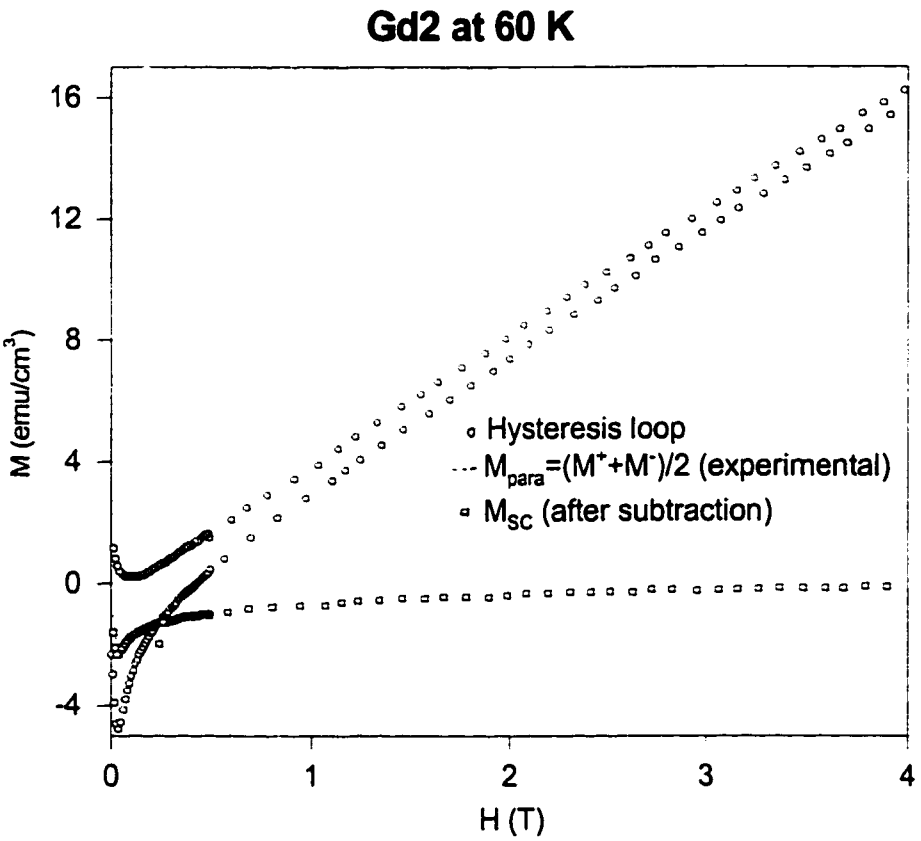

Figure 11: Steps of the procedure applied to Gd2 at 60 K with θ =12.1

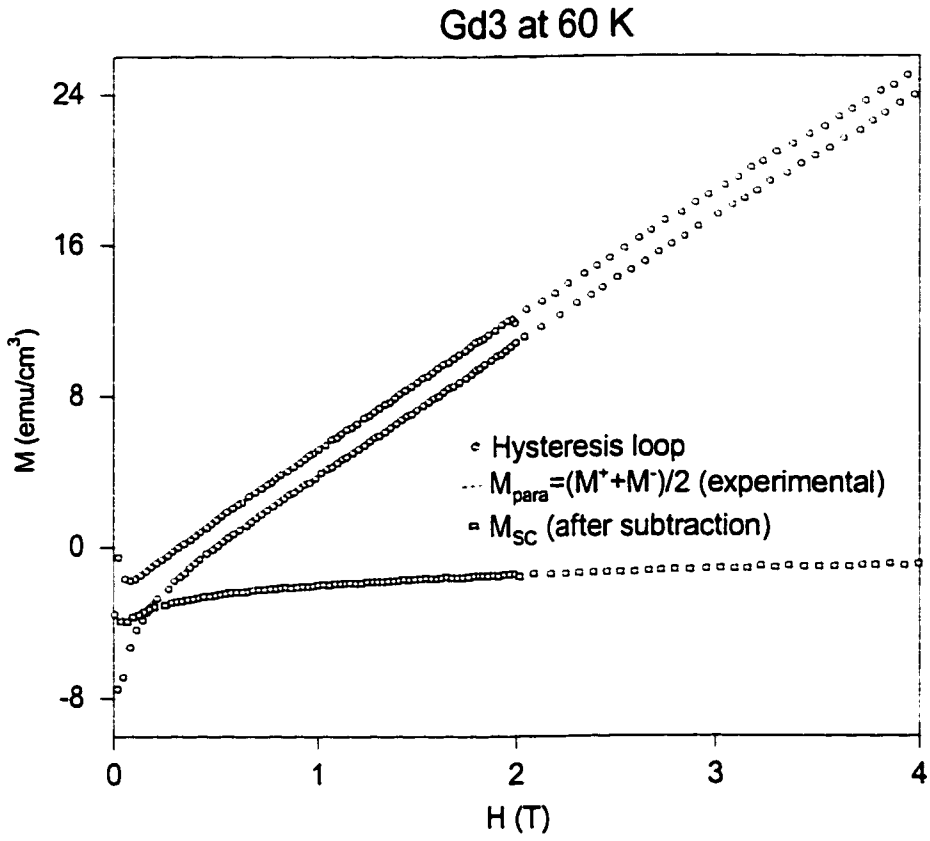

Figure 12: Steps of the procedure applied to Gd3 at 60 K with θ =12.3

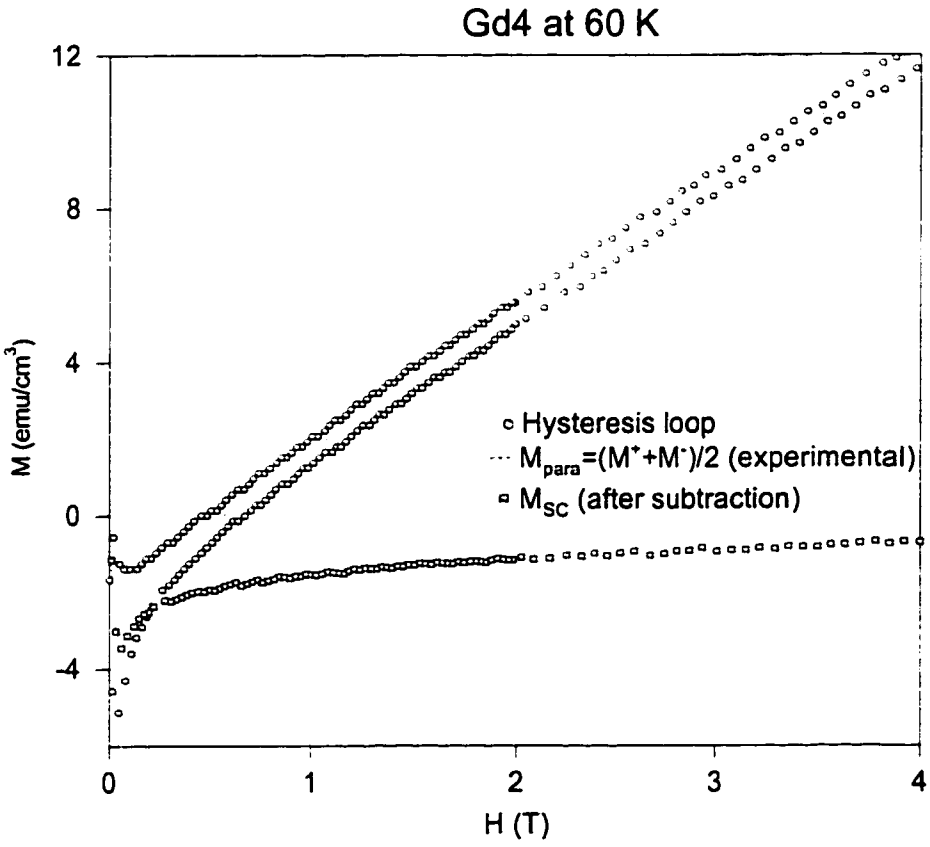

Figure 13: Steps of the procedure applied to Gd4 at 60 K with θ =14.8

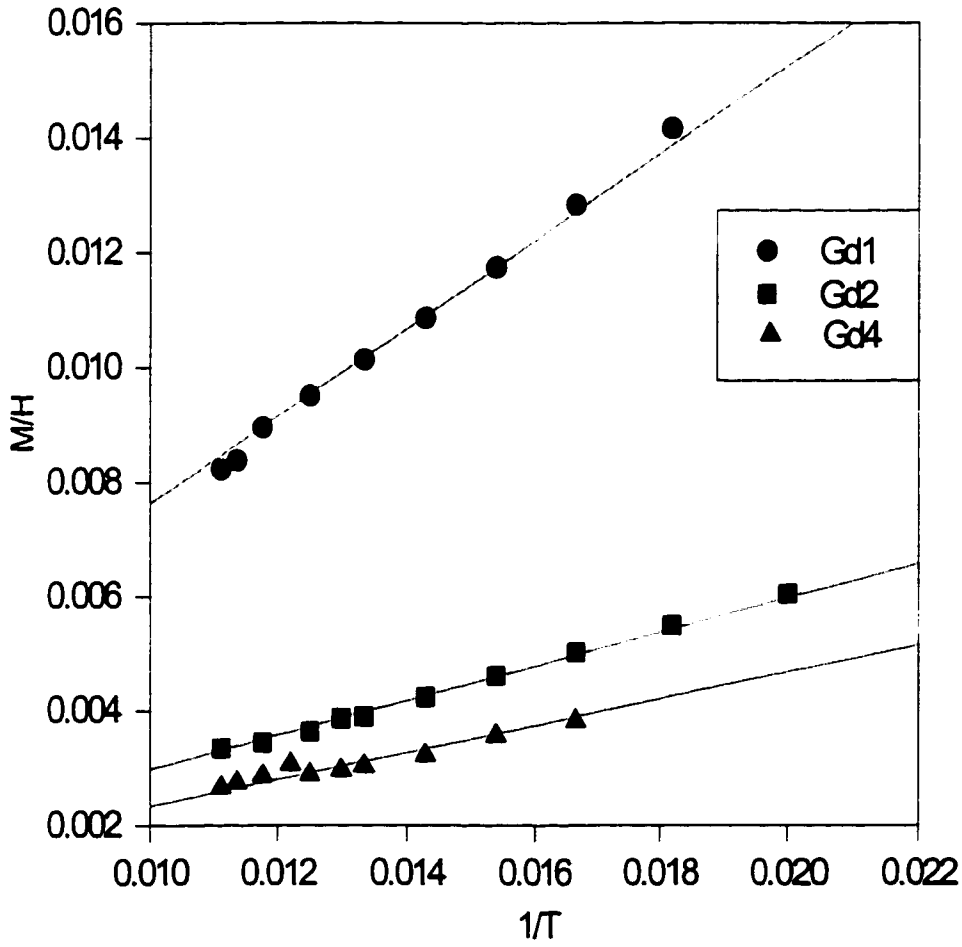

Figure 14: χ = (M/H) vs. 1/T for Gd1, Gd2 and Gd4 (The lines represent the linear fits).

TABLE 8: Curie-Weiss constant (C) for some of the samples compared with the calculated values

	Gd1	Gd2	Gd4
C calculated	0.751	0.249	0.201
C experimental	0.763	0.299	0.234
% Difference	1.6	20	16

$$\chi = \frac{C}{T - \theta} \tag{3.6}$$

where C is the Curie-Weiss constant (in units of $\frac{\text{emu K}}{\text{Oe cm}^3}$) and is given by

$$C = \frac{Np^2\mu_B^2}{3k_B} \tag{3.7}$$

where p is the effective number of Bohr magneton defined as $p \equiv g[J(J+1)]^{1/2}$. It is obvious from equation (3.6) that C can be calculated from the slope of a χ vs. 1/T graph.

To check for the paramagnetic behavior of the Gd samples, a comparison will be made between the calculated C constant using equation (3.6) with C calculated experimentally via the slope of χ vs. 1/T graph. The comparison is shown in Table 8.

In the following chapter will study the thermodynamic properties of the GdYBCO system.

CHAPTER 4

Thermodynamic Properties

4.1 Introduction

Superconductors exhibit diamagnetic response to an externally applied magnetic field. As the field increases above a critical value (H_c), a second order transition to non-superconducting state occurs in type I superconductors (there is no latent heat of transition at T_c [19]). The transition from superconducting to normal state is sharp as seen in Fig 15A.

The situation is different in the case of type II superconductors (SC). The transition to normal state occurs gradually passing through a mixed state which is limited by two critical magnetic field values, namely H_{c1} and H_{c2} [38]. A type II SC will exhibit perfect diamagnetic behavior only below H_{c1}. Above H_{c1}, the flux penetrates the SC partially and the sample becomes in a complicated microscopic structure of both normal and superconducting regions known as the mixed state [20], see Fig. 15B.

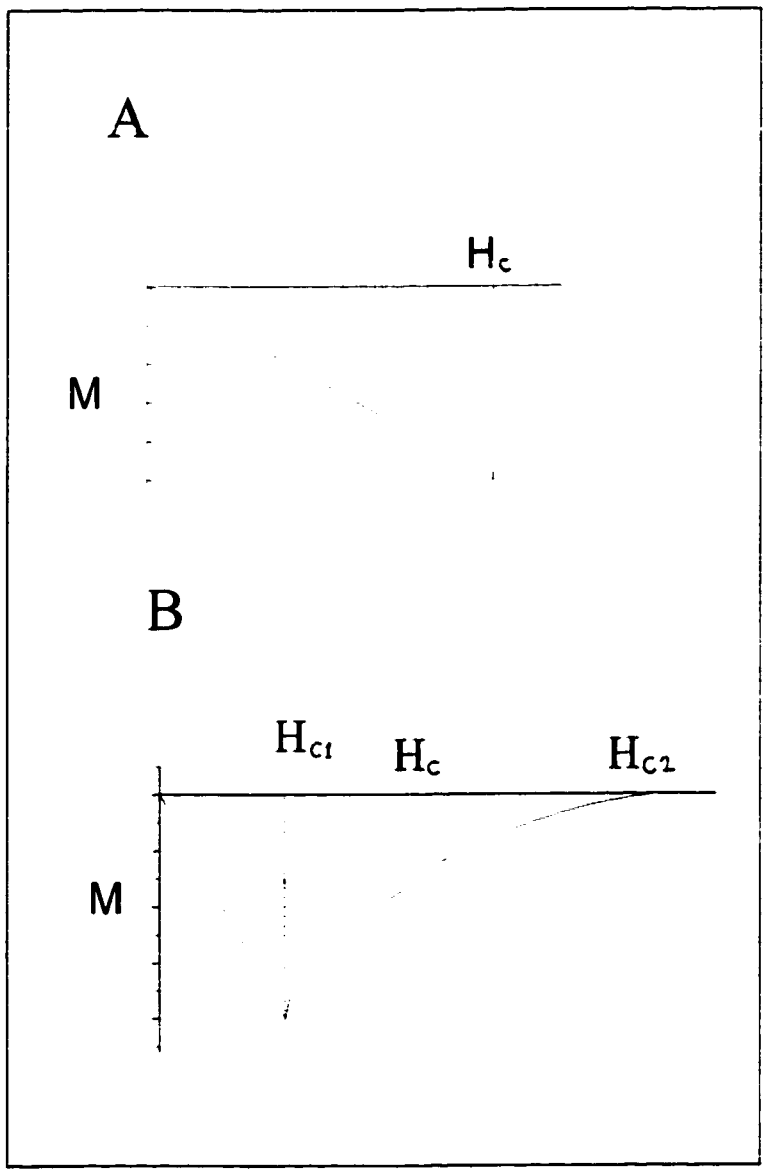

Figure 15: A- Sharp transition from superconducting to normal state at H_c in type I superconductors. B- magnetization curve of type II superconductor showing H_{c1}, H_c and H_{c2}.

4.2 Thermodynamic Critical Field

Because the phase transition (from normal state to SC state and vice versa) is reversible, thermodynamics can be applied to the superconducting materials [2], [21]. From thermodynamics, the area under the reversible magnetization curve is given by

$$Gn - Gs = \int_0^{H_{c2}} \mathrm{M\ dH} = \frac{\mathrm{H_c^2}}{8\pi} \tag{4.1}$$

This relation serves as a definition of H_c [39], [40]. This is why H_c is called thermodynamic critical field. Geometrically, It has a value between H_{c1} and H_{c2} (i.e. $H_{c1} < H_c < H_{c2}$) as shown in Fig. 15.

In order to be able to calculate H_c precisely, we should have a wide range of reversible magnetization in the hysteresis loops [21]. For these four Gd doped samples, we have nearly similar reversible magnetization specially at high temperatures near T_c (85-93 K) (see Fig. 16). So, we expect better results of H_c at high temperatures than at low temperatures. At all temperatures, Gd1 has the highest reversible field.

Equation (4.1) will be discussed later in the section about free energy.

4.3 Methods of Calculating H_c

There are several methods to calculate H_c for type II superconductors. One of these methods is to calculate H_c by determining H_{c2} and κ (defined in section 1.2) experimentally,

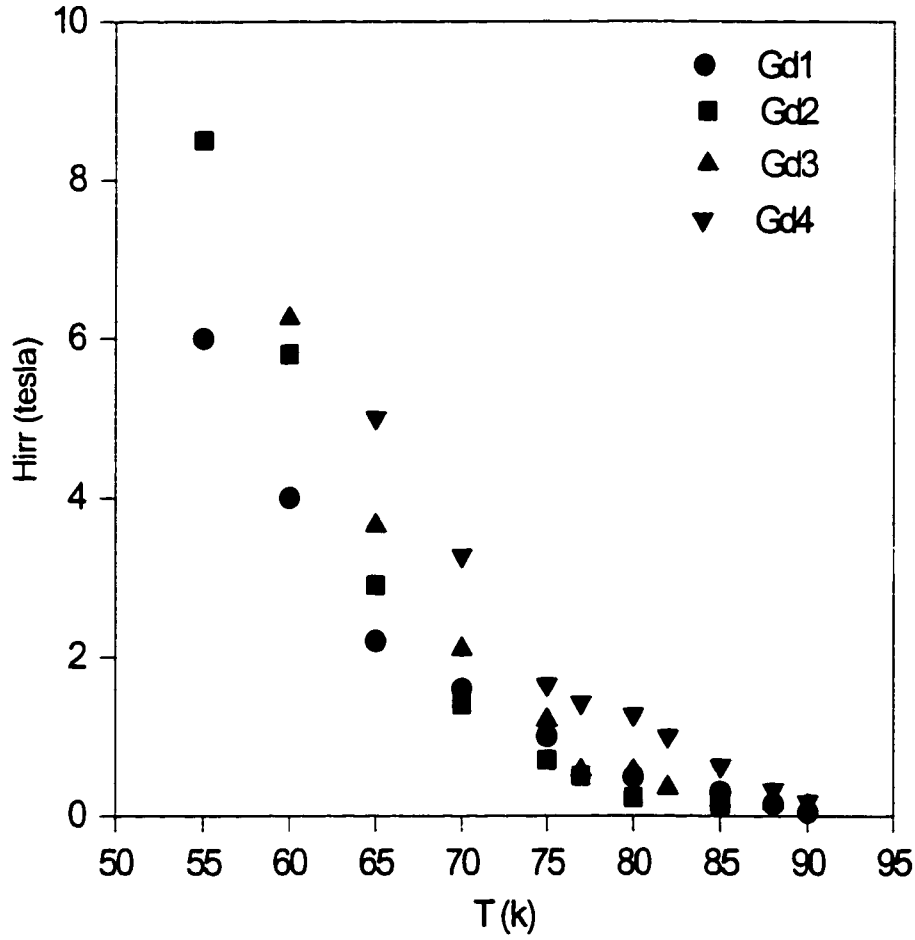

Figure 16: H_{irr} vs. T for the Gd doped four samples.

then to find H_c using the relationship:

$$H_c = \frac{H_{c2}}{\sqrt{2}\kappa} \tag{4.2}$$

However, This is not an easy job because of the difficulties in obtaining both H_{c2} and κ experimentally.

There is another method that uses the Hao-Clem model and Ginzberg-Landau order parameter to fit the reversible magnetization. This method is explained in reference [41] . It assumes that H_c and κ are independent fitting parameters for the magnetization data. Moreover, it is applicable only for a narrow range of temperatures near T_c. In reference [41], H_c was calculated for the temperature range 82-89 K in $YBa_2Cu_3O_7$.

H_c can also be calculated using the specific heat analysis method as in references [42] and [43]. In this method, H_c is obtained by integrating the entropy difference between the normal and superconducting states according to the following relation:

$$\frac{\mu_0 H_c^2(T)}{2} = \int_{Tc}^{T}\int_{Tc}^{T'} \frac{(C_s - C_n)}{T''}\, dT''\, dT' \tag{4.3}$$

In this study, we used a method which depends on the condensation energy. The next section explains this method and our results.

4.4 Free Energy Method of Calculating H_c

In section (4.2), the definition of H_c was given in terms of thermodynamic arguments. The equation (4.1) can be used to calculate H_c. The left hand side of this relation

$$Gn - Gs = \int_0^{H_{c2}} MdH = \frac{H_c^2}{8\pi} \tag{4.4}$$

represents the condensation energy of the electrons in the superconducting state (the free energy difference between the normal and superconducting states) where Gn is the Gibbs free energy of the normal state and Gs is the energy of the superconducting state [2]. According to this relation, the area under the magnetization curve should ideally equal the free energy difference between the SC state and the normal state. The free energy difference can be defined as the required energy to have a transition from the normal state to the superconducting state and it is also called the condensation energy. The area is evaluated graphically. Then by substituting the area into equation (4.1), one can obtain H_c (the thermodynamic critical field).

The difficulty in applying this relation to high-T_c superconductors arises from the fact that H_{c2} is very high, and the reversible magnetization region is relatively limited to a narrow range in H and T [41]. As mentioned in chapter 3, it was noticed that after performing the paramagnetic subtraction the magnetization becomes almost zero at magnetic field values much less than H_{c2}, see for example Fig. 17. The magnetization becomes zero at H $\approx$ 3.5 T at T = 70 K, therefore, one can evaluate the integral from 0 to 3.5 T without having

to warry about the value of H_{c2} since the contribution to the area from 3.5 tesla to H_{c2} is approximately zero.

The H_c values for Gd1, Gd2, Gd3 and Gd4 at different temperatures are shown in Fig. 18. To see the effect of paramagnetic contribution on the H_c values, the figure also shows the published data of H_c values obtained for the pure $YBa_2Cu_3O_{7-\delta}$ using Clem-Hao model [41].

A polynomial fit has been used to fit the magnetization curve at high fields. The paramagnetic contribution was then subtracted from the total magnetization to obtain the superconducting state contribution to the magnetization. The obtained values for H_c are shown in Fig. 19 along with the values obtained using the extended Brillouin function fit for the Gd1 sample. The results obtained from both methods are comparable.

By inspecting Fig. 18, it can be concluded that the H_c vs. T curves are similar (within the experimental error) for different concentrations of Gd in GdYBCO samples. Therefore, one can safely say that the law of corresponding states is obeyed. The BCS law of corresponding states is:

$$\frac{H_c(T)}{H_c(0)} = 1 - \left(\frac{T}{T_c}\right)^2 \tag{4.5}$$

However, these H_c values are different from the published data for the pure $YBa_2Cu_3O_{7-\delta}$ system.

If one fits the H_c vs. T curves in Fig. 18 by linear fit, then the slope near T_c:

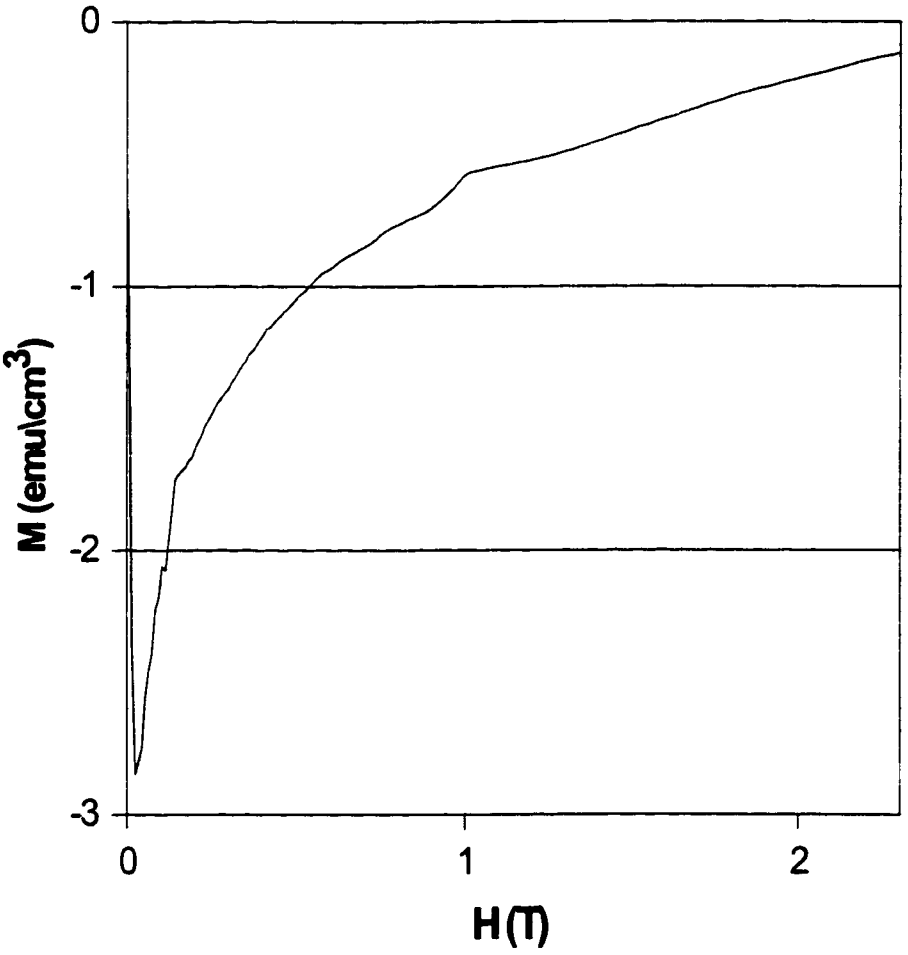

Figure 17: Magnetization curve for Gd1 at T=70 K showing the SC contribution only after subtracting the paramagnetic contribution.

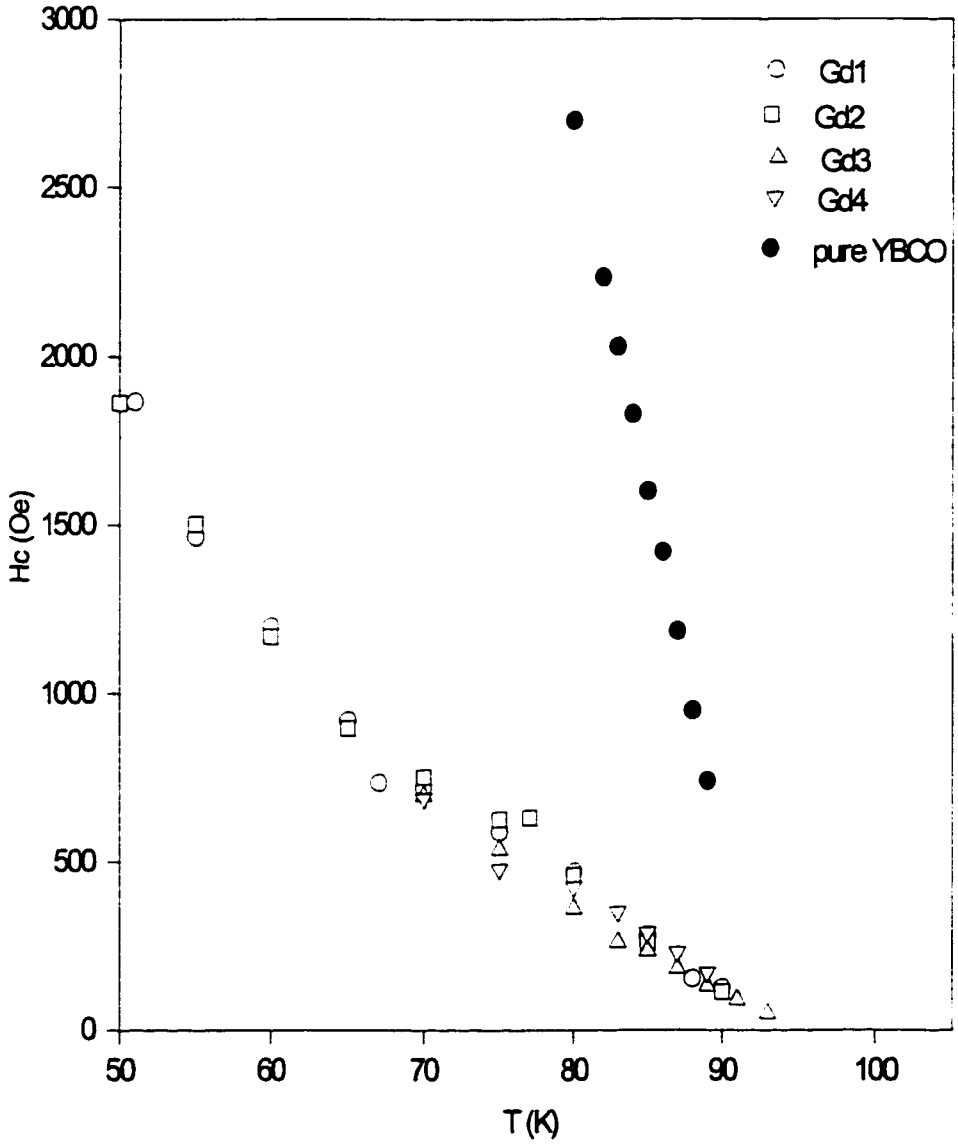

Figure 18: The thermodynamic critical field H_c vs. temperature for the Gd doped four samples. H_c values for pure YBCO system is shown for comparison.

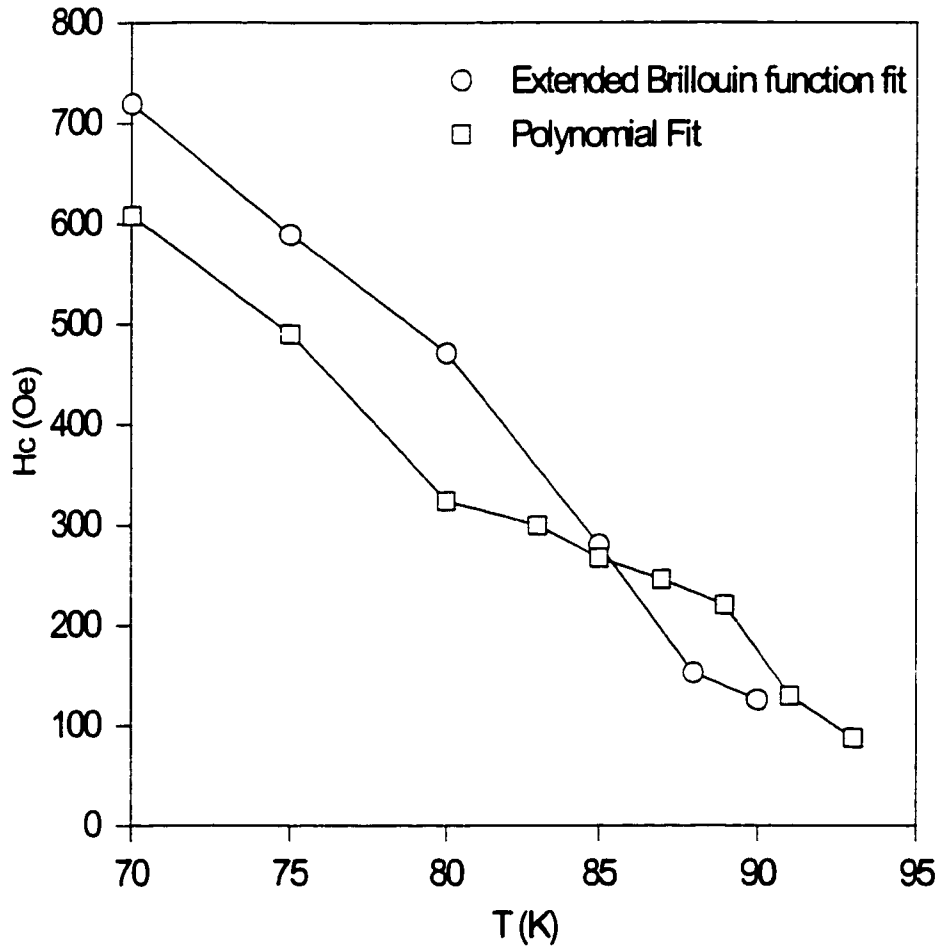

Figure 19: Comparison between the values of H_c for the Gd3 sample obtained using both the extended Brillouin function fit and the polynomial fit (the lines are guides for the eye).

$$\frac{dH_c}{dT} \approx -30 \text{ Oe/K} \tag{4.6}$$

where the published value of $\frac{dH_c}{dT}$ for the pure $YBa_2Cu_3O_{7-\delta}$ is -220 Oe/K. This slope of the critical field at T_c is related directly to the step change ΔC of the heat capacity at T_c through [44]:

$$(\frac{dH_c}{dT})_{T_c} = (\frac{4\pi\Delta C}{V T_c})^{1/2} \tag{4.7}$$

where V is the molar volume.

By extrapolating the H_c to the T-axis, these curves cut the T-axis at a value of 94 K which is very near to the value of T_c for these compounds (about 93 K).

Finally, the effect of annealing the sample in O_2 on the value of H_c was observed. The Gd3 sample was annealed for an extra 24 hours. A noticeable increase in the H_c values can be clearly seen in Fig. 20, with about 30% increase in the slope near T_c. The possible reason for this change is the increase in the superconducting fraction by annealing the sample in O_2. Further investigations of the effect of oxygen contents on the thermodynamic critical field are being planned in the lab.

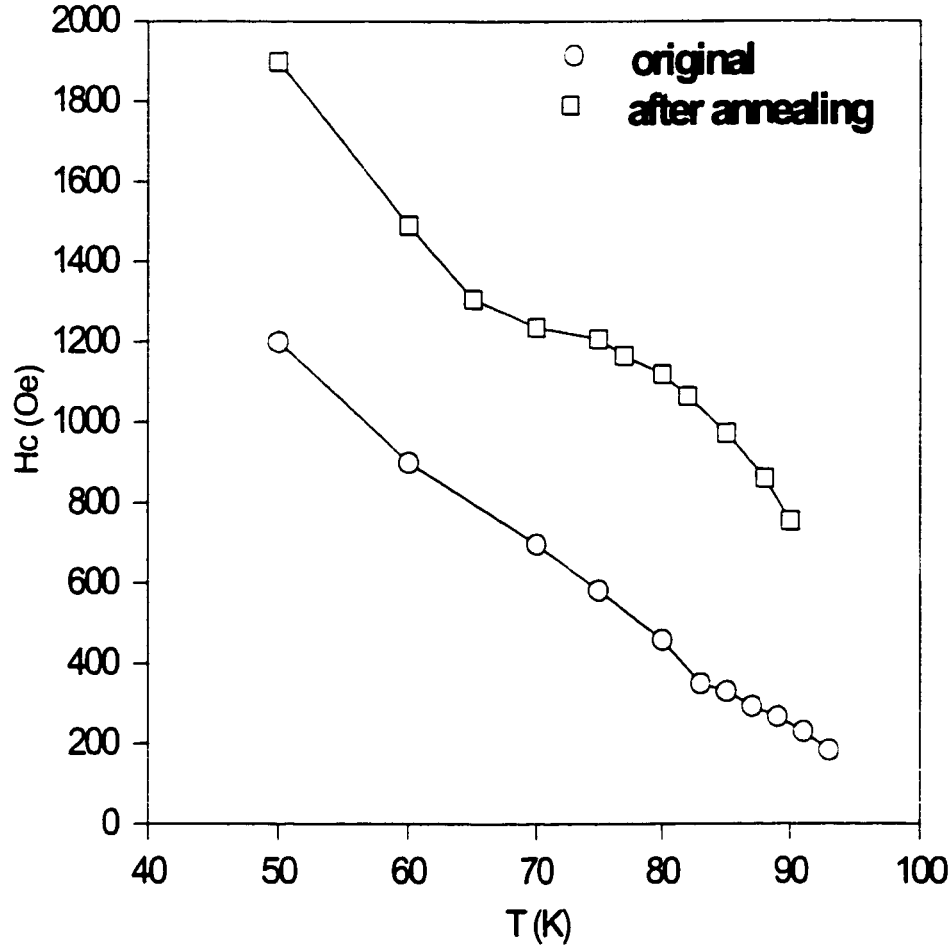

Figure 20: Comparison between H_c values for Gd3 sample before and after annealing in O_2 for 24 hours.

4.5 BCS Coupling

The BCS theory predicts that the critical field H_c closely obeys the relation

$$H_c(T) = H_c(0)\left(1 - \frac{T^2}{T_c^2}\right) \tag{4.8}$$

where $H_c(0)$ is the value of H_c at $T = 0$ and T_c is the temperature at which the transition takes place in zero field [21]. The prediction of BCS for $H_c(T)$ is often expressed in terms of the deviation from the empirical law:

$$D = \frac{H_c(T)}{H_c(0)} - \left[1 - \left(\frac{T}{T_c}\right)^2\right] \tag{4.9}$$

The deviation can be considered as being a measure of the electron-phonon coupling strength [20], [42]. The deviation function of thermodynamic critical field vs. the reduced temperature $(T/T_c)^2$ is shown in Fig. 21. This figure shows that all the GdYBCO samples have weak coupling behavior with a maximum deviation of about 20 % from the BCS behavior. Weak coupling means that the superconducting pairing energy is negligible compared to the phonon energies [4]. The deviation also conveys that the law of corresponding states is being obeyed with an estimated error of about 20 %. One possible reason for this relatively high deviation from BCS coupling is that the magnetic moments of Gd are affecting the electron-phonon interaction. Electron-phonon interaction is believed to be responsible for the formation of superconducting cooper pairs [44].

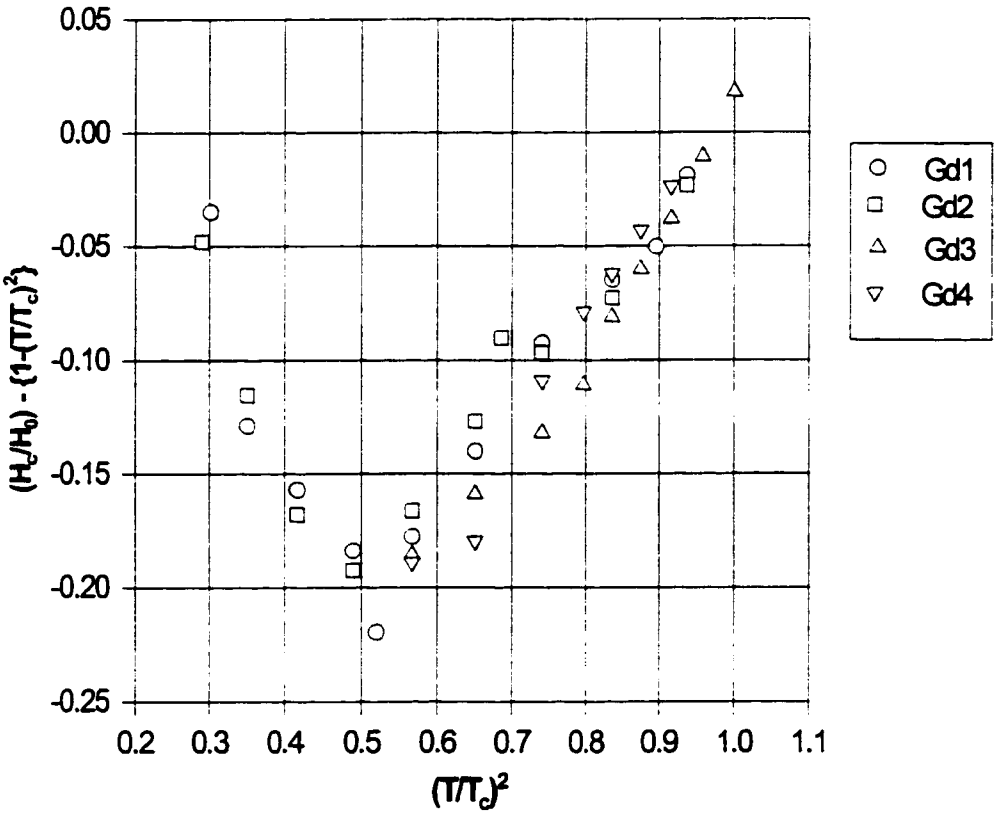

Figure 21: The deviation function of the thermodynamic critical field vs. $(T/T_c)^2$ for the four Gd doped samples.

CHAPTER 5

Scaling of the Critical Current Density and the Pinning Force

5.1 Introduction

The critical current is defined as the highest current that can flow through a particular superconducting material before the material transforms to normal state. This means that superconducting materials are usable only for passing currents lower than the critical current density J_c, expressed in A/cm^2 [5], [38].

Many practical applications of superconductors require high values of J_c which vary in magnitude according to application. For example, superconducting wires for magnetic field generators require values of J_c in the order of $10^4 A/cm^2$. Therefore, various research projects in SC have focused on methods to improve J_c values and develop superconducting materials with high values of J_c [45], [38]. It has been found that the measured values of J_c depends on many criteria such as the exact shape of the sample, the experimental technique used and the relationship between the J value and the applied magnetic field (H) [15].

There are several methods to determine the J_c values, namely:

1. The transport method using the V-I characteristics (from applied voltage V vs. current I curves). This method is called a transport method because charges are transported into and out of the SC material using a current source. A criteria of 1 μV is commonly used to determine the critical current.
2. The magnetic method using the width of the hysteresis loops. In this method the measured current is the screening current that arises to shield the SC material from an applied magnetic field [2].
3. The inductive method which includes using the ac susceptibility through its imaginary part χ''.

For more details on each of these methods and the differences between them refer to ref. [15].

In early sixties, Bean [46] proposed his critical state model in which the critical current density is proportional to the width of the hysteresis loop. In Bean's model the main assumption is that for applied fields higher than the full penetration field H^*, the critical current density is independent of the applied magnetic field, i.e.

$$J_c(H) = J_c(0) \tag{5.1}$$

where $J_c(0)$ is the critical current density at zero applied field [47]. Bean's model assumes that the critical current flows in the sample to prevent the penetration of flux and relates the

width of the hysteresis loop with the J_c values through the following relationship:

$$J_c = 17\frac{\Delta M}{R} = \alpha \Delta M \tag{5.2}$$

where $\Delta M = M^+ - M^-$ (the difference between the increasing and decreasing field magnetization density, respectively) in units of emu/cm^3, R is the average radius of the grain size ($\approx$ 10 microns = 1 x 10^{-4}cm) and α is a constant which depends on the geometry of the sample. This method usually gives results which are comparable to those obtained by the direct transport method [48], but with the advantage over the direct method since it does not require electrical contacts [4].

One drawback of this model is that it is not applicable above H_{irr} since the two branches of the hysteresis loop collapse and the width of the hysteresis loop becomes zero where the pinning force may not vanish. This implies that the model gives zero values for J_c at applied magnetic field values above H_{irr}. However, Bean's model is still widely used to calculate J_c [15].

It should be mentioned that the critical current density depends on the temperature. It decreases as the temperature increases until it reaches zero at T_c. The critical current density also depends on the applied magnetic field. The critical current density for many HTSCs has high values at low applied magnetic fields, then it drops sharply at higher fields [2].

It is worth mentioning that the Silsbee's hypothesis is very well applied to predict critical currents of type I superconductors [2]. This hypothesis is based on the fact that, the sum of the applied magnetic field and the magnetic field due to the current should not exceed H_c.

The situation is different in type II SCs because they have two critical field values H_{c1} and H_{c2}. It is very important to know that the critical current of a type II SC in the mixed state is not determined by the Silsbee's hypothesis but by impurities and imperfections present in the material [2].

In the following section the Bean's model will be used to calculate J_c for the Gd-Y(123) four samples. The pinning force (PF) will be calculated, then we introduce our scaling method for both J_c and PF using thermodynamic critical field H_c.

5.2 Critical Current Density

Equation (5.2) has been used to evaluate J_c for the four samples of $Y_{1-x}Gd_xBa_2Cu_3O_{7-\delta}$ with x = 1, 0.75, 0.50 and 0.25. The results are presented in part (A) of Figures 22, 23, 24, and 25. The variation of J_c with the applied magnetic field are shown on semi-log plots. The critical current density J_c follows a similar behavior in the four samples. Initially J_c is very large at low field, then rapidly decreases with increasing field and becomes zero at H_{irr} where the two branches of the hysteresis loop collapse and the width of the hysteresis loop is zero. It is known that at high temperatures and high magnetic fields, the critical current density J_c decreases rapidly due to the weak pinning strength. The relation between H_{irr} and the pinning mechanism has not been yet clarified quantitatively [49].

Another point to be added is the effect of Gd content on J_c values. Fig. 26, is a presentation of the variation of J_c with fields for Gd1, Gd2, Gd3, and Gd4 at 75 K. At any given field, the critical current density increases with increasing Gd content in the sample.

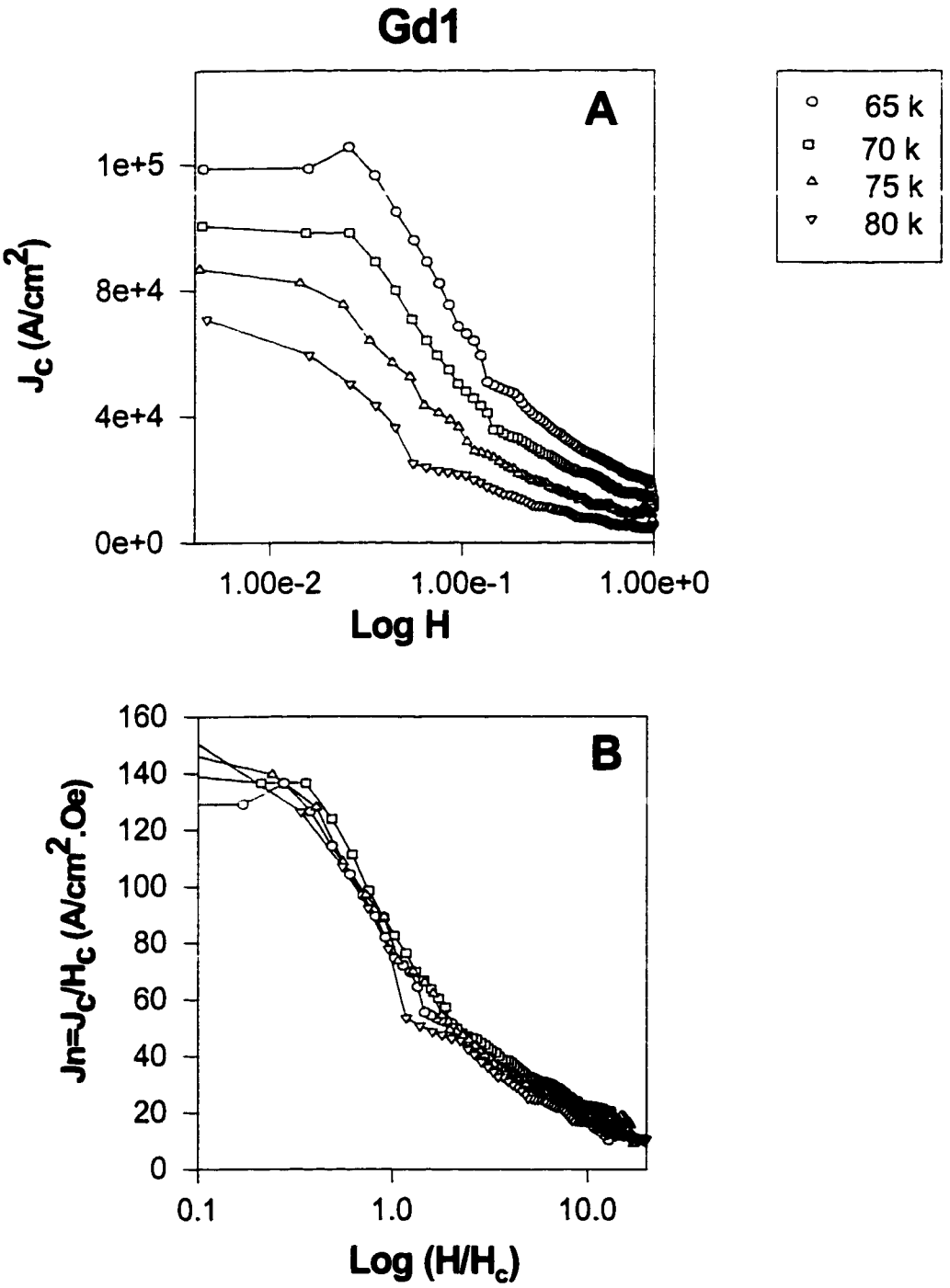

Figure 22: A) J_c vs Log(H) for Gd1 at various temperatures. B) Scaling of J_c using the critical thermodynamic field H_c.(the lines are guides for the eye)

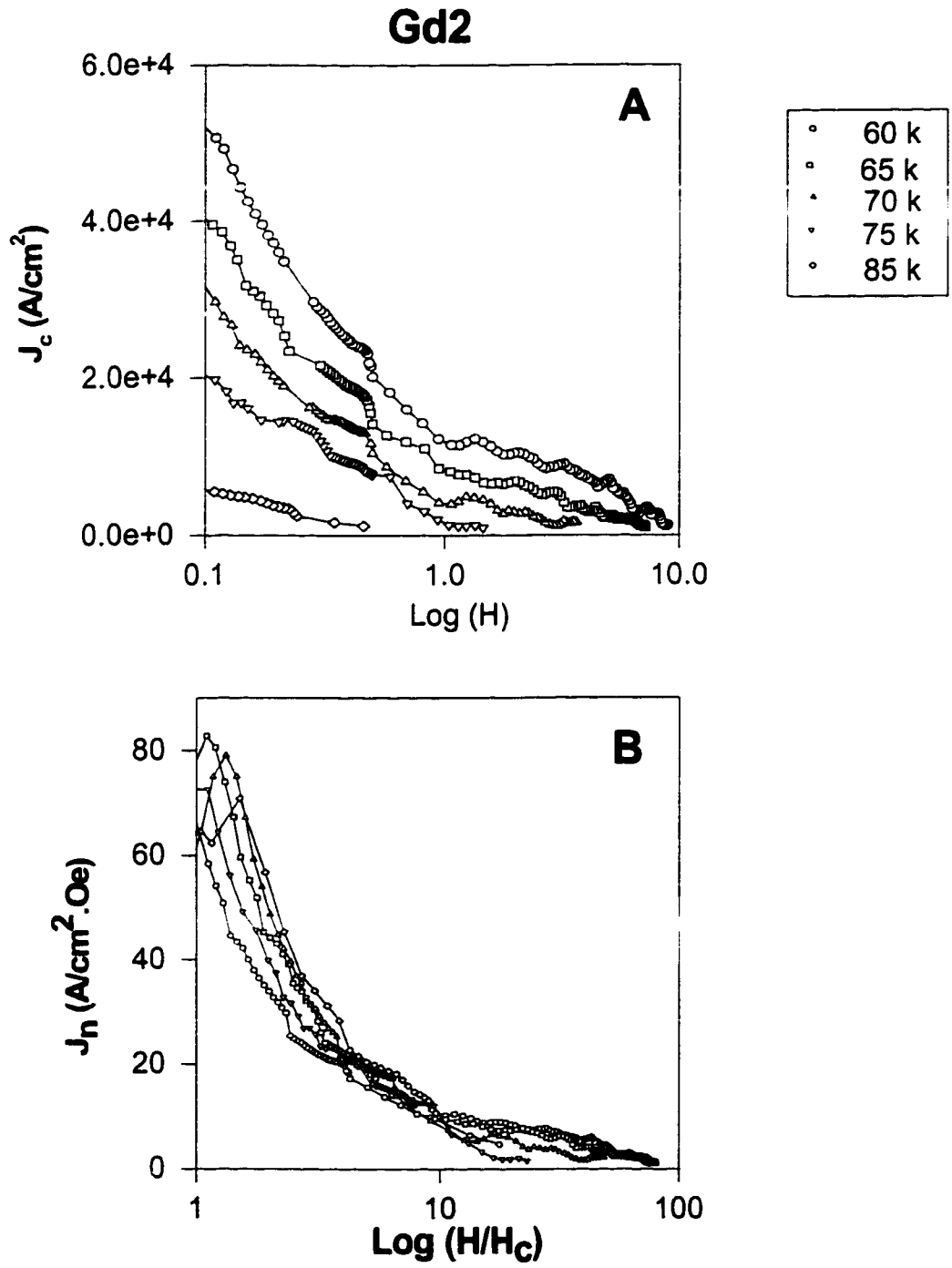

Figure 23: A) J_c vs Log(H) for Gd2 at various temperatures. B) Scaling of J_c using the critical thermodynamic field H_c.(The lines are guides for the eye)

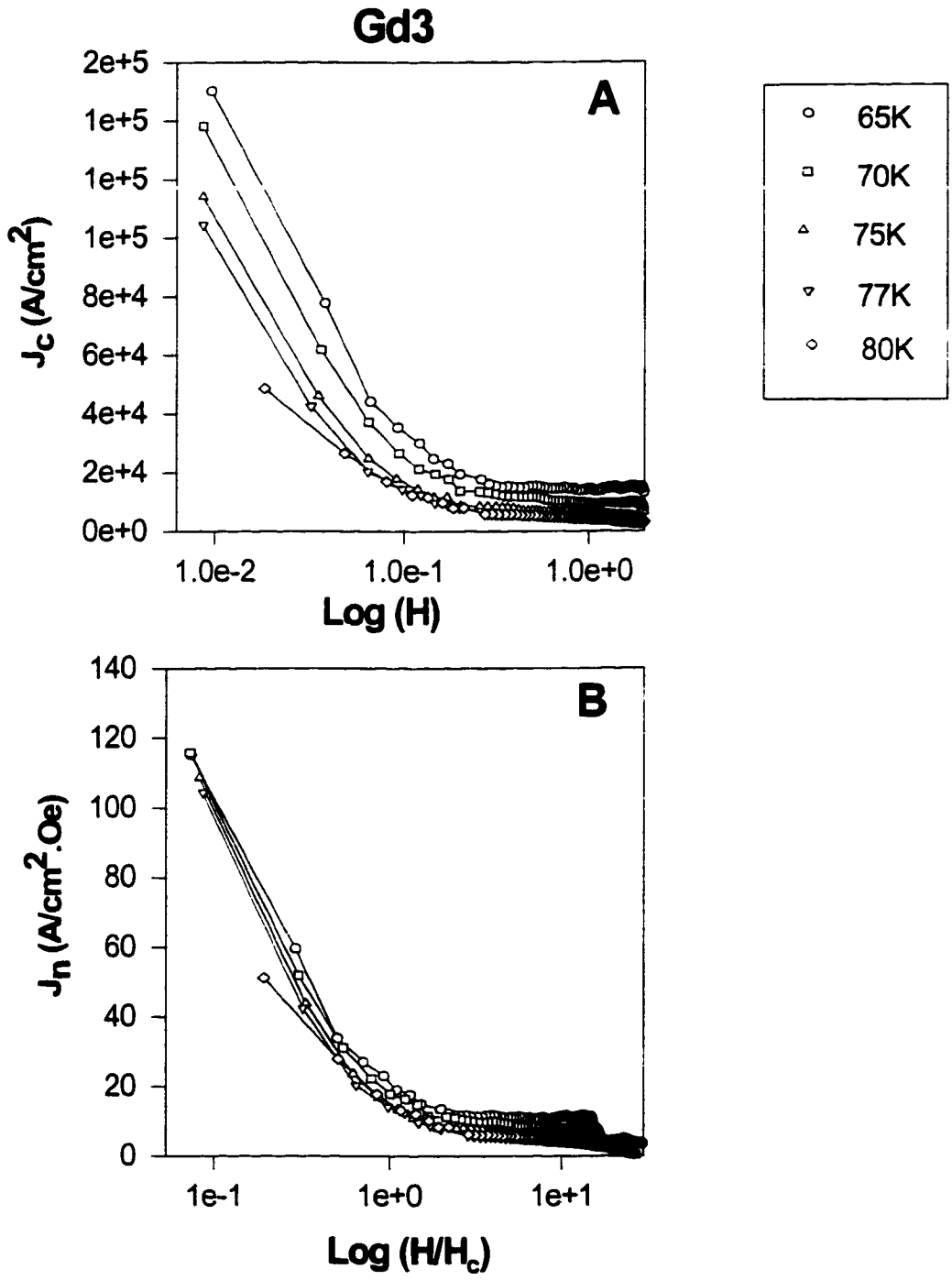

Figure 24: A) J_c vs Log(H) for Gd3 at various temperatures. B) Scaling of J_c using the critical thermodynamic field H_c.(The lines are guides for the eye)

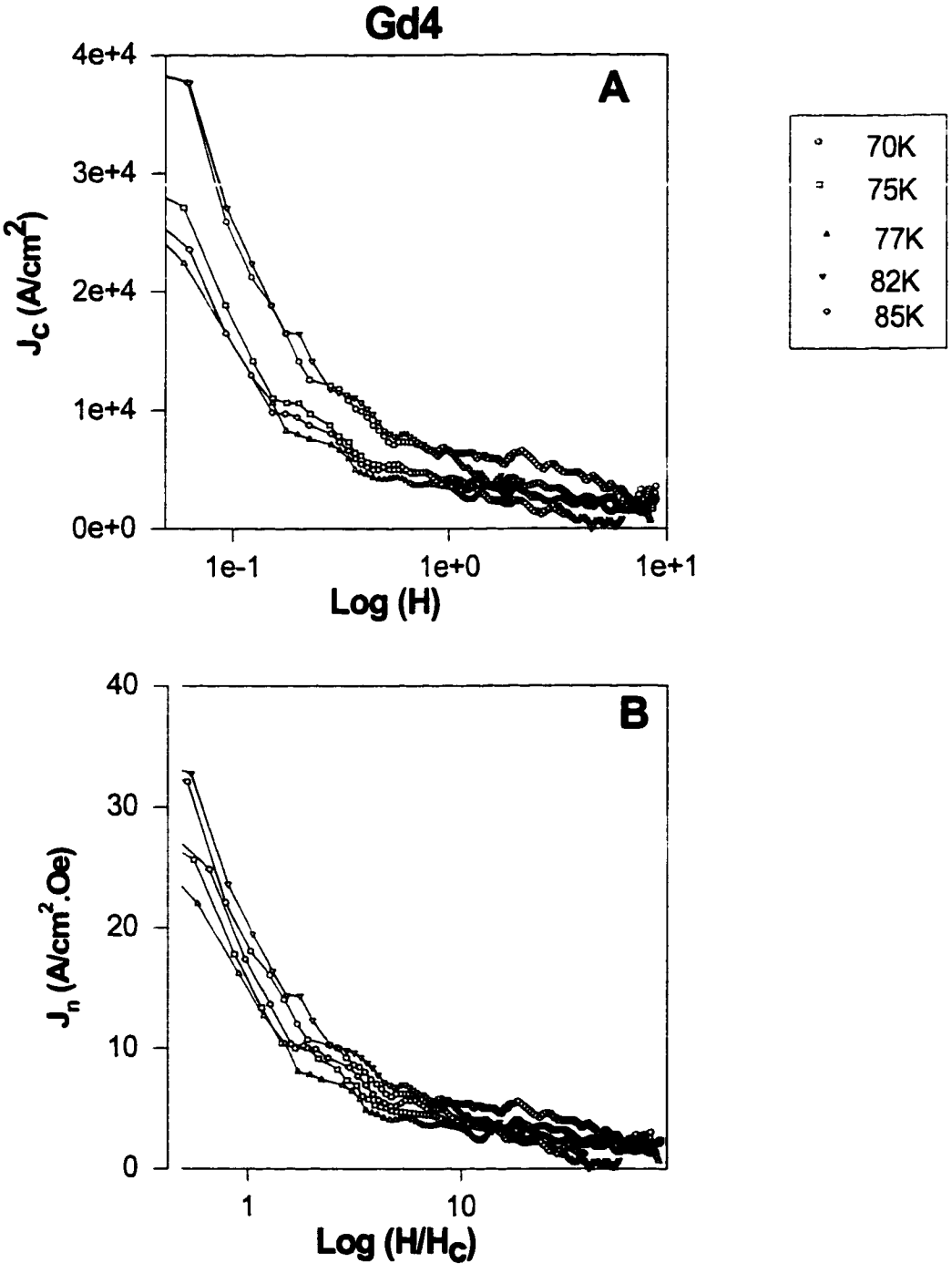

Figure 25: A) J_c vs Log(H) for Gd4 at various temperatures. B) Scaling of J_c using the critical thermodynamic field H_c.(The lines are guides for the eye)

A possible reason for this result is the peak effect in Gd-Y samples. Moreover, as we introduce more Gd into the sample, more imperfections and defects are present in the sample. This might give rise to additional pinning centers.

5.3 Pinning Force

We mentioned earlier that, in type II superconductors magnetic flux penetrates the material when the applied magnetic field exceeds H_{c1} (the lower critical field). Between H_{c1} and H_{c2} (the upper critical field), the superconductor is in a mixed state. The magnetic flux penetrates the SC in the form of flux lines each carrying a single flux quantum φ_0. Motion of the flux lines can be induced by the Lorentz force of an electric current or the thermal force of a temperature gradient [50].

For flux flow to occur the driving force should exceed the pinning force. The pinning force determines the critical current and the critical temperature gradient and causes irreversibilities in the magnetic behavior of the SC [50], [51]. The pinning force is given in terms of the Lorentz force:

$$PF = J_c \times H \tag{5.3}$$

Since the critical current increases by increasing the pinning force, it is important from an application point of view to increase the density of pinning centers.

The behavior of the pinning force for Gd1, Gd2, and Gd3 are shown in part A of Figures

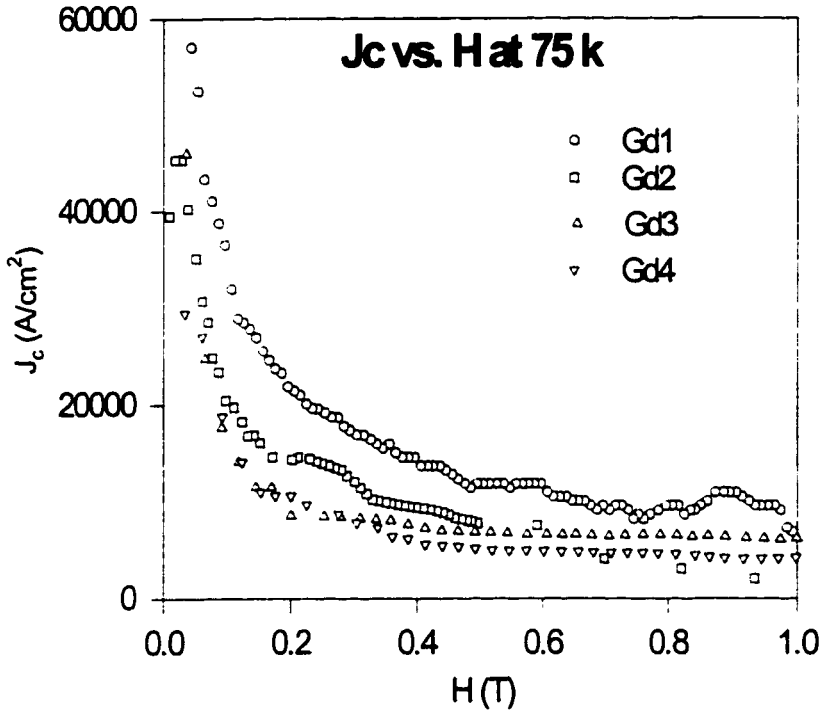

Figure 26: J_c vs H at 75 K for the four Gd doped samples.

27, 28, and 29, respectively. The general behavior of the pinning force curves is similar in the four Gd doped samples. The pinning force decreases as the temperature increases. Initially, the pinning force increases with applied magnetic field, reaching a maximum at a certain value of the applied field H^*. Above H^*, the PF decreases gradually, reaching zero when the width of the hysteresis loop vanishes. However, we have seen more than one maxima in the pinning force curves (see part A in Fig. 28).

This phenomena of having more than one peak in the pinning force curve has been observed for other materials such as the one shown in Fig. 30 for Nb-Ti alloy [51], [50] . Numerous experimental investigations were done to explain this phenomena. The main general conclusion that can be drawn from this observation is that there are more than one mechanism controlling the PF [51], [50].

5.4 Review of Scaling

If one compares the shape of the pinning force curves at different temperatures (Fig 27 for example), some similarities in the shape of the curves at various temperatures can be observed. This suggests that these curves can be normalized (scaled) so that they all may coincide at one curve.

Scaling is very important for two reasons. First, one can use the behavior of the scaled quantity (Jc, PF) to predict its behavior at any other temperature or field. Second, scaling gives useful information about the pinning mechanism and changes in the mechanism at extreme experimental conditions. For example, if the pinning force scales over a wide

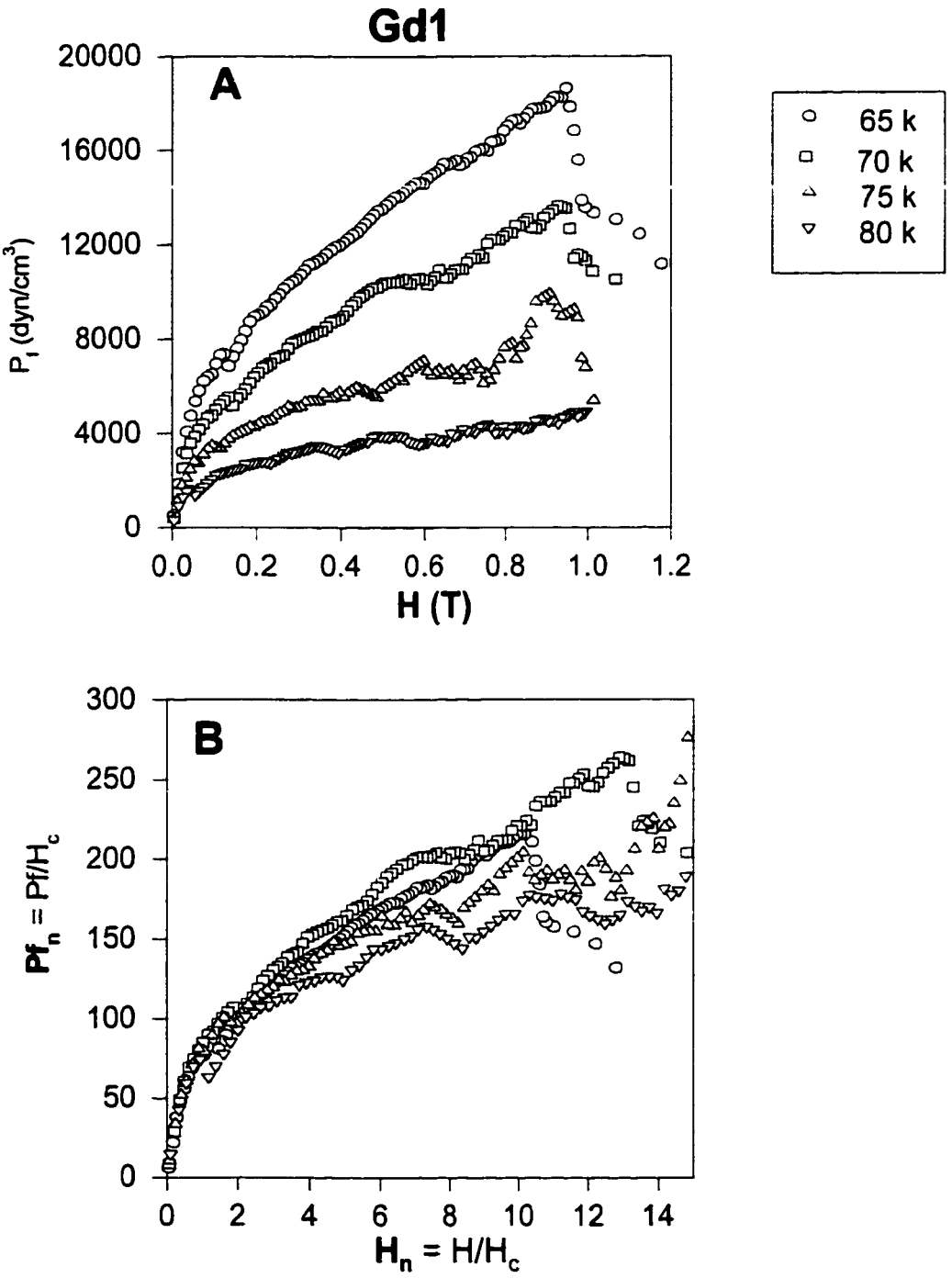

Figure 27: A) PF vs. H for Gd1 at various temperatures. B) Scaling of PF using thermodynamic critical field H_c.

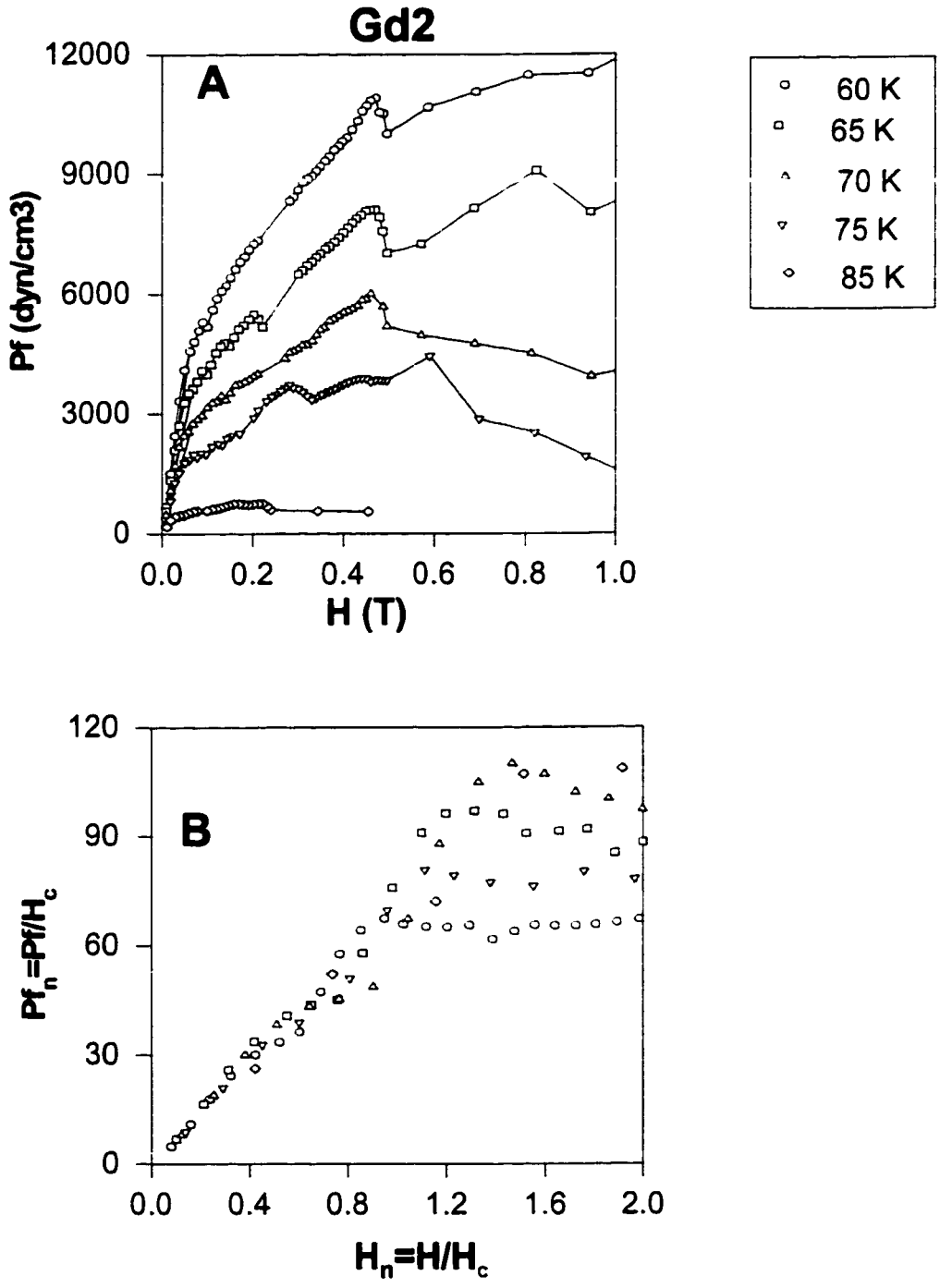

Figure 28: A) PF vs. H for Gd2 at various temperatures (The lines are guides for the eye). B) Scaling of PF using thermodynamic critical field H_c.

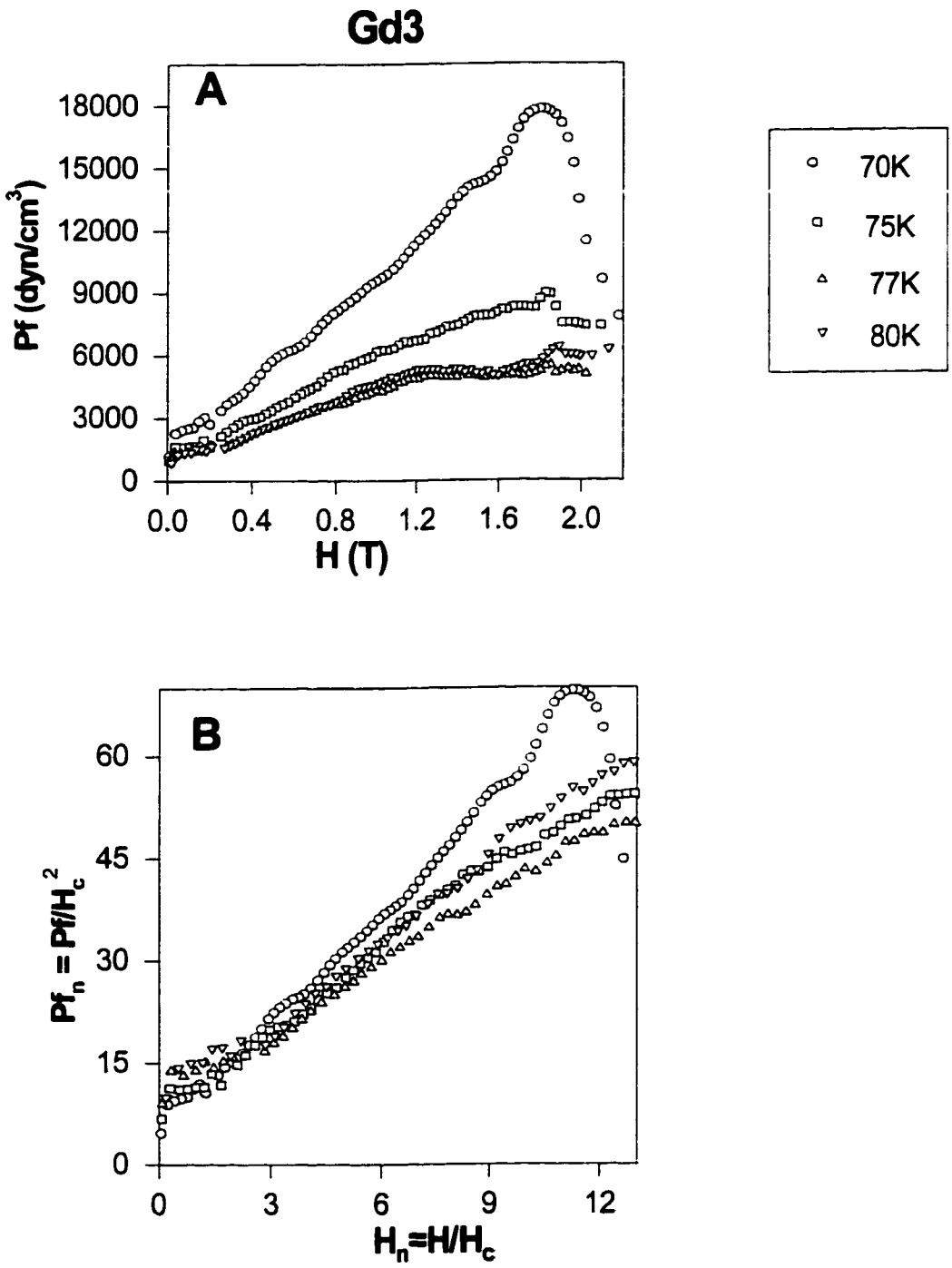

Figure 29: A) PF vs. H for Gd3 at various temperatures. B) Scaling of PF using thermodynamic critical field H_c.

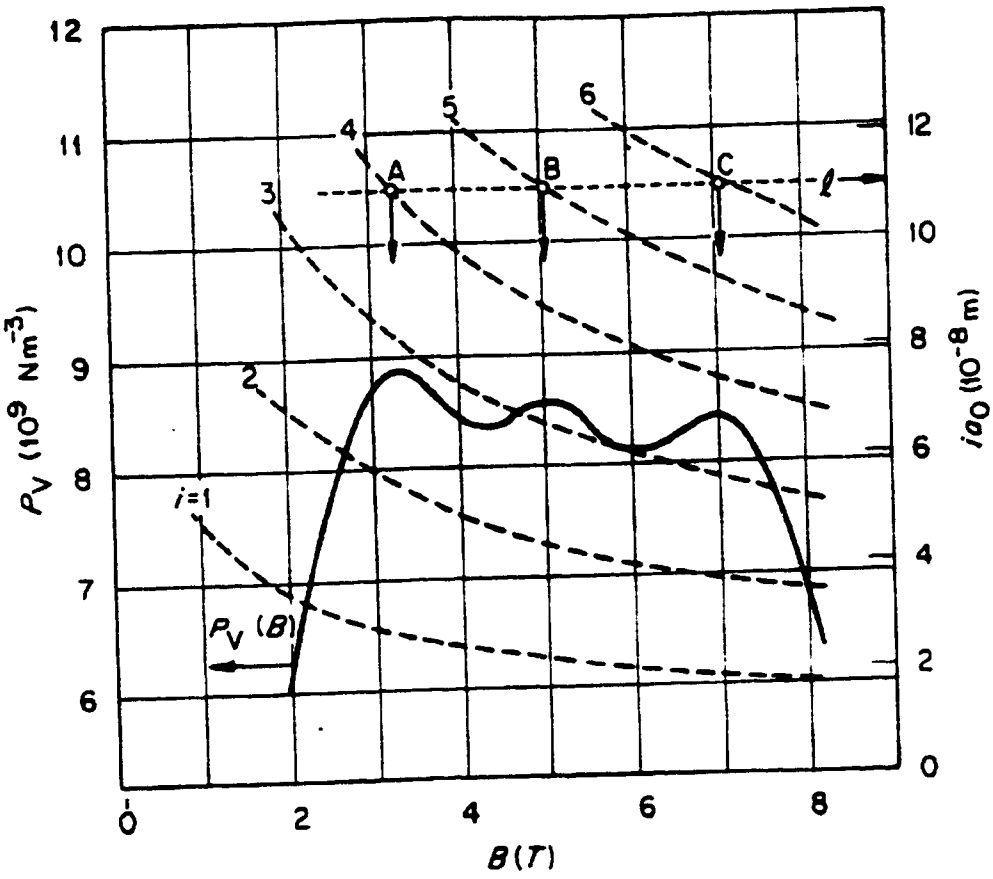

Figure 30: Pinning force vs. flux density for Nb-Ti alloy showing more than one peak.

range of temperatures ($\leq T_c$) or fields, then this would imply that no change in the pinning mechanism is expected within this range. One mechanism is responsible for pinning over the range of validity of scaling [51], [52], [53].

In the late sixties and early seventies, different scaling procedures have been introduced. Scaling of PF vs. H using PF_{max} and $(H_{c2})^{2.5}$ was first recognized by Fietz and Webb in 1969 for dilute Nb-based alloys. It is a good scaling parameter for a large variety of hard superconductors [51], [54]. Many others, like Kramer [54] and Juang et al [55] used these two parameters (i.e. H_{c2} and PF_{max}) to scale the pinning force. However, for high-T_c superconductors it is very difficult to measure H_{c2} from a practical point of view. To imagine the degree of difficulty of measuring H_{c2} for HTSC, it is enough to know that ,for example, H_{c2} = 160 T for $YBa_2Cu_3O_{7-\delta}$ [1].

Other scaling procedures have been applied for HTSC, such as PF_{max}, H_{irr}, and H^* [56] , [57] where H_{irr} is the magnetic field at which the pinning force vanishes, and H^* is the magnetic field at which PF reaches its maximum. E. H. Abdel-Hafidh used PF_{max} and H^* as scaling parameters [58]. While F. M. Enaya scaled using one parameter called H_p which is the threshold field or full penetration field above which PF approaches saturation [59].

Most of these scaling procedures use two scaling parameters (one for PF and one for H) except the last one by F. M. Enaya. Another observation is that all of the scaling parameters used are geometrical, i.e. all are based on geometrical similarity of the shape of PF vs. H curves at various temperatures. It should be pointed out here that very little effort has been devoted to scaling behavior of the critical current density.

In this study, the thermodynamic critical field H_c (that we calculated in chapter 4) will

be used to scale both the critical current density and the pinning force, i.e. a single scaling parameter for J_c and PF will be used. Moreover, this parameter is not based on geometrical similarity of the magnetization curves, it is a thermodynamical property of the sample.

In the following section, the scaling of J_c and PF for GdBCO system will be shown. In chapter 6, the same parameter will be used in scaling the stripe phase of $La_{1.45}Nd_{0.40}Sr_{0.15}CuO_4$ superconductor.

5.5 Scaling of the Critical Current Density and the Pinning Force

Several studies showed that the critical current density depends on the thermodynamic critical field H_c as it is related to the condensation energy [52].

In part (b) of Figures 22, 23, 24 and 25, we present the normalized critical current density (J_c/H_c) vs. changes in the normalized field (H/H_c). These figures show that Jn at different temperatures reasonably follows a universal curve when plotted against Hn. Although in conventional superconductors J_c is controlled by the defect structure not by thermodynamic variables [60], it seems that in high-T_c superconductors J_c is also controlled by thermodynamic properties, it showed good scaling behavior using the thermodynamic critical field H_c.

These results can be cast in another way of presentation, namely normalized pinning force vs. normalized field; we have

$$PF = J_c \times H \tag{5.4}$$

$$\frac{PF}{H_c^2} = \frac{J_c}{H_c}\,\frac{H}{H_c} \tag{5.5}$$

The results are shown in part B of Figures 27, 28, and 29.

The normalized pinning force shows relatively large scattering deviations from single universal behavior, especially at high fields. However, the max. in the normalized PF occurs almost at the same normalized field, i.e. independent of temperature.

The universal behavior of PF can be illustrated by presenting the variation of PF_{max} vs. H_c on a log-log graph. The results are shown in Fig 31.The figure shows that the shapes are almost constant for various samples. The slopes are n = 2.0, 2.6, 2.3 and 1.8 for Gd1, Gd2, Gd3 and Gd4, respectively. These slopes suggest that PF is proportional to H_c^n where $n \sim 2$, since the condensation energy is proportional to H_c^2. This means that if one divides PF by H_c^2, they will be able to get a universal curve within a certain range of validity as shown in part B of Figures 27, 28, and 29. In those figures, $Pfn = PF/H_c^2$ and $Hn = H/H_c$.

The range of validity of using H_c as a scaling parameter is limited to high temperatures and low applied magnetic fields. At low temperatures, reversible magnetization is not achieved and therefore H_c can not be calculated correctly. At high temperatures and magnetic fields, fluctuations and changes in pinning mechanism cause large deviations from

universal behavior. For these samples, H_c is a good scaling parameter if there is a sufficiently wide range of thermodynamic reversibility to allow calculating H_c with reasonable accuracy. In the case of high magnetic fields, multiple peaks in the pinning force become more evidence (see Fig. 30). This probably indicates that another mechanism controls the pinning at high magnetic fields. Hence, the scaling process is not valid at high magnetic fields.

To conclude this chapter, the thermodynamic critical field (H_c) is a good scaling parameter within a certain range of validity for the GdBCO system. The core energy of the vortex ($\sim H_c^2$) plays an important role in the pinning mechanism.

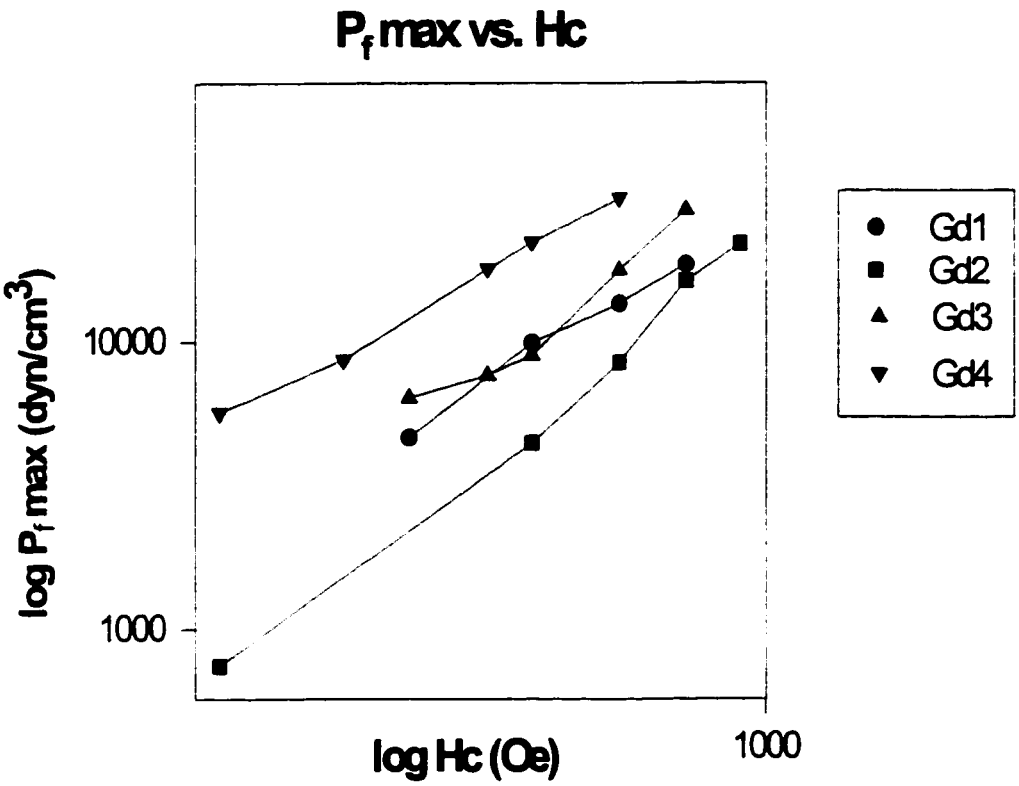

Figure 31: PF_{max} vs. H_c on Log-Log scale for the Gd doped four samples.

CHAPTER 6

Scaling in the Stripe Phase of $La_{1.45}Nd_{0.40}Sr_{0.15}CuO_4$ Superconductor

6.1 Introduction

In this chapter, we extend our investigation to the stripe phase of superconductivity, namely to the superconductivity in $La_{1.45}Nd_{0.40}Sr_{0.15}CuO_4$. The sample is a single crystal and has a paramagnetic contribution due to the presence of Nd. The procedures described in chapter 3 will be applied to subtract the paramagnetic contribution. Then, H_c will be evaluated along two different crystallographic directions (c-axis and ab-plane) using the free energy approach, since it is expected that H_c is independent of the direction of the applied magnetic field. Finally, H_c values will be used to scale both the critical current density (J_c) and the pinning force (PF) along c-axis and in ab-plane.

6.2 Stripe Phase Superconductors

HTSCs are layered materials where superconductivity is believed to be confined to the CuO_2 planes. The charge carriers are thought to be uniformly distributed throughout the CuO_2 layers. The behavior of the charge carriers in the CuO_2 layer seems to be very important in understanding the SC properties of HTSC materials [61]. However, in some superconducting materials, the situation is different. It has been found (using neutron scattering [62]) that the charge carriers are lined up in rows in the CuO_2 planes [63] sandwiching between them regions of copper atoms whose spins are aligned antiferromagnetically with nearest neighbors having opposite spins as shown in Fig. 32. This arrangement of charges and spins was first discovered in 1990 and confirmed by many experiments using X-ray absorption (XAS), high energy X-ray diffraction (XRD) and neutron scattering [64].

Fig. 32 (after [63]) shows a model of charge and spin stripes. Empty circles represent Cu ions with no net spin because of the loss of the unpaired electrons after doping. Black circles are holes and located in those rows of spinless ions. These rows of holes and charges with no spin separate regions of copper ions with spins aligned antiferromagnetically [63].

Fig. 33 (after [61]) shows a sketch of an ordered stripe phase. Big arrows represent charge carriers while small arrows represent spins. The period of spin is twice the period of charge carriers. The stripes are oriented parallel to [100] and [010] directions in successive planes of CuO_2 [65]. These stripes can be viewed as being 1-dimensional superconducting quantum wires, which means that superconductivity which is a macroscopic property is confined to stripes on a microscopic level.

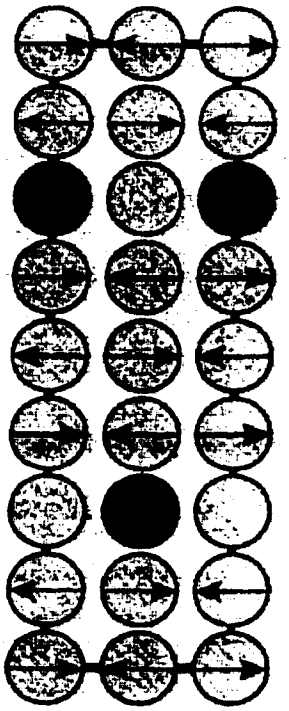

Figure 32: A model of charge and spin stripes. Empty circles are Cu ions with no net spin, black circles are holes, and arrows represent the spin.

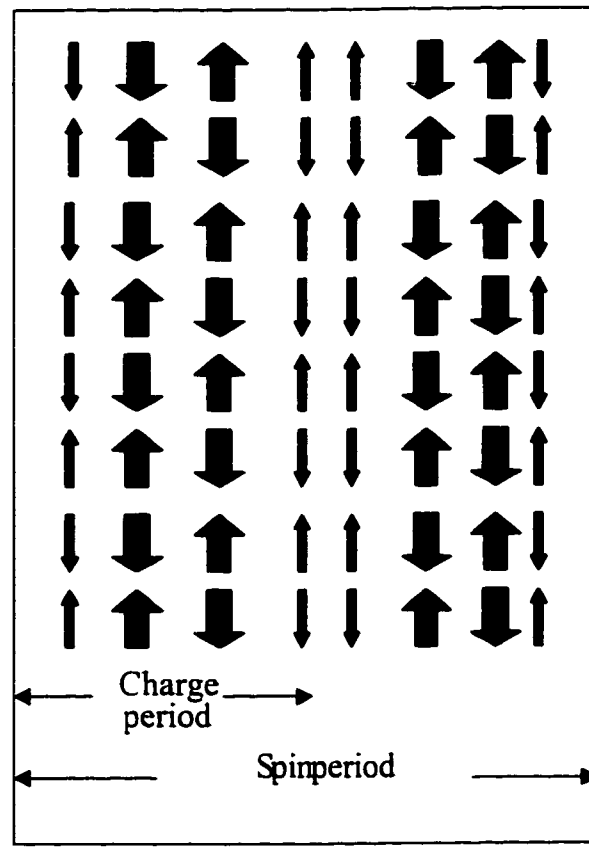

Figure 33: A sketch of an ordered stripe phase.

The parent HTSC sample is La_2CuO_4 with $T_c = 40$ K, when doped with certain amounts of Sr and Nd, it transforms to a stripe phase $La_{1.45}Nd_{0.40}Sr_{0.15}CuO_4$ superconductor with $T_c = 10.5$ K. These stripes formed after doping are static (do not fluctuate with time). Changes in the density of charge carriers may be responsible for the reduction of the transition temperature [61].

Recently, it has been proposed that the spin and charge stripes play a key role in HTSCs. There are increasing efforts to investigate the stripe behavior within many other HTSCs such as $YBa_2Cu_3O_7$. Those stripes are thought to be dynamic rather than static, and have therefore proved to be difficult to probe [61], [63], [64]. The subject of stripe phase is a fascinating one and is expected to improve our understanding of superconductivity and magnetism in HTSCs.

6.3 About the Sample

The sample used in this work is a single crystal with the following specifications:

mass = 140 mg

volume = 0.019805 cm^3

thickness = 1.5 mm

number of Nd^{3+} ions = 4.3×10^{21}

$T_c = 10.5$ K

This sample is a portion of the same sample used for neutron scattering by J. M. Tranquada et. al. [62]. The sample structure is tetragonal in which $a = b \neq c$ [65].

6.4 Magnetic Properties

In the stripe phase sample under study ($La_{1.45}Nd_{0.40}Sr_{0.15}CuO_4$), Nd is one of the rare earth elements with a spin of 9/2 and Lande factor g = 0.7273. The paramagnetic Nd-moments are aligned parallel to the c-axis. It is expected that a larger magnetization shall be observed when the applied magnetic field is parallel to the c-axis than when it is along the ab-plane. Fig. 34 shows two magnetization curves, one with the applied magnetic field parallel to the c-axis and the other when the applied magnetic field is along the ab-plane. About an order of magnitude difference between the two hysteresis loops is clearly seen in the figure. The magnetization in the c-axis direction is much larger because of the paramagnetic contribution (due to Nd^{3+} ions) to the magnetization.

This is a completely different situation relative to the GdBCO system discussed in the previous chapters. The GdBCO samples were polycrystals with the paramagnetic moments randomly oriented throughout the samples, so we had only one hysteresis loop for each sample at a given temperature. This is a system with two completely different hysteresis loops, one along the c-axis and the other along the ab-plane.

In order to subtract the paramagnetic contribution to the magnetization curve, the same technique described in chapter 3 for the Gd doped samples is applied. For a given applied magnetic field direction, the paramagnetic contribution at high fields is fitted using the extended Brillouin function, then we subtracted that contribution to get the superconducting contribution. Fig. 35 shows the superconducting magnetization with applied magnetic field parallel to the ab-plane and the c-axis at 8 K after subtracting the paramagnetic contribution

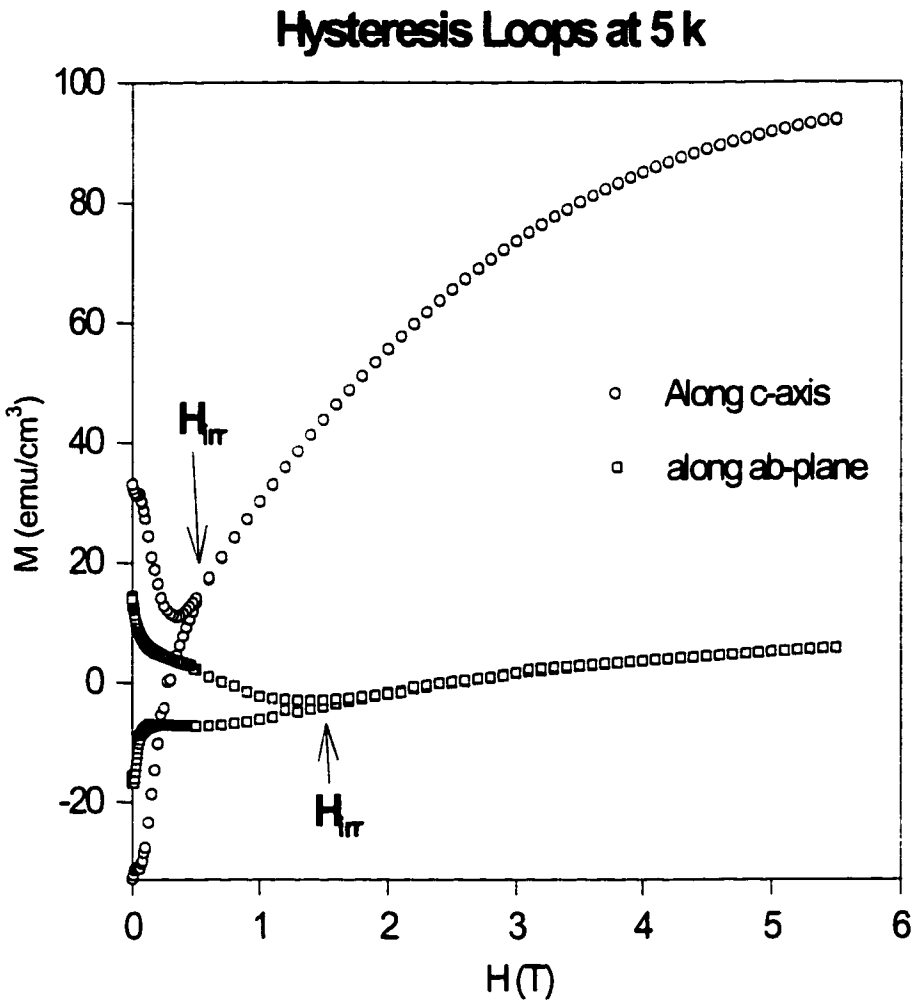

Figure 34: Comparison between hysteresis loops for applied fields parallel to the c-axis and along the ab-plane.

due to Nd^{3+} ions. Although the shape of the two curves are different, the area under the two curves is the same, indicating that the condensation energy is independent of the direction of the applied magnetic field. The general behavior of the superconducting magnetization shows a second minima at $H = 4800\ Oe$ for both directions of the applied magnetic field. This phenomena is not yet fully understood, but have been obsereved for many other high-T_c superconductors with high density of columnar defects [65].

6.5 Thermodynamic Properties

We applied the same method described in chapter 4 to calculate the free energy of the system. The thermodynamic critical field H_c is calculated at different temperatures ranging from 5.0 K to 10.5 K. Our stripe phase sample shows a wide range of reversibility in its hysteresis loops, so that H_c can be accurately calculated with confidence. Fig. 36 shows the irreversible field values deduced from the hysteresis loops (as shown in Fig. 34). The c-axis shows a wider range of reversible magnetization than the ab-plane. Therefore, we expect more accurate determination of H_c values for the c-axis than for the ab-plane.

The H_c values vs. T for applied fields in both directions (parallel to c-axis and along ab-plane) are shown in Fig. 37. We notice that H_c values are the same for both directions. This is an expected result since the free energy difference (condensation energy) is unique for the system at any given temperature whether we calculate it with fields applied parallel to the c-axis or along the ab-plane. However, we observe little difference between H_c values for both directions at low temperatures. The reason for this difference is that at low

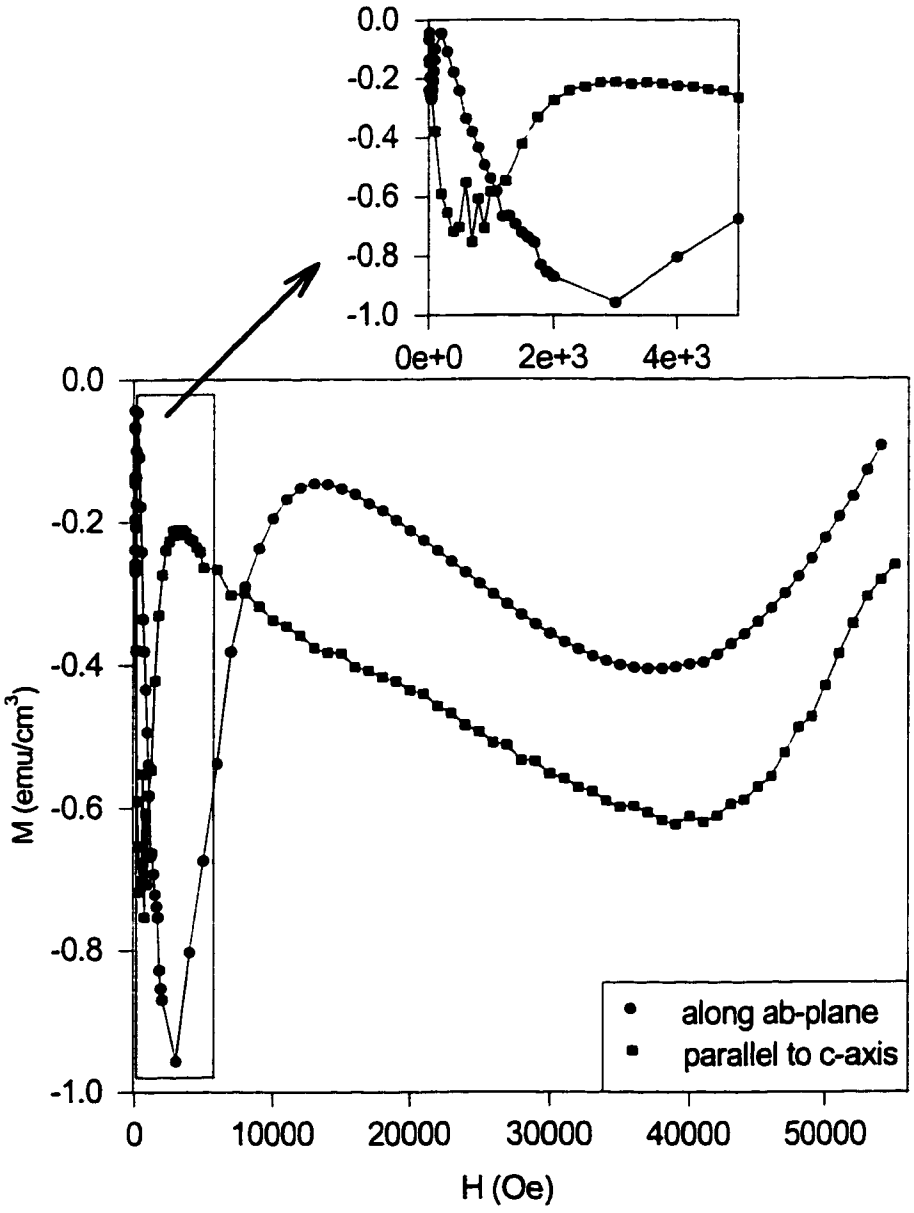

Figure 35: Superconducting magnetization of the stripe phase sample with the applied field along the ab-plane and parallel to the c-axis after subtracting the paramagnetic contribution due to Nd^{3+} ions from the total magnetization at 8 K (The lines are guides for the eye).

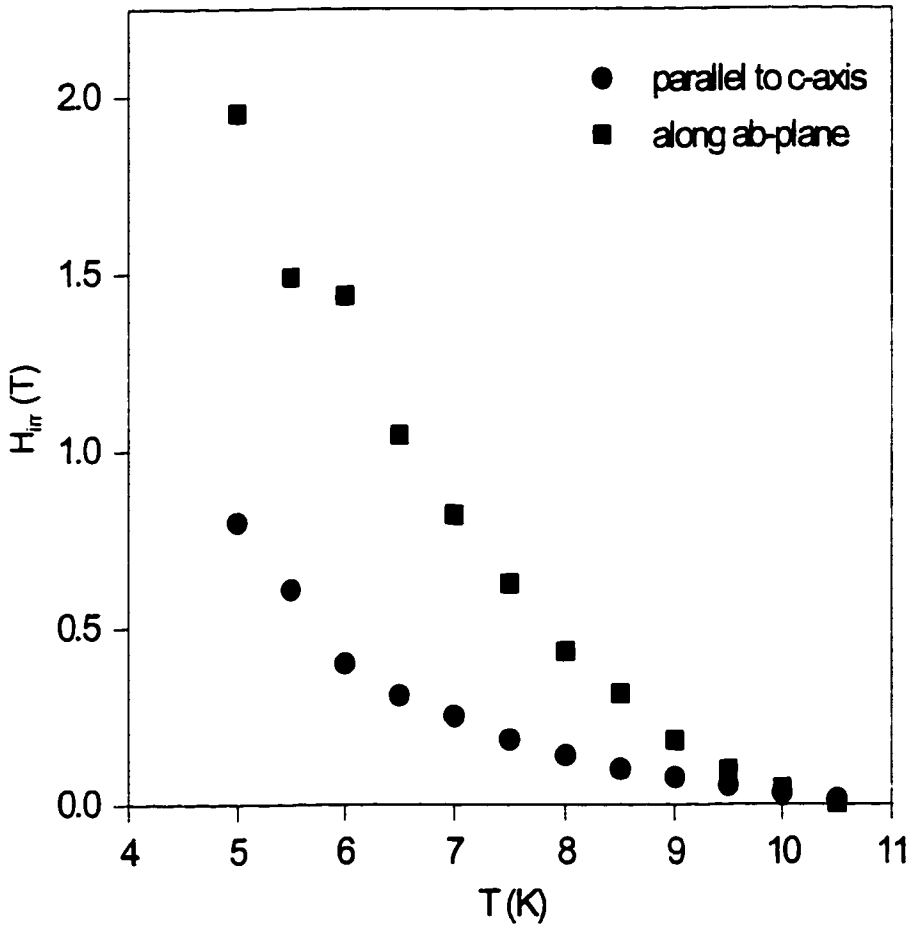

Figure 36: H_{irr} vs. T for both directions of the applied magnetic field (parallel to the c-axis and along the ab-plane).

temperatures we get closer to the ordering temperature ($\sim$ 3 K). So, we expect the extended Brillouin function not to be applicable at low temperatures, and as a result H_c values at low temperatures are not precise. Moreover, at low temperatures the reversible range of the magnetization curve (which is used to calculate H_c) gets narrower, hence the error in the calculated H_c increases.

We can compare our results of H_c with the values published in the literature by J. Ostenson et. al. [65]. They used a Curie-Weiss-like approach and the following relation to fit the magnetization data at high magnetic fields in order to subtract the paramagnetic contribution:

$$M_n = \frac{N\left[\sum_a \mu_a e^{\mu_a \cdot H/k(T-\theta)}\right]}{\left[\sum_a e^{\mu_a \cdot H/k(T-\theta)}\right]} \tag{6.1}$$

where $\mu = g\, m_j\, \mu_B$, m_j is the projection of the angular momentum along H, μ_B is the Bohr magneton, N is the number of Nd^{3+} ions and a is an index which runs over the m_j values. The values of H_c vs. T obtained using this method of fitting are shown in Fig. 38 noticing that the solid squares represent the first run, the open squares for the second run and the line shows H_c values for Nb for comparison. We believe that our method of fitting using the extended Brillouin function appears to be easier and gives better results for H_c.

As we have done with the GdBCO system in chapter 4, we calculated the deviation from the BCS coupling in the stripe phase sample under study. The deviation as shown in Fig. 39 indicates that the stripe phase sample under investigation has a weak coupling with a deviation of about 40 % from the BCS behavior. This means that the electron-phonon cou-

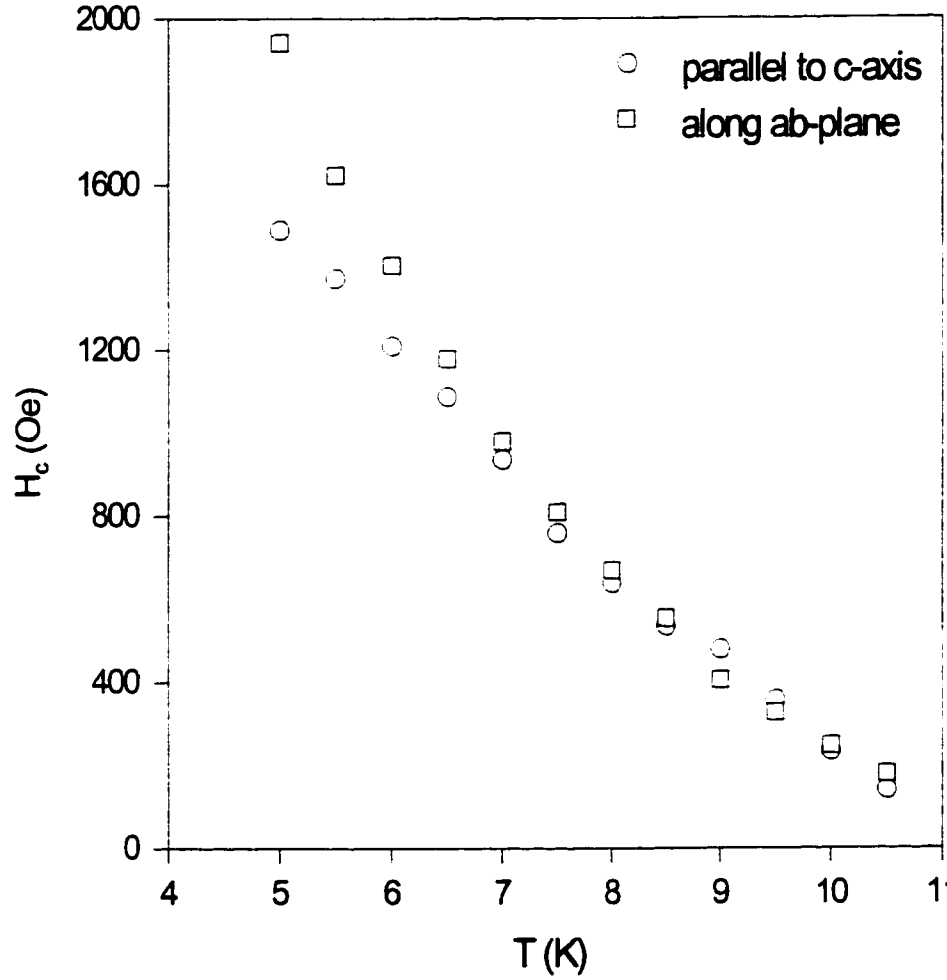

Figure 37: H_c vs. T for the stripe phase sample with applied magnetic field parallel to the c-axis and along the ab-plane.

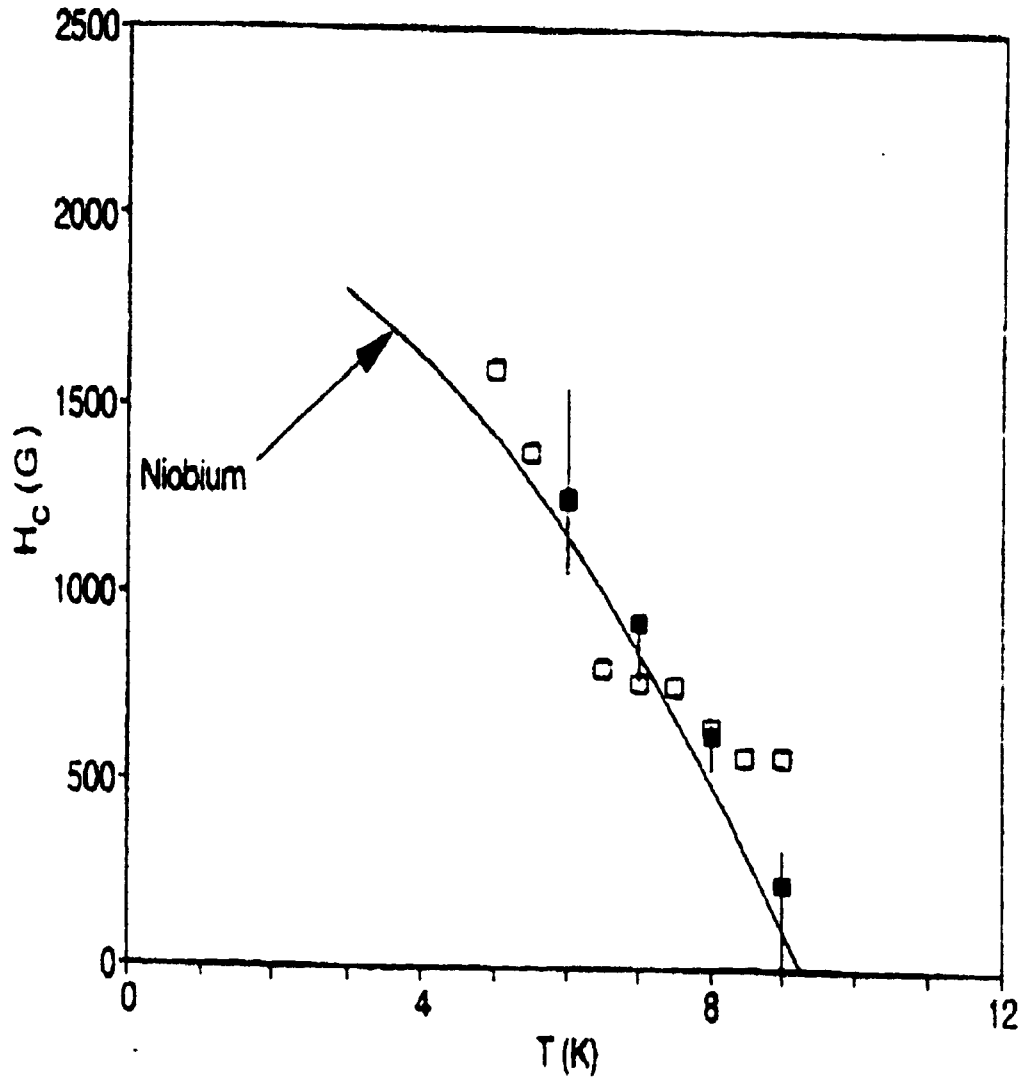

Figure 38: Comparison of H_c for $La_{1.45}Nd_{0.40}Sr_{0.15}CuO_4$ with Nb. Solid squares are the first run and the open squares are the second run. (These are the results of the work done by Ostenson et. al.)

pling is greatly reduced in the stripe phase SC by the presence of the charges and magnetic moments rearrangement (stripes). The increase in the effective mass of the whole stripes may play a role in this reduction.

6.6 Scaling of the Critical Current Density and the Pinning Force

The behavior of J_c with applied magnetic field parallel to the c-axis at different temperatures is shown in part A of Fig. 40. Part A of Fig. 41 shows the behavior of J_c with applied magnetic field along the ab-plane. The J_c values were calculated using Bean's model. The critical current has a high value at low fields, first it decreases gradually, then rapidly until it reaches zero at some higher field (H_{irr}) which varies with temperature.

We used the thermodynamic critical field (H_c) to scale the J_c values for both directions (parallel to the c-axis and along the ab-plane). The results of the scaling are shown in parts B of Figs. 40 and 41 as Jn=J/H_c and Hn=H/H_c. We can conclude that the scaled J_c values follow closely universal scaling with some scattering in the data. Again, J_c appears to be controlled by a thermodynamic variable (H_c), not only by the defect structure as it is the case in conventional superconductors [60].This also supports our observation in chapter 5.

The pinning force was calculated for this system using the relation PF = $J_c \times H$. The PF behavior as the magnetic field varies along the c-axis and along the ab-plane at different temperatures are shown in part A of Figs. 42 and 43, respectively. We notice that the pinning force (as given by Lorentz force) starts with zero value at zero magnetic field, reaches a maximum, then it goes to zero at a higher magnetic field. The maximum in PF changes

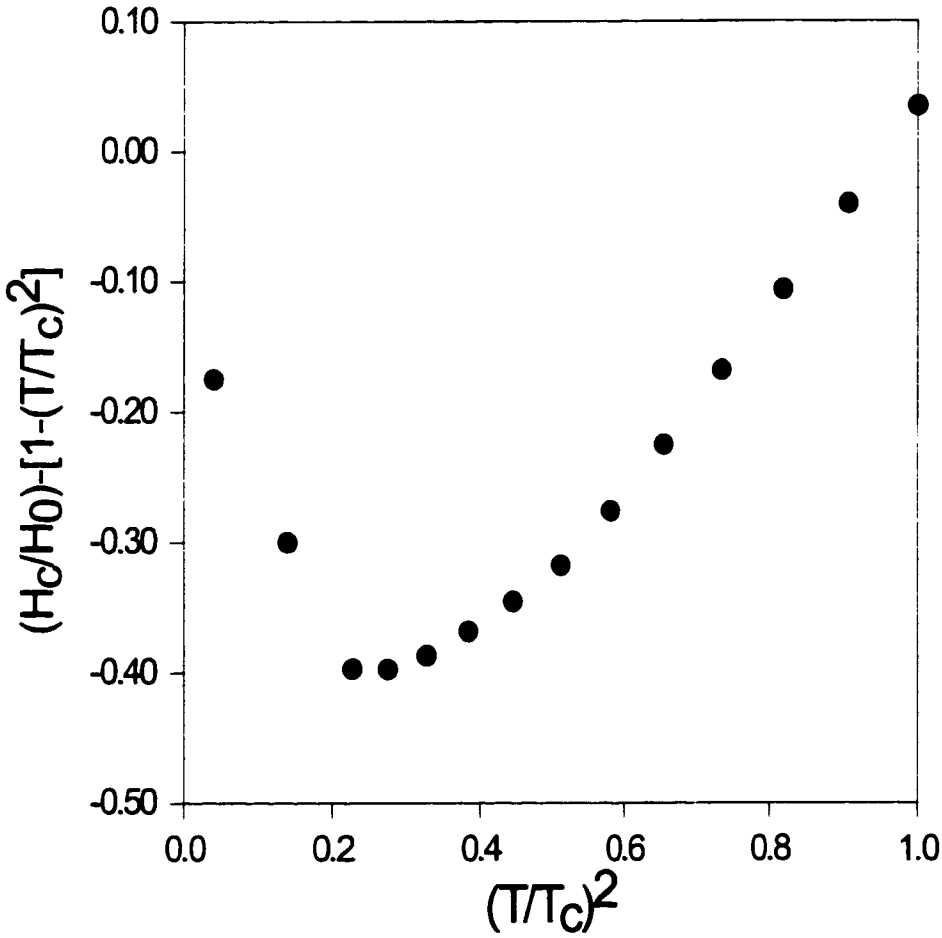

Figure 39: The deviation function of the thermodynamic critical field vs. $(T/T_c)^2$ for the stripe phase sample.

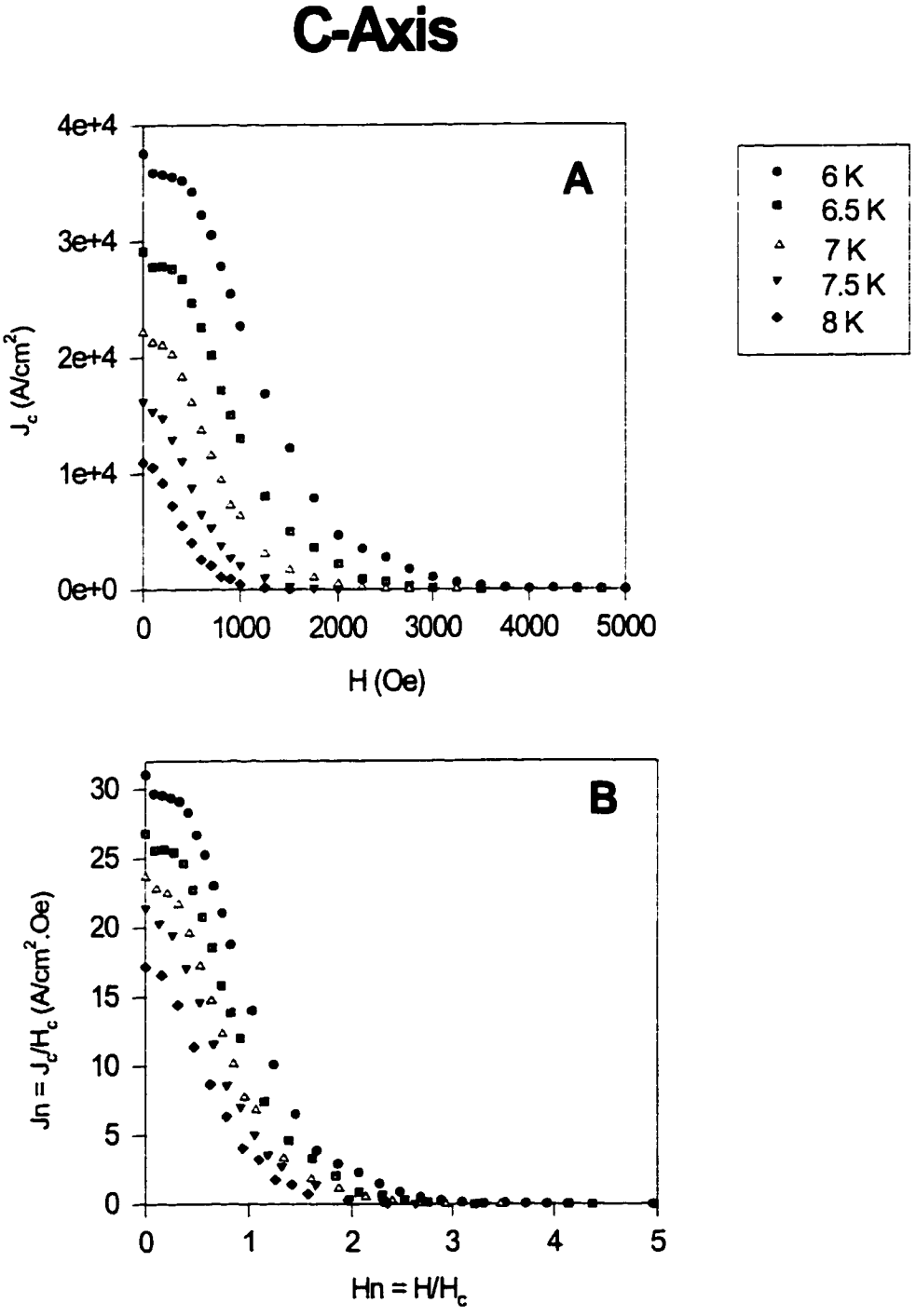

Figure 40: A) Jc vs. H parallel to the c-axis. B) Jn vs Hn.

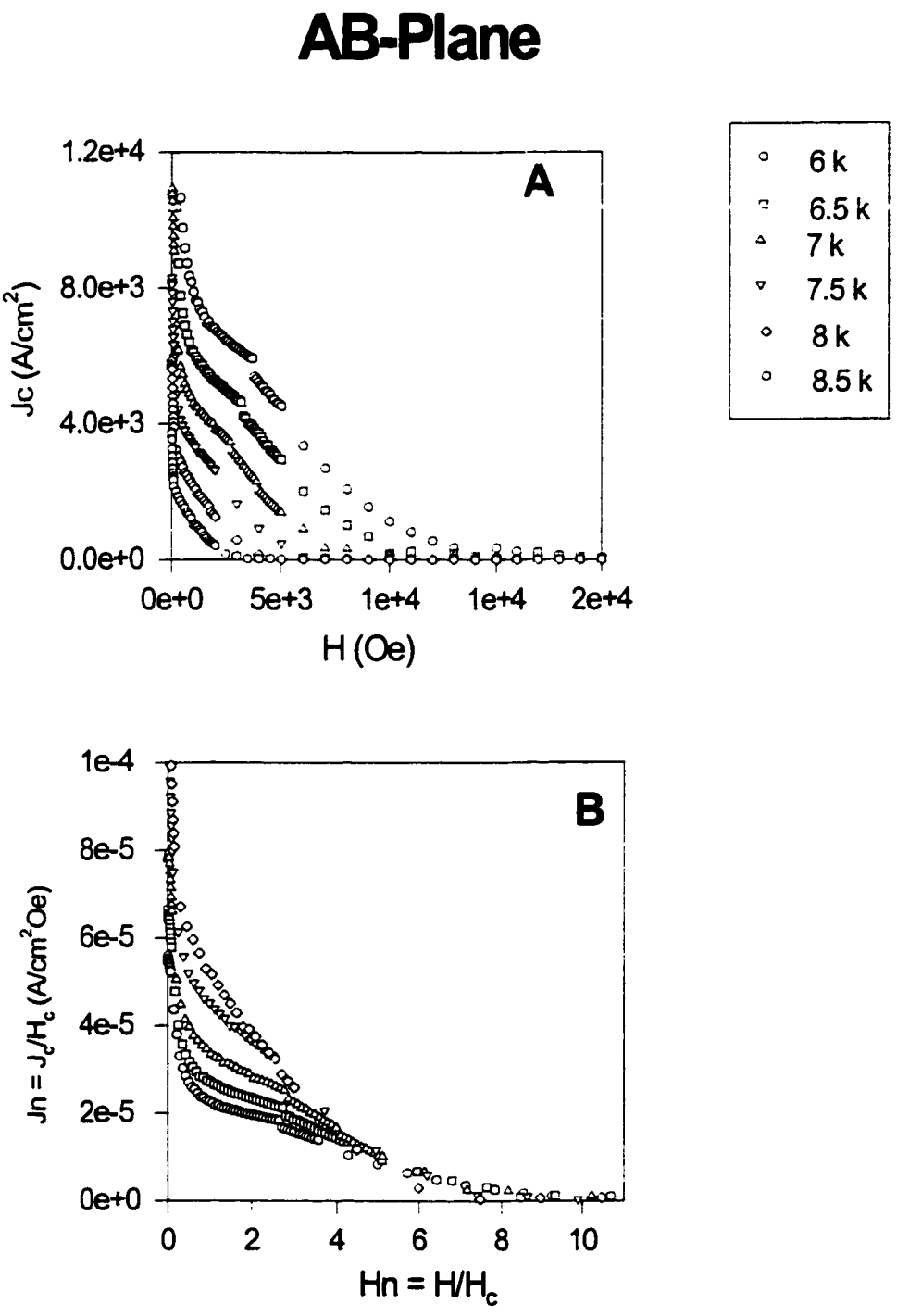

Figure 41: A) Jc vs. H along ab-plane. B) Jn vs. Hn.

with temperature, moreover, the field at which the PF is maximum and where it becomes zero decreases with increasing temperature.

We used the thermodynamic critical field values to scale the PF values for both directions (parallel to the c-axis and along the ab-plane). The results of scaling are shown in parts B of Figs. 42 and 43. We notice that the scaled PFn vs Hn curves follow (to some extent) a universal behavior.

It is interesting to see that H_c can be used to scale both J_c and PF for both directions, namely the c-axis and the ab-plane. This implies that H_c and hence the free energy plays an important factor contributing to the strength of flux pinning in this material [52]. The maxima of PFn occurs at Hn $\approx$ 0.8 for the c-axis and at Hn $\approx$ 3.5 for the ab-plane. This indicates that the pinning is stronger along ab-plane than in c-axis (PFn^{max} (ab) > PFn^{max} (c-axis)), i.e. the pinning is stronger in the direction of stripes. Thus, we conclude that the presence of stripes may provide new pinning centers.

To see the dependence of the PF on H_c, we plotted PF_{max} vs. H_c for both directions (the c-axis and the ab-plane) on Log-Log scale as in Fig. 44. The slope of both lines is about 3.7. This indicates that the PF depends roughly on $H_c^{3.7}$. This might explain why we did not get exact scaling of PF when we divided by H_c^2. The slope of PF_{max} vs. H_c for the Gd system was around 2 (as mentioned in chapter 5), while the slope for $Lu_{0.96}Gd_{0.04}Ni_2B_2C$ is found to be equal to 2 [52], indicating that The PF is proportional to H_c^2 for both of these systems. The higher exponent value for the stripe ($\sim$ 3.7) indicates that the thermodynamic field H_c may not be the only factor affecting the pinning in these materials.

In conclusion, we were able to calculate H_c for the stripe phase SC with applied mag-

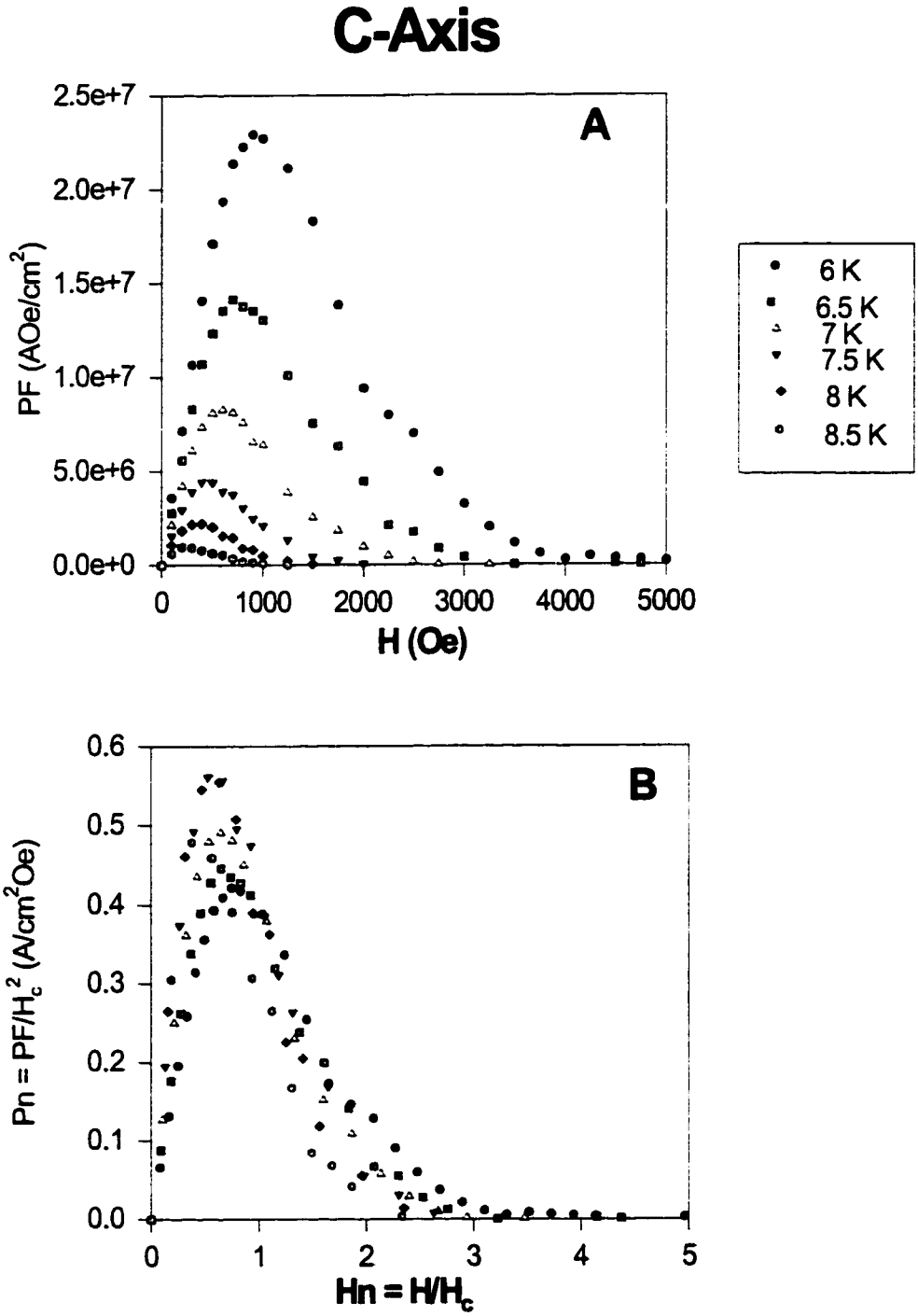

Figure 42: A) PF vs. H parallel to c-axis. B) PFn vs. Hn.

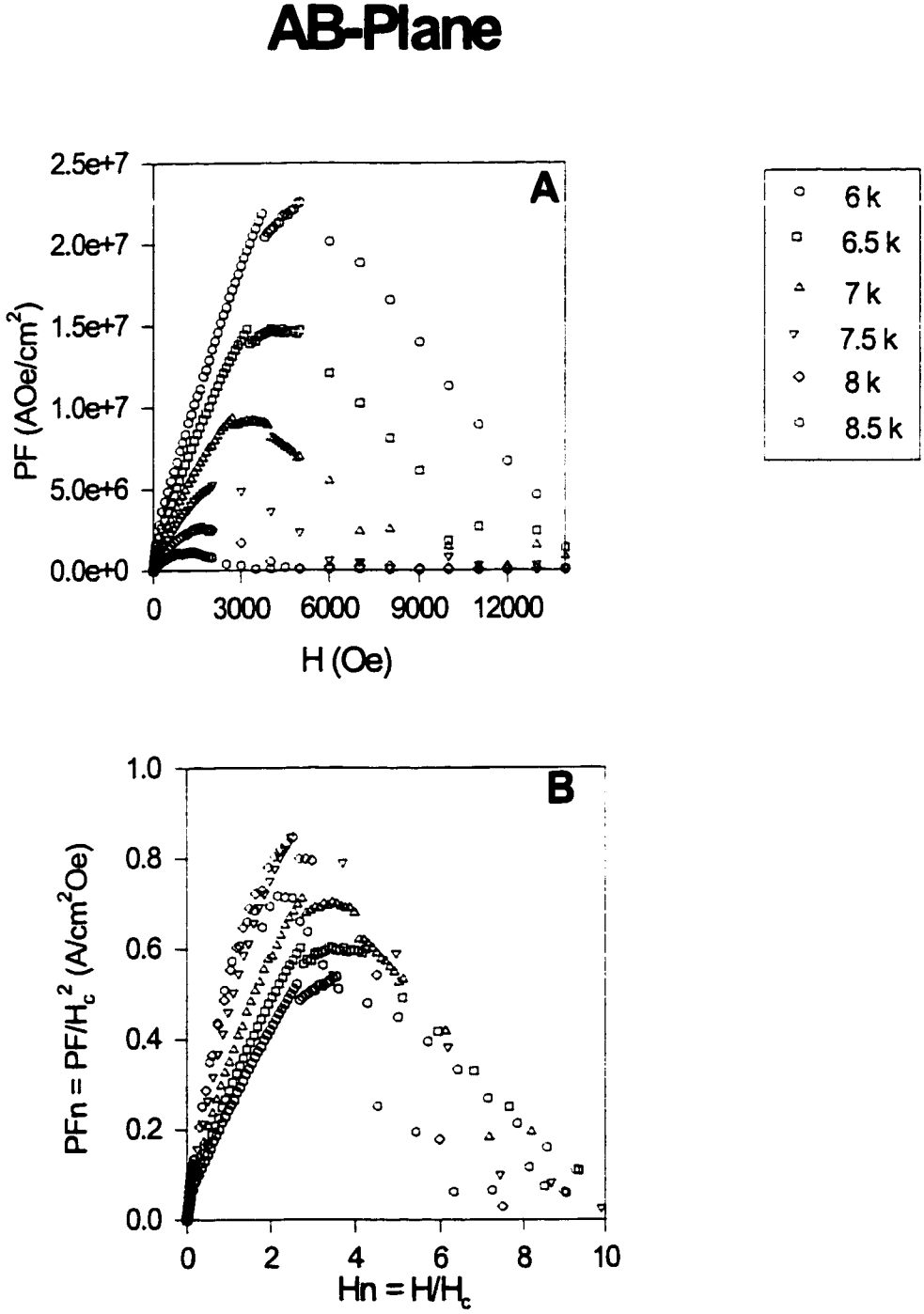

Figure 43: A) PF vs. H along the ab-plane. B) PFn vs. Hn.

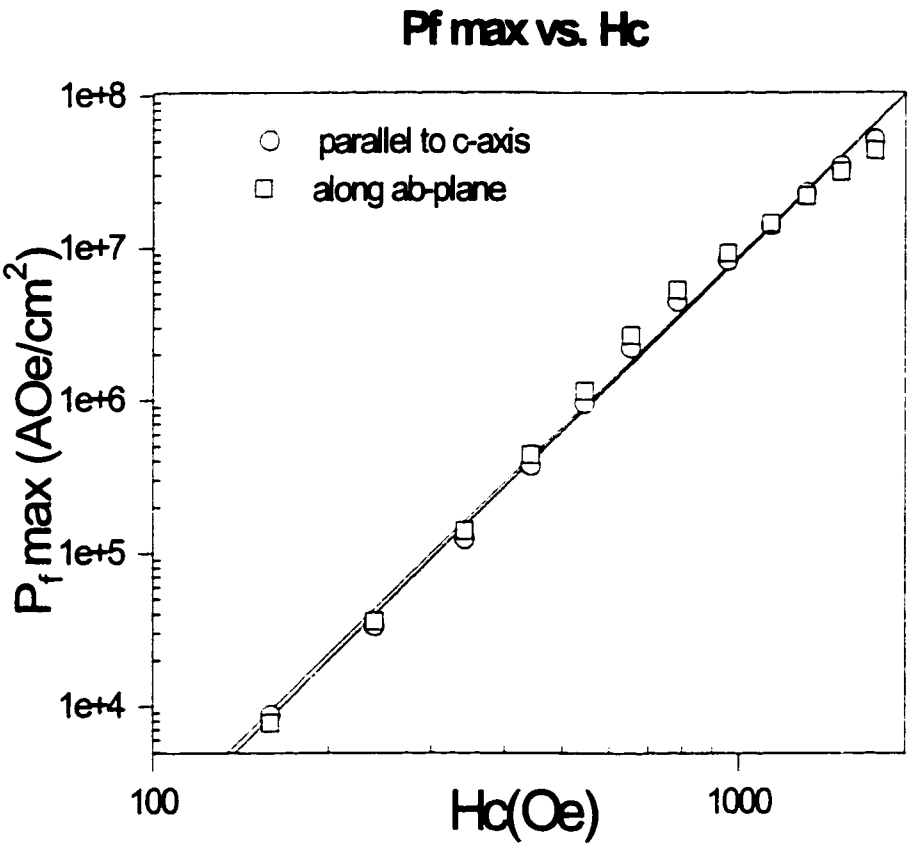

Figure 44: PFmax vs. H_c on Log-Log scale for both directions of the applied field parallel to x-axis and along ab-plane. The solid lines are linear fits. The slope of both lines is $\approx$ 3.7.

netic fields along two different directions. It was found that H_c is the same for both directions (as expected). We used these H_c values as a single scaling parameter to scale both J_c and PF in both directions.

CHAPTER 7

Conclusion

In this thesis, scaling of the critical current density and the pinning forces with the thermodynamic critical field in various high-T_c superconductors, namely $Y_{1-x}Gd_xBa_2Cu_3O_{7-\delta}$ and $La_{1.45}Nd_{0.40}Sr_{0.15}CuO_4$ were investigated.

Prior to calculating the thermodynamic critical field (H_c), the paramagnetic contribution was subtracted from the total magnetization by fitting the magnetization at high fields using the extended Brillouin function. Then, using the thermodynamic argument stating that the area under the superconducting reversible magnetization curve is proportional to H_c^2, H_c was calculated for the four Gd doped samples at different temperatures.

The critical current density (J_c) has been calculated from the hysteresis loops using Bean's model. The J_c's were found to have high values at low fields then drops sharply, then it follows a slow and gradual decrease as field increases. In normalized (scaled) representation, H_c was used to scale J_c and the applied field, the variations in $J_n=J_c/H_c$ vs. $H_n=H/H_c$ were found to follow a universal behavior. To the best of our knowledge, this is the first time that such scaling procedure has been applied to high-T_c superconductors. This is also considered to be one of the few efforts devoted to scale J_c. Most of the scaling studies

concentrate on the pinning force rather than J_c. Although in conventional superconductors J_c is controlled by the defect structure not by thermodynamic variables, it seems that in high-T_c superconductors J_c is also controlled by thermodynamic properties since it showed good scaling behavior using the thermodynamic critical field H_c.

The pinning force (PF) was calculated for these samples at various temperatures. The same scaling parameter H_c has been used to scale PF. The behavior of the scaled PF showed a universal behavior indicating that PF is mainly controlled by the condensation energy or simply the vortex core energy $\sim H_c^2$. The new thing to add here is that H_c is calculated from thermodynamics not from the geometry of the curve to be scaled (as it is the case in most of other scaling methods). It is a single scaling parameter for both J_c and PF curves.

At the end of this work, the previous procedures were applied to another superconducting sample which has anisotropic hysteresis behavior. The sample is a single crystal known as the stripe phase superconductor $La_{1.45}Nd_{0.40}Sr_{0.15}CuO_4$. The paramagnetic contribution due to Nd^{3+} ions are aligned along the c-axis, so that the magnetization along the c-axis is much higher than that along ab-plane. Although the irreversibility fields have different values at a given temperature, the area under the reversible superconducting magnetization along both directions was evaluated. The H_c values along both directions were found to be the same indicating that the condensation energy for the system is unique whether the applied field is parallel to c-axis or along ab-plane. In other words, H_c is not anisotropic.

Despite the fact that J_c and PF values in the ab-plane are much higher than the corresponding values along the c-axis, the normalized values of J_c and PF followed similar scaling behavior. The maxima of the normalized pinning force (PF_n^{max}) in the ab-plane is

about 5-times larger than that in the c-axis. Since the stripes lie in the ab-plane, one can conclude that they provide new pinning centers.

Further research on other HTSCs with paramagnetic moments seems promising. It is suggested that this approach of scaling be extended to other systems, such as single crystals of $GdBa_2Cu_3O_7$. One can look also at the effect of annealing, oxygen content, other magnetic and non-magnetic impurities such as Zn, ...etc. on the H_c values.

REFERENCES

1. R. A. Serway. *Physics for Scientists and Engineers*. Saunders College, 1990.

2. A. C. Rose-Innes and E. H. Rhoderick. *Introduction to Superconductivity*. Pergamon Press, 1978.

3. G. Vidali. *Superconductivity: the Next Revolution*. Cambridge University Press, 1993.

4. G. Burns. *High-Temperature Superconductivity*. Academic press, 1992.

5. F. J. Owens and C. P. Poole. *The New Superconductors*. Plenum Press, 1996.

6. T. H. Geballe. *Science*, 259:1550, 1993.

7. M B Maple. *J. of Mag. and Mag. Materials*, 177-181:18–30, 1998.

8. H. Theuss and H. Kronmuller. *Phys. C*, 242:155–63, 1995.

9. A Bourdillon N X Tan Bourdillon. *High Temp. Superconductors: Processing and Science*. Academic Press, 1994.

10. C Schneider Y Kuo and M Skove. *Phys. Rev. B*, 56(10):6201–6, 1997-II.

11. H. Theuss and H. Kronmuller. *Phys. C*, 177:253–61, 1991.

12. A. Pramana. Master's thesis, KFUPM, Dec. 1995.

13. Francis S Galasso. *Perovskites and High Tc Superconductors*. Gordon and Breach Science Publishers, 1990.

14. B. Batlog. *Phys. Today*, pages 44–50, June 1991.

15. M. Senoussi. Review of the critical current densities and magnetic irreversibility in high-tc superconductors. *J. de Physique 3, France*, 1992.

16. J. Borin and O. Baffa. *Am. J. Phys.*, 66(5):449–52, 1998.

17. E. Slowinski W. Masterton and C. Stanitski. *Chemical Principles*. Holt-Saunders Int'l Editions, 1985.

18. *Encyclopedia of Materials Science and Engineering*. Pergamon Press, 1986.

19. C. Kittel. *Introduction to Solid State Physics*. John Wiley and Sons, 1986.

20. N. W. Ashcroft and N. D. Mermin. *Solid State Physics*. Holt-Saunders Int'l Editions, 1976.

21. D. K. Finnemore. *A Child's Guide to BCS*. Nova Science Publishers, 1992.

22. E A Lynton. *Superconductivity*. Methuen Co Ltd., 1969.

23. Jeffrey W Lynn. *High Temp. Superconductivity*. Springger-Verlag, 1990.

24. B. Raveau. *Phys. Today*, pages 53–8, Oct. 1992.

25. A Mekki. PhD thesis, Warwich University, UK., 1997.

26. J. Tarascon and W. McKinnon. *Phys. Rev. B*, 36(1):226–34, 1987.

27. David J. Griffiths. *Introduction to Electrodynamics*. Printice Hall, 1989.

28. S. T. Sekula J. R. Thompson and D. K. Christen. *Phys. Rev. B*, 36(1):718–21, 1987.

29. H Bornemann C. Meyer and H. Schmidt. *J. Phys. F*, 17:345–51, 1987.

30. Beongki Cho. PhD thesis, Iowa State University, 1995.

31. L. Ji M. Qin and Jin. *Phys. Rev. B*, 50(6):4086–91, 1994.

32. A. Al-Sharif. *CATP First Symposium on Magnetics*, pages 131–40, 1993.

33. P. C. Jana and R. C. Bhuniya. *Solid State Comm.*, 87(8):731–734, 1993.

34. M. Mchenry M. Foldeaki and R. O'Handley. *Phys. C*, 161:403–11, 1989.

35. A. Gavrin G. Xiao, F. Streitz and C. Chien. *Solid State Comm.*, 63(9):817–20, 1987.

36. G J Baldha K M Pansuria, D G Kuberkar and R G Kulkarni. *SC Sci. Technol.*, 12:579–86, 1999.

37. I Felner and I Nowik. *SC Sci. Tech.*, 8:121–142, 1995.

38. V. Daniel Hunt. *Superconductivity Sourcebook*. John Wiley Sons, 1989.

39. T. Stromberg and C. Swenson. *Phys. Rev. Lett.*, 9(9):370–4, 1962.

40. P. S. Swartz. *Phys. Rev. Lett.*, 9(11):448–51, 1962.

41. Junho Gohing and D K Finnemore. *Phys. Rev. B*, 46(1):398, 1992.

42. C Dusek H Michor, T Holubar and G Hilscher. *Phys. Rev. B*, 52(22):16165, 1995.

43. P. Rogl H. Michor, R. Krendelsberger and H. W. Zandbergen. *Phys. Rev. B*, 54(13):9408, 1996.

44. D. M. Ginsburg. *Phys. Properties of High Temp. SC.* World Scientific, 1989.

45. M. C. Munson. *Inst. Measur. soc. Newsletter*, pages 6–16, Winter 1995.

46. R. P. Bean. *Rev. Mod. Phys.*, 36:31, 1964.

47. M. Tinkham. *Introduction to Superconductivity.* McGraw-Hill Inc, 1975.

48. Z. Vladimir. *Fundamentals of Superconductivity.* Plenum Press, 1990.

49. T Akune Akitoshi Matsuda and N. Sakamoto. *Advances in superconductivity X, Proceedings of the 10th Intl. symp. on S.C.- Japan*, pages 505–8, 1997.

50. R. P. Huebener. *Magnetic Flux Structures in Superconductors.* Springer-Verlag, 1979.

51. H. Ullmair. *Irreversible Properties of Type II Superconductors.* Springer-Verlag, 1975.

52. Kh. A. Ziq P. Canfield, J. Ostenson and D. Finnemore. *Phys. Rev. B*, pages 3603–7, Aug. 1999.

53. G Meijer J. Karpinski and H Schwer. *Supercond. Sci. Technol.*, 12:R153–R181, 1999.

54. E. J. Kramer. *J. Appl. Phys.*, 44(3):1360–70, 1973.

55. J. Juang. *Phys. Rev. B*, 46(2):1118, 1992.

56. J. Chang. *Phys. Rev. B*, 48:13911, 1993.

57. C. D. Wei. *Phys. C*, 195:286, 1992.

58. E. H. Abdel-Hafidh. Master's thesis, KFUPM, June 1996.

59. F. M. Enaya. Master's thesis, KFUPM, Oct 1998.

60. K. S. Athreya and S. C. Sanders. *Phys. Rev. B*, 41(1):264–66, 1990.

61. J. Tranquada. *Physics World*, pages 19–20, Nov. 1999.

62. J Axe Y Nakamura J. M. Tranquada, B Sternlleb and S Uchida. *Nature*, 375:561–3, 1995.

63. B. G. Levi. *Physics Today*, pages 19–22, June 1998.

64. A. Bianconi. *Phys. C*, 296:269–80, 1998.

65. M Breiwisch D Finnemore N Ichikawa J. E. Ostenson, S Bud'ko and S Uchida. *Phys. Rev. B*, 56(5):2820–23, 1997.

Appendix A

The Fortran Program Used to Fit the Magnetization to the Extended Brillioun Function

```
C###################### MGFT-MH FORTRAN ###############
C FITTING OF EXPERIMENTAL M (EMU/cm3) VS H (Tesla)
C INCLUDES ASSUMED UNCERTAINTIES AT 5%
C SET FOR UNDEFINED NBER OF DATA SETS
C DETERMINATION OF( Theta in the Extended Brillioune Function )
C USED FOR: YBaCuO
C DATA SETS: Gd1-4.dat,....
C=============================================
C CHARACTER*1 TITLE(10)
REAL H, Mag, VOL
COMMON/A/ X(100),Y(100),SIGMAY(100),YFIT(100)
COMMON/B/ A(5),DELTAA(5),SIGMAA(5)
COMMON/C/ DX
COMMON/D/ TEMP
COMMON/BBB/NTERMS,NPTS,MODE
C=============================================
NTERMS = 1
MODE = 1
C NBER OF DATA SETS: NDMAX, PLOTTING STEP: DX
NDMAX = 1
```

```
      DX = 100.
C-----------------------------------------------------------
C BASE REF NUMBER OF DATA FILES
C IND = 10
C-----------------------------------------------------------
C PER DATA SET ----------
      DO 10 ND = 1,NDMAX
C SET UP SEARCH PARAMETERS
      A(1) = 0.1
      DELTAA(1) = A(1) * 0.05
C IND = IND + 1
C READ IN DATA ------
C READ HEADLINES, DATA SET PARAMETERSS
C READ(IND,23) (TITLE(II),II=1,10)
C 23 FORMAT(10A1)
C READ(IND,*) PERC,MASS,TEMP
      VOL = 1
C POW = 10.**LEXP
C TEMP = TEMP
C WRITE(9,25) (TITLE(II),II=1,10),MASS,TEMP
C 25 FORMAT(1X,5X,10A1,' ==== ',' MASS = ',F6.4,' (G)',3X,
C * 'TEMP = ',F5.1,' (K)',/)
```

```
N = 0
C
C READ MAG VS FIELD DATA
C
open(1,file='m.dat',status='unknown')
28 READ(1,*,END=29) H,Mag
N = N + 1
X(N) = H
Y(N) = Mag
GOTO 28
29 CONTINUE
C
NPTS = N
C-----------------------------------------
C TRANSFORMING Y (MAG IN EMU) INTO Y (MAG IN EMU/cm3)
DO 30 N=1,NPTS
Y(N) = Y(N) / VOL
SIGMAY(N) = Y(N) * 0.05
30 CONTINUE
C-----------------------------------------
CALL GRIDLS (CHISQR)
C-----------------------------------------
```

```
C OUTPUT

WRITE (2,41)

41 FORMAT (1X,/,'*** FINAL ESTIMATE ***',//,

* 1X,1X,'I',9X,'H',9X,'M',9X,'MF',/)

DO 50 N=1,NPTS

open(2,file='m.out',status='unknown')

50 WRITE (2,51) N, X(N),Y(N),YFIT(N)

51 FORMAT (1X,I2,3X,F8.1,2(3X,E9.3))

WRITE(2,59)

59 FORMAT(1X,/)

DO 60 J=1,NTERMS

60 WRITE (2,61) J, A(J), SIGMAA(J)

61 FORMAT(1X,I2,2X,2(E12.5,5X))

WRITE (2,63) CHISQR

63 FORMAT(1X,//,' CHISQR = ',E9.3,//)

C-------------------------------

C CALL PLOTMH

C-------------------------------

10 CONTINUE

C-------------------------------

STOP

END
```

```
C####################################

FUNCTION FUNCTN(I)

C CALCULATES MAGNETIZATION: MAG (EMU/GRAM)

C====================================

DOUBLE PRECISION T1,T2,T3,B1,B2,B,XX,PI,div,Mag

Real KB, MUB, J, n, NA , V

COMMON/A/ X(100),Y(100),SIGMAY(100),YFIT(100)

COMMON/B/ A(5),DELTAA(5),SIGMAA(5)

COMMON/D/TEMP

KB = 1.3805E-23

MUB = 9.2732E-24

V = 0.01443

NA = 6.0225E23

TEMP=88

PI = 3.1416 * 4.0E-4

n = 2.236376475E19

C VARIABLE

H = X(I)

C PARAMETERS ( J = SPIN, G = G-FACTOR)

J= 7./2.

G= 1.99

C FITTING PARAMETER: F = THETA
```

```
F = A(1)
C CALC
XX= G * MUB * H /( KB * (TEMP + F ))
T1=1./J
T2= J+1./2.
T3=1./2.
B1= T2 / DTANH (T2* XX)
B2= T3 / DTANH (T3*XX)
B=T1*(B1-B2)
div = V * PI
Mag= n * MUB * G * J * B / div
FUNCTN = Mag
20 RETURN
END
C##############################################################
SUBROUTINE GRIDLS (CHISQR)
C==============================================================
C SUBROUTINE GRIDLS (BEVINGTON - PROG. 11-1, P. 212)
C MAKES A LEAST-SQUARES FIT TO A NON-LINEAR FUNCTION WITH A PARABOLIC
C EXPANSION OF CHI-SQUARES
C==============================================================
COMMON/A/ X(100),Y(100),SIGMAY(100),YFIT(100)
```

```
      COMMON/B/ A(5),DELTAA(5),SIGMAA(5)
      COMMON/BBB/NTERMS,NPTS,MODE
C=====================================================================
      NFREE = NPTS - NTERMS
      FREE = NFREE
      CHISQR = 0.
      IF (NFREE) 100,100,20
C---------------------------------------
   20 DO 90 J=1,NTERMS
C EVALUATE CHI-SQUARE AT FIRST TWO SEARCH POINTS
C-------------------------
      DO 22 I=1,NPTS
   22 YFIT(I) = FUNCTN(I)
      CHISQ1 = FCHISQ(NFREE)
C-----------------------------
C FIRST ESTIMATE WITH INITIAL PARAMETERS
      IF (J.GT.1) GOTO 711
      WRITE (9,709)
  709 FORMAT (1X,'*** FIRST ESTIMATE ***',//,
     * 1X,' N',8X,'H',12X,'M',10X,'MF',/)
      DO 710 I=1,NPTS
  710 WRITE(9,712) I,X(I),Y(I),YFIT(I)
```

```
712 FORMAT (1X,I2,3X,E9.3,2(3X,E9.3))
WRITE (9,713) CHISQ1,(A(M),M=1,NTERMS)
713 FORMAT (1X,' * CHISQ1 = ',E9.3,
* 5X,'A1 = ',E12.5,2X)
711 CONTINUE
C-------------------------
FN = 0.
DELTA = DELTAA(J)
41 A(J) = A(J) + DELTA
C-----------
DO 43 I=1,NPTS
43 YFIT(I) = FUNCTN(I)
CHISQ2 = FCHISQ(NFREE)
C--------
WRITE (9,721) CHISQ2, (A(M),M=1,NTERMS)
721 FORMAT(1X,' ** CHISQ2 = ',E9.3,
* 5X,'A1 = ',E12.5,2X,'A2 = ',E12.5)
C--------
IF (CHISQ1 - CHISQ2) 51,41,61
C REVERSE DIRECTION OF SEARCH IF CHI-SQUARE IS INCREASING
51 DELTA = -DELTA
A(J) = A(J) + DELTA
```

```
      DO 54 I=1,NPTS
   54 YFIT(I) = FUNCTN(I)
      SAVE = CHISQ1
      CHISQ1 = CHISQ2
      CHISQ2 = SAVE
C INCREMENT A(J) UNTIL CHI-SQUARE INCREASES
   61 FN = FN + 1.
      A(J) = A(J) + DELTA
      DO 64 I=1,NPTS
   64 YFIT(I) = FUNCTN(I)
      CHISQ3 = FCHISQ(NFREE)
C-------
      WRITE(9,741) CHISQ3,(A(M),M=1,NTERMS)
  741 FORMAT(1X,'*** CHISQ3 = ',E9.3,
     * 5X,'A1 = ',E12.5)
C-------
      IF (CHISQ3 - CHISQ2) 71,81,81
   71 CHISQ1 = CHISQ2
      CHISQ2 = CHISQ3
      GOTO 61
C FIND MINIMUM OF PARABOLA DEFINED BY LAST THREE POINTS
   81 DELTA = DELTA * (1./(1. + (CHISQ1-CHISQ2)/(CHISQ3-CHISQ2)) + 0.5)
```

```
A(J) = A(J) - DELTA

SIGMAA(J) = DELTAA(J) * SQRT(2./(FREE*(CHISQ3-2.*CHISQ2+CHISQ1)))

DELTAA(J) = DELTAA(J) * FN/3.

90 CONTINUE

C-----------------------------------

C EVALUATE FIT AND CHI-SQUARE FOR FINAL PARAMETERS

91 DO 92 I=1,NPTS

92 YFIT(I) = FUNCTN(I)

93 CHISQR = FCHISQ(NFREE)

C-------------------------------------------

100 RETURN

END

C###########################################

FUNCTION FCHISQ(NFREE)

C===========================================

C FUNCTION FCHISQ (BEVINGTON - PROG. 10-2, P. 194)

C EVALUATES REDUCED CHI-SQUARES FOR FIT TO DATA

C===========================================

DOUBLE PRECISION CHISQ,WEIGHT

COMMON/A/ X(100),Y(100),SIGMAY(100),YFIT(100)

COMMON/BBB/NTERMS,NPTS,MODE

C-----------------------------------
```

```
      CHISQ = 0.
      IF (NFREE) 13,13,20
   13 FCHISQ = 0.
      GOTO 40
C-----------------------------------------
C ACCUMULATE CHI-SQUARE
   20 DO 30 I=1,NPTS
      IF (MODE) 22,27,29
   22 IF (Y(I)) 25,27,23
   23 WEIGHT = 1. / (Y(I))
      GOTO 30
   25 WEIGHT = 1. / (-Y(I))
      GOTO 30
   27 WEIGHT = 1.
      GOTO 30
   29 WEIGHT = 1. / SIGMAY(I)**2
   30 CHISQ = CHISQ + WEIGHT*(Y(I)-YFIT(I))**2
C-----------------------------------------
C DIVIDE BY NUMBER OF DEGREES OF FREEDOM
      FREE = NFREE
      FCHISQ = CHISQ / FREE
C-----------------------------------------
```

```
40 RETURN

END
```

Appendix B

The Fortran Program Used to Generate Magnetization Values Using θ_N Values Gotten from Extended Brillouin Function Fit

---

```
DOUBLE PRECISION T1,T2,T3,B1,B2,B,XX,PI,div,Mag
Real KB, MUB, J, n, NA , V
Dimension X(400) , Y(400)
KB = 1.3805E-23
MUB = 9.2732E-24
V = 0.01443
NA = 6.0225E23
TEMP= 88
theta=.17602E+02
PI = 3.1416 * 4.0e-4
n = 2.236376475E19
PARAMETERS ( J = SPIN, G = G-FACTOR)
J= 7./2.
G= 1.99
L = 1
open(1,file='mm.dat',status='unknown')
28 READ(1,*,END=29) H
```

```
X(L)=H

L=L+1

GOTO 28

=========

Calculation

=========

29 Do 30 M=1,L-1

XX= G * MUB * X(M) /( KB * (TEMP - theta ))

T1=1./J

T2= J+1./2.

T3=1./2.

B1= T2 / DTANH (T2* XX)

B2= T3 / DTANH (T3*XX)

B=T1*(B1-B2)

div = V * PI

Mag= n * MUB * G * J * B / div

Y(M)= Mag

open(2,file='m.out',status='unknown')

write(2,*) Y(M)

30 continue

End
```